# Neuronal coherence and its functional role in communication between neurons

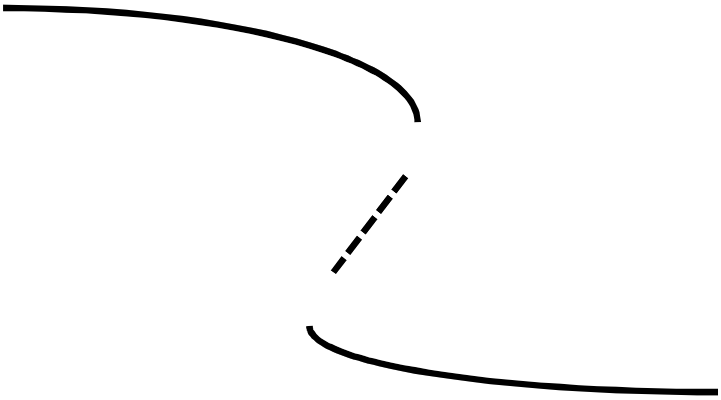

**Magteld Zeitler-Geurds**

# Neuronal coherence and its functional role in communication between neurons

Een wetenschappelijke proeve op het gebied van de
Natuurwetenschappen, Wiskunde en Informatica

## Proefschrift

ter verkrijging van de graad van doctor
aan de Radboud Universiteit Nijmegen,
op gezag van de rector magnificus prof. mr. S.C.J.J. Kortmann,
volgens besluit van het college van decanen
in het openbaar te verdedigen op dinsdag 9 februari 2010
om 13.30 uur precies

door

**Magteld Zeitler-Geurds**

geboren op 22 december 1970
te Nijmegen

Promotor : Prof. dr. C.C.A.M. Gielen

Manuscriptcommissie : Prof. dr. P.H.E. Tiesinga
Dr. A. Daffertshofer (Vrije Universiteit Amsterdam)
Prof. dr. S.A. van Gils (Universiteit Twente)

This research was supported by NWO-Council for Cognition (NWO 051.02.050)

ISBN: 978-90-9024990-2

Gedrukt door PrintPartners Ipskamp, Enschede

# Contents

## Chapter 1

# General introduction

The human brain is a very complex system, built up by billions of neurons, each interacting with many others (typically in the range from 10 to $10^6$). Through these interactions neurons can communicate with each other and can exchange information. How is information encoded? And what are the underlying biological mechanisms used for coding? Neuroscientists can use a variety of tools, like experimental brain imaging techniques, information theory and / or models to investigate these fundamental questions in neuroscience. Models can be used to describe the experimental data, but also to test hypotheses that result from experimental findings and make predictions that can, in turn, be tested experimentally. A model is often considered to be ”good” if it is as simple as possible, while still containing all elements that are assumed to be essential. In this way, the number of parameters in the model should be reduced and thus also the probability that one can generate every possible result. The results obtained with a simple model can be understood and explained easier. However, the models often remain fairly complex and although analytical approaches are preferable, computer simulations are needed to investigate the behaviour of the model. Theoretical and computational neuroscience studies investigate possible neuronal mechanisms that underly experimentally observed neuronal phenomena, ranging from microscopic to macroscopic observed phenomena, from molecules, single neurons and networks towards behaviour. In the following I will provide a brief overview about several aspects in single neurons and (small) networks that appear most relevant for the remainder of this thesis.

## 1.1 Single neuron models

The main components of neurons are the dendrites, the soma and the axon (see Fig. 1.1A) (Dayan and Abbott, 2001; Kandel and Schwartz, 1982). The connections between neurons are called synapses. Most synapses are chemical and form a specialised connection between the presynaptic axon terminator and the postsynaptic dendrite (see Fig. 1.1B). An electric pulse that arrives at the axon terminator causes the release of neurotransmitter (chemical substance) contained in the synaptic vesicles. The neurotransmitter diffuses across the synaptic cleft and part of it will temporarily bind to the neurotransmitter receptors at the dendrites. The effect is that a corresponding ion-specific channel opens to enable an in- or outflux of that specific ion-type to or from the interior of the neuron. This will cause a small post-synaptic current in the dendrite. The information flow in a neuron goes as fol-

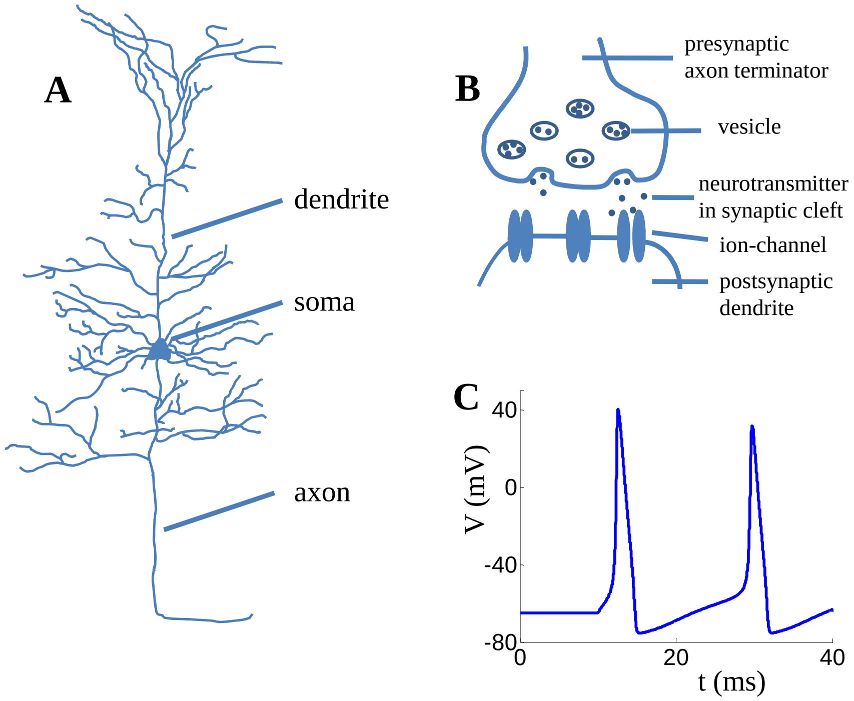

Figure 1.1: (A) shows the main components of a neuron. (B) shows a chemical synapse between the presynaptic axon terminal and the postsynaptic dendrite. (C) shows the membrane potential with two action potentials.

lows: the dendrites receive inputs from other neurons via synapses and transmit the induced electric currents to the soma. If the resulting potential of the soma exceeds a certain threshold, the soma (more precisely the axon-hillock: the point where the soma is connected to the axon) will generate a brief electric pulse. The pulse has an amplitude of $\sim$100 mV starting from a baseline of $\sim$ -70 mV (see Fig. 1.1C). The axon transmits this brief pulse, called action potential or spike, via synapses to other cells.

The shape of an action potential of a neuron is identical for all action potentials and therefore the shape does not carry any information. Information is encoded by the number of spikes and when these spikes occur (spike times). A sequence of action potentials is called a spike train and can be characterised by the spike times. The firing rate of a neuron is the number of generated spikes per second.

There are many single neuron models. In the next sections I will discuss those single neuron models that are used in the oncoming chapters of this thesis.

### 1.1.1 Poisson model

One of the most simple models for a neuron is the so-called Poisson neuron, which generates an action potential according to a rate-modulated Poisson process. This is a stochastic process that generates a sequence of spike times. For a Poisson process, the probability that a spike occurs is independent of the history of all preceding spikes. However, this is not the case for real neurons. Since experiments have shown that the ratio between the standard deviation and the mean inter-spike-interval (ISI, the time between two succeeding spikes) corresponds very well with the ratio for a Poisson process, nl. one, the Poisson model is a valid model to produce spike trains with statistics as reported by experiments. The Poisson distribution tells that the number of spike events $n$ within a certain time interval $T$ of a spike train with an average firing rate $r$ is given by (see e.g. Dayan and Abbott, 2001)

$$P_T(n) = \frac{(rT)^n}{n!}\exp(-rT). \tag{1.1}$$

There are several ways of implementing this model. One method is to divide the time interval $T$ into small bins $\Delta t$. The probability $p_{\Delta t}(1)$ that a spike occurs within a certain bin of size $\Delta t$ equals the product $r\Delta t$. If a random number, drawn from a uniform distribution between 0 and 1, is smaller than this probability $p_{\Delta t}(1)$, this bin gets a spike, otherwise not. The advantage of this procedure is that it can be used for homogeneous Poisson processes, meaning that the rate is constant, as well as for inhomogeneous Poisson processes for which the rate is time-dependent.

Figure 1.2A shows the spikes (dots) generated by 250 homogenous Poisson processes (y-axis) as a function of time. This is called a rasterplot. Figure 1.2B

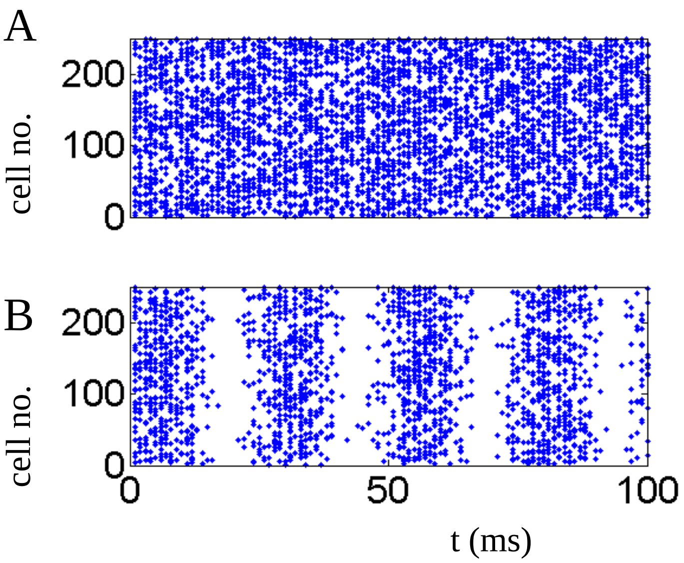

Figure 1.2: (A) rasterplot of 250 neurons firing according to a homogeneous Poisson process. (B) rasterplot of 250 inhomogeneous Poisson model neurons, modulated by a sinusoid.

shows the rasterplot of 250 inhomogeneous Poisson trains, each driven by the same sinusoidal rate. Poisson spike trains are often generated to produce spike input (with or without a time-dependent rate) to other single neuron models. In this report this procedure will be used to generate the time-dependent input spike trains for the model studies described in chapters 2 and 3.

### 1.1.2 Mirollo-Strogatz model

Another very simple neuron model is the Mirollo-Strogatz (MS) model that represents the neuron as a phase oscillator. This simplification assumes that the spike inputs of the thousands of presynaptic neurons arrive randomly, so that it can be approximated by a constant input, representing the background activity. Experimental results of neurons in slices show that a neuron can fire regularly if a constant current is applied to it (Bal et al., 2002). This justifies the assumption of simplifying the neuron to a phase oscillator. A Mirollo-Strogatz oscillator is described by an internal state $f$, corresponding to the membrane potential of a neuron, and a phase variable that encodes the time until its next pulse. This smooth, monotonically increasing, concave function $f : [0,1] \longrightarrow [0,1]$

$$f(\phi) = b^{-1} \ln\left(1 + \left(e^{b} - 1\right)\phi\right) \tag{1.2}$$

is a member of a general class of dynamics of neuron models, like the leaky integrate-and-fire neuron (described in section 1.1.3) with fast synaptic responses and the conductance-based threshold neuron (Timme et al., 2003). In this thesis I always use $b = 3$ (Mirollo and Strogatz, 1990; Ernst et al., 1995; Timme et al., 2003) as dissipation parameter.

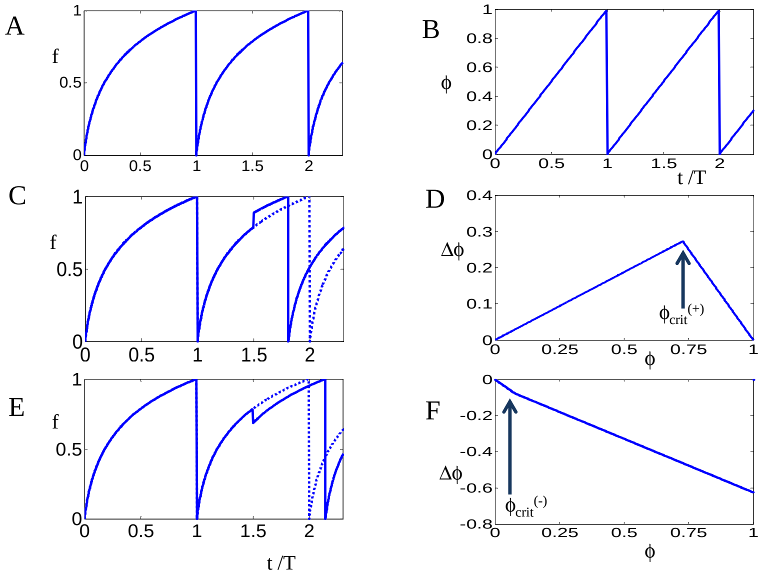

Figure 1.3: internal state of an unpertubated Mirrollo-Strogatz oscillator (A) and phase (B) versus the ratio of time and intrinsic period of the unpertubated MS-oscillator. (C) internal state of MS-oscillator when it receives an excitatory input at $t/T = 1.5$ (solid line). (D) phase response curve of the MS-oscillator for excitatory input with strength $\varepsilon = 0.1$. (E) internal state of MS-oscillator that receives an inhibitory input at $t/T = 1.5$ (solid line). (F) phase response curve for inhibitory input with strength $\varepsilon = 0.3$. In (C) and (E) the dashed lines are the internal states of the unpertubated MS-oscillator.

The phase of the oscillator $\phi \in [0,1]$ is at its lowest value ($\phi = 0$) if $f = 0$. At $\phi = 1$ (corresponding to $f = 1$) the oscillator reaches threshold, emits a pulse, and resets its phase to zero. Figure 1.3A shows the internal state $f$ of a Mirollo-Strogatz (MS-) oscillator as a function of the ratio of time and intrinsic period of the MS-oscillator. Since the time-derivative of the phase is 1, the modulus 1 of this ratio is equivalent to the phase $\phi$ of the oscillator (see Fig. 1.3B). In the presence of neuronal interactions the MS-oscillator will receive spike input from other oscillators. Depending on the type of coupling between the two oscillators the internal state will increase (excitatory coupling) or decrease (inhibitory coupling) by a fixed amount $\varepsilon$,

$$f(\phi) = b^{-1} \ln \left[ 1 + \left( \mathrm{e}^{b} - 1 \right) \phi \right] \pm \varepsilon \tag{1.3}$$

and generate a pulse if the threshold $f = 1$ is reached. An excitatory input causes an increase of the internal state value and thus a phase advance: the MS-oscillator will reach threshold sooner due to an excitatory input (shown in Fig. 1.3C). An inhibitory input, reduces the internal state (phase delay), so that it takes longer before the oscillator reach threshold and emits a spike (see Fig. 1.3E). The precise phase shift is described by the phase response curve (PRC), which gives the phase shift $\Delta\phi$ as a function of the phase $\phi \in [0,1]$ at the arrival time of the pulse (Izhikevich, 2007). The PRC for the original Mirollo-Strogatz model (excitatory couplings) shows a phase advance whenever $\Delta\phi \geq 0$ holds, even at zero phase, which appears improper for 'real neurons', that include a refractory period, during which the input has no effect on the internal state of the neuron (refractory period). In this thesis I corrected for this by using a modified PRC

$$\mathrm{PRC}^{(+)} = \begin{cases} \left( 1/\phi_{\mathrm{crit}}^{(+)} - 1 \right) \phi & \text{for } \phi \leq \phi_{\mathrm{crit}}^{(+)} \\ 1 - \phi & \text{otherwise} \end{cases} ;$$

with $\phi_{\mathrm{crit}}^{(+)} = \left( \mathrm{e}^{b(1-\varepsilon)} - 1 \right) / \left( \mathrm{e}^{b} - 1 \right)$ representing the phase at which the maximum phase shift is reached (see Fig. 1.3D). When a pulse arrives at the oscillator at phase $\phi \geq \phi_{\mathrm{crit}}^{(+)}$, the oscillator immediately emits a pulse. For biological systems the phase shift reaches its maximum when the input arrives in the second half of the cycle (see also Tsubo et al., 2007), i.e. $\phi_{\mathrm{crit}}^{(+)} > 0.5$ yielding $\varepsilon \leq 0.21$.

For an inhibitory coupling an input spike causes a phase delay and therefore the MR-oscillator cannot elicit a pulse as a direct response to the inhibitory input (see Fig. 1.3E). This phase delay is described as a function of the phase at the arrival time of the pulse and is given by the following PRC:

$$\mathrm{PRC}^{(-)} = \begin{cases} \frac{\mathrm{e}^{-b\varepsilon} - 1}{\mathrm{e}^{b} - 1} + \left( \mathrm{e}^{-b\varepsilon} - 1 \right) \phi & \text{for } \phi > \phi_{\mathrm{crit}}^{(-)} \\ -\phi & \text{otherwise} \end{cases} ;$$

as shown in Fig. 1.3F. When a pulse arrives at the oscillator at phase $\phi \leq \phi^{(-)}_{\text{crit}}$, with $\phi^{(-)}_{\text{crit}} = \left(\mathrm{e}^{b\varepsilon}-1\right) / \left(\mathrm{e}^{b}-1\right)$ the oscillator is reset to zero phase and corresponding amplitude $f$. This model, approximating neurons as phase oscillators is used for the analytical study of the dynamics of synchronisation in Chapter 4.

### 1.1.3 Leaky Integrate-and-Fire model (LIF)

Although in 1907 Lapicque did not have any knowledge of the underlying mechanisms for the generation of action potentials, he used an electric circuit as shown in Fig. 1.4A to model the spiking of the neuron (Abbott, 1999). An injected input current, $I^{ext}(t)$ is split into two components, one part charges the capacitor $C$, the other part flows through the resistor, $R$. The voltage difference between the interior and the exterior of a cell is called the membrane potential, $V(t)$ and is described by:

$$C\frac{dV(t)}{dt} + \frac{V(t)}{R} = I^{ext}(t), \tag{1.4}$$

or in more common form:

$$\tau_m \frac{dV(t)}{dt} = -V(t) + RI^{ext}(t). \tag{1.5}$$

with $\tau_m = RC$ the time constant of the leaky integrator.

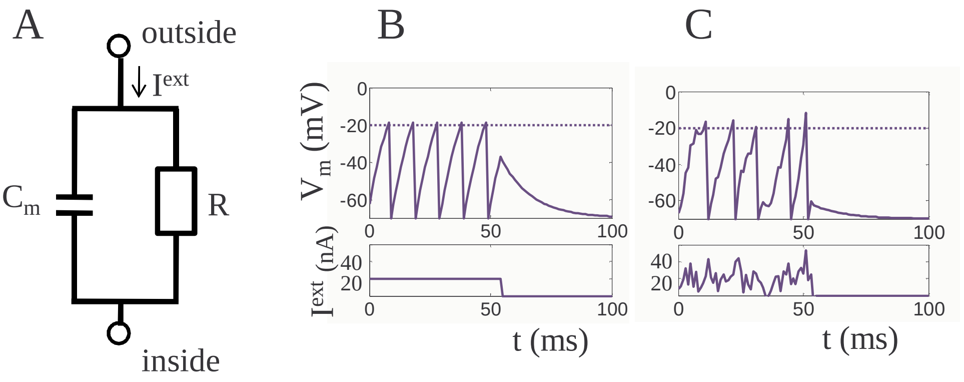

Figure 1.4: (A) electric circuit of the leaky integrate-and-fire model, consisting of a parallel capacitor ($C_m$) and resistor ($R$) to model a neuron. $V$ is the membrane potential, $I^{ext}$ the injected current. (B) The injected current (lower panel) and the resulting membrane potential as a function of time. (C) As in (B), but now for a time-varying current. The dashed line in (B) and (C) are the threshold potential.

This simple model alone is not able to generate action potentials. Lapicque solved that problem by postulating that when the capacitor is charged to a certain threshold potential, an action potential will be generated and the capacitor will discharge and thereby resets the potential to a certain value, hence called the reset potential. The membrane potential of the leaky integrate-and-fire model between two successive action potentials is described by equation 1.4 or 1.5. If the membrane potential has reached the threshold potential, the model neuron generates an action potential and the membrane potential is reset to the reset potential, $V_{reset}$.

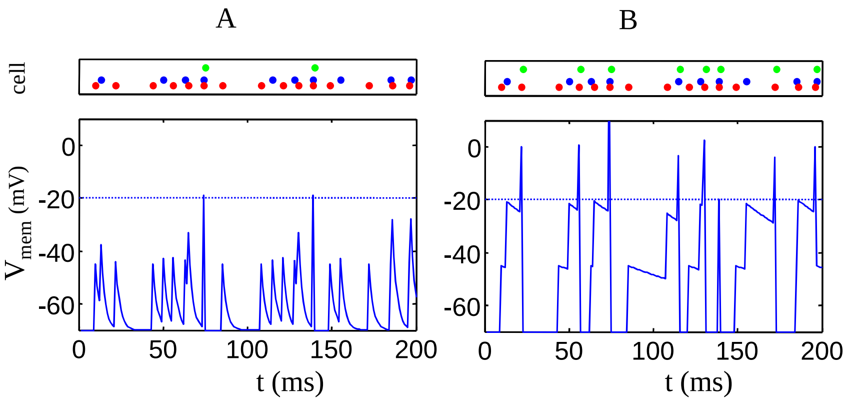

Figure 1.5: Type of information encoded depends on the time-constant of the LIF-neuron. Column A: raster plot of the input spikes and the resulting membrane potential of a leaky integrate-and-fire neuron with a small time constant $\tau_m = 3\ ms$. The neuron generates action potentials if at least a certain number of input spikes has arrived within a small time window. For small time constants, the neuron behaves as a coincidence detector. Column B: rasterplot of the input spikes and the resulting membrane potential of a leaky integrate-and-fire neuron with a large time constant $\tau_m = 100\ ms$. The information encoded now represents the number of received input spikes.

For a constant external current, this model generates spike times with constant inter-spike-intervals (the time between two succeeding spikes) resulting in a constant number of spikes per second (firing rate) (see Fig. 1.4B). The inter-spike-intervals (ISIs) will be variable for irregular currents, implying that the model neuron fires irregularly (see Fig. 1.4C). If some current was applied to the LIF neuron and than suddenly stopped (e.g. $I(t) = 0$ nA at $t \geq 55$ ms in Fig. 1.4B and C), the membrane potential will decrease exponentially to the rest potential unless a new current is applied before. During the time interval $\tau_m = RC$ after the sudden stop of input, the membrane potential looses 63% of its initial value.

For small membrane time constants $\tau_m$ (the neuron has a short memory) the LIF neuron is acting as a coincidence detector, in the sense that it only fires if it receives a certain amount of simultaneous input spikes within a small time interval (see column A of Fig. 1.5). The subthreshold change in membrane potential by an input spike induced will decay fast towards the resting potential and only simultaneously arriving input spikes can cause an increase in membrane potential that is high enough to generate a spike. For long membrane time constants, the neuron has a long memory, and the LIF neuron is more acting as a spike counter: it spikes as soon as it has received a certain number of spikes (see column B of Fig. 1.5).

The LIF model is used to compute relatively fast the spike times of a neuron, neglecting the shape of an action potential, but still incorporating the recent firing history, going back to the last spike time.

### 1.1.4 Hodgkin-Huxley model

A more realistic biophysical model of a single neuron is the Hodgkin-Huxley model, named after the two scientists who derived empirically the differential equations for the ionic currents in this model and received the Nobel prize for this work. The Hodgkin-Huxley model describes the dynamics of the cell membrane not just between two action potentials, but also during an action potential. The dynamics of the membrane potential and the occurrence and shape of an action potential are caused by currents (flow of ions) that pass the cell membrane of a neuron via synapses. The membrane separates the interior of the neuron from the surrounding extracellular space. The concentration of ions within this extracellular space differ from that inside the cell. Embedded in the membrane are synapses through which ions can selectively pass under certain circumstances. If there would be no electrical potential difference between the interior and exterior of the cell, ions tend to diffuse through these synapses as if the ions would be uncharged. However, since the electrical potential difference between outside and inside the cell is -65 mV, ions will tend to move driven by the gradient of the electrical potential across the membrane. The direction of the net movements depends on whether the effect of the concentration difference or the effect of the electric potential difference is larger. If these effects are equally strong, there is no net force acting on the ions, and there will be no net movement of the ions. The Nernst equation for ion $x$ gives the relation between the electrical potential across the membrane, $E_x = V_{in} - V_{out}$ that is required to produce an electrical force,

$$ZF(V_{in} - V_{out}), \tag{1.6}$$

that is equal and opposite to the force caused by the concentration difference of ion $x$

$$RT \ln \frac{[x]_{in}}{[x]_{out}}, \tag{1.7}$$

where $Z$ is the valency of the ion, $F$ = 96 487 C mol$^{-1}$ is the Faraday constant, $R$ = 8.3143 J mol$^{-1}$ K$^{-1}$ is the universal gasconstant, $T$ is the absolute temperature and $[x]$ is the concentration of ion $x$ in which $x$ is the general form for any type of ion involved. The Nernst equation is expressed as

$$E_x = \frac{RT}{ZF} \ln \frac{[x]_{out}}{[x]_{in}}. \tag{1.8}$$

It is only valid for one type of ions and if there is no net flow of these ions (at equilibrium) (Berne and Levy, 1988).

A

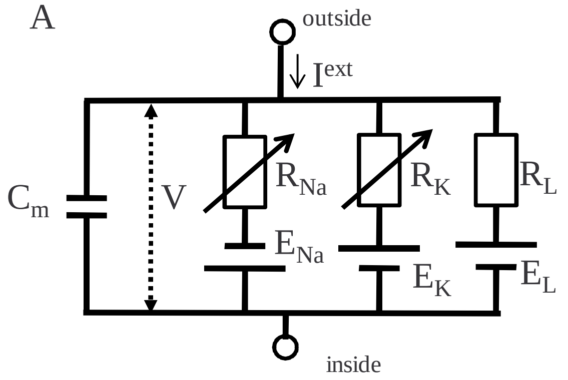

B

| | |
|---|---|
| $E_L$ | -54.387 mV |
| $E_{Na}$ | + 50 mV |
| $E_K$ | -77 mV |
| $C_m$ | 0.01 nF mm$^2$ |
| $g_{Na}$ | 1.2 mS/mm$^2$ |
| $g_K$ | 0.36 mS/mm$^2$ |
| $g_L$ | 0.003 mS/mm$^2$ |

Figure 1.6: (A) electric circuit for the Hodgkin-Huxley neuron model, consists of a parallel capacitor ($C_m$), a constant leak resistor ($R_L = 1/g_L$) and two voltage-dependent resistors $R_{Na} = 1/g_{Na}$ and $R_K = 1/g_K$ to model the sodium and potassium channels. $V$ is the membrane potential, the batteries represent the reversal potentials. $I^{ext}$ is the injected current. (B) table with some typical parameter values (Hodgkin and Huxley, 1952).

Since more than just one type of ions is involved in the intrinsic dynamics of the membrane, e.g. $Na^+, K^+, Cl^-$, one has to use the Goldman-Hodgkin-Katz equation to determine the rest potential of the neuron, i.e. the membrane potential if no external currents are injected. This membrane potential is given by (Berne and Levy, 1988)

$$V_m = \frac{RT}{F} \ln \frac{P_K[K]_{out} + P_{Na}[Na]_{out} + P_{Cl}[Cl]_{in}}{P_K[K]_{in} + P_{Na}[Na]_{in} + P_{Cl}[Cl]_{out}} \tag{1.9}$$

with $P_x$ the permeability for ion $x$ and $[x]_{in}$ ($[x]_{out}$) the concentration of ion $x$ inside (outside, respectively) of the neuron.

The membrane potential $V_m$ and its dynamics in the Hodgkin-Huxley model can be explained by of the electrical circuit as shown in Fig. 1.6 (Kandel and Schwartz, 1982; Gerstner and Kistler, 2002; Dayan and Abbott, 2001). This circuit contains a capacitor $C_m$ that represents the capacitance of the membrane, which separates the interior from the exterior of the cell. The circuit further has one constant resistor and two variable resistors. In the standard Hodgkin-Huxley model two voltage-gated ion specific synapses are described, namely the sodium and the potassium channel (neurotransmitter-gated ion channels), and one channel that allows other ions, mainly chloride ions, to diffuse (called leak channel). Hodgkin and Huxley have measured the dynamics of the ion channels in the giant axon of a squid as a function of the membrane potential and time. This resulted in three extra differential equations, which describe the dynamics of the activation and inactivation of the potassium and sodium channels (shown in Fig. 1.6A).

The Hodgkin-Huxley model is given by the following set of differential equations (Hodgkin and Huxley, 1952):

$$\begin{aligned} C_m \frac{dV}{dt} &= -\bar{g}_{Na} m^3 h (V - E_{Na}) - \bar{g}_K n^4 (V - E_K) - \bar{g}_L (V - E_L) + I^{ext}(t), \\ \frac{dx}{dt} &= \frac{x_\infty(V) - x}{\tau_x(V)} \end{aligned} \tag{1.10}$$

with $E_{Na}, E_K$ the reversal (Nernst) potentials of sodium and potassium, $E_L$ the leak reversal potential, $\bar{g}_{Na}$, $\bar{g}_K$ the maximum conductances of the sodium and potassium channel, respectively, $\bar{g}_L$ the maximum conductance of the leak channel, and $I^{ext}(t)$ the external input current. $x \in \{m, h, n\}$ with $m$ ($h$, $n$) the probability that the $m-$ ($h-$, $n-$, respectively) gate in the ion-channel is open. For a fixed membrane potential $V$, the variable $x$ approaches the limiting value $x_\infty(V)$ exponentially with time constant $\tau_x(V)$. The asymptotic values $x_\infty(V)$ and time constants $\tau_x(V)$ are shown in Fig. 1.7 and given by:

$$x_\infty(V) = \frac{\alpha_x(V)}{\alpha_x(V) + \beta_x(V)} \tag{1.11}$$

$$\tau_x(V) = \frac{1}{\alpha_x(V) + \beta_x(V)} \tag{1.12}$$

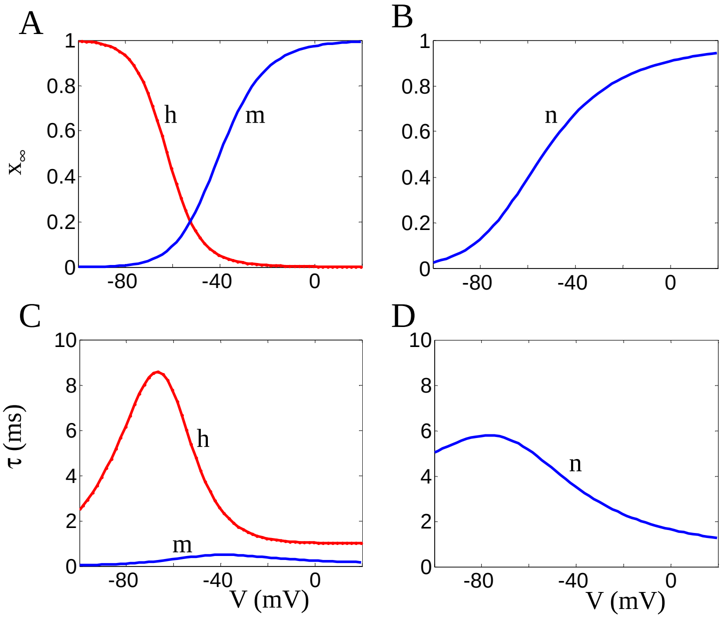

Figure 1.7: (A) asymptotic values for the m- and h-gate of the sodium channel. (B) Time constant of the m- and h- gate of the sodium channel. (C) asymptotic value of the h-gate of the potassium channel. (D) Time constant of the n-gate of the potassium channel. (see pages 170-173 of Dayan and Abbott (2001) for the exact equations)

with the opening and closing rate functions $\alpha_x(V)$ and $\beta_x(V)$ determined empirically by Hodgkin and Huxley for the giant axon of the squid. Typical values for reversal potentials and conductances are given in the table of Fig. 1.6B (Hodgkin and Huxley, 1952).

The Hodgkin-Huxley model is used to model realistic neurons and can be extended by adding additional ion channels and also by taking the geometric structure of a neuron into account, both at the expense of computational time.

## 1.2 Neuronal representations

In order to process sensory information, like visual images, sounds, differences in temperature or pressure, our brain has to convert this information into a format that neurons can use for their computations and communication. Neurons can only exchange information via synapses if these are activated by presynaptic action

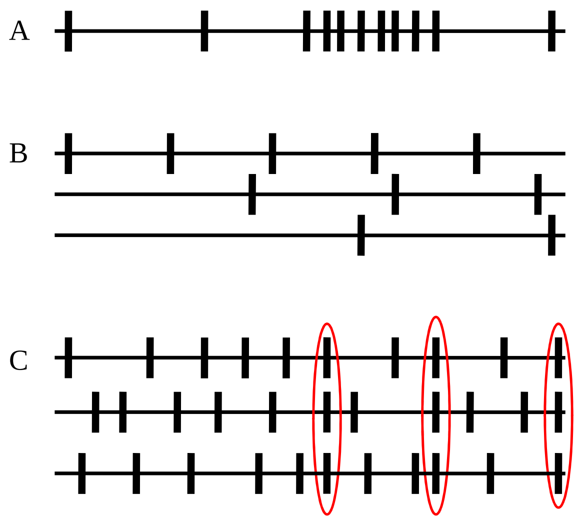

Figure 1.8: Three different possibilities of coding neuronal information illustrated by spike trains, represented as a horizontal time-line with small vertical bars at the time that a spike occurs. (A) rate coding: the firing rate codes e.g. the absence (low firing rate) / presence (high firing rate) of a stimulus. (B) recruitment: the number of active neurons codes the force that the muscle will execute. (C) temporal coding: the amount of simultaneous firing may code the presence of a stimulus.

potentials. Therefore, the basic unit of neuronal communication is the action potential. Since the shape of the action potentials generated by a single neuron does not change, there can be no information within the shape. Neuronal information can be encoded by different schemes, e.g. by the exact timing of the action potential or the average number of action potentials per second, it can be encoded by single neurons or by the joint activity of a group of neurons or by a combination of different coding schemes.

At the beginning of the 20th century Lord Adrian measured the relation between the force applied to a muscle and the firing rate of a stretch receptor embedded in that muscle. Different forces were generated by hanging weights with different masses at the muscle (Adrian, 1926; Rieke et al., 1997). The result of his work showed that a single neuron can encode information in the average number of action potentials over a certain time period (rate coding) as show in Fig.1.8A. Another way of encoding information is recruitment. A muscle can be activated by many neurons. The more of them are active (recruited), the more force can be generated by that muscle. In the last decennia, also temporal coding has been suggested as a possibility. Temporal encoding implies that the average firing rate stays the same, but that the precise timing of the spikes generated by the neurons carries the information, e.g. by correlated spike behaviour of neurons. In other words, neurons tend to fire in synchrony, and the information is encoded by the amount of synchrony. An example, found in the auditory cortex, was described by deCharms and M. M. Merzenich (1996). They showed that the presence of a 4 kHz tone does not significantly change the firing rate of the two recorded neurons, but increases the probability that both neurons fire simultaneously.

This suggests that information can be encoded in the firing rate of single neurons but also in the joint activity of a group of neurons and the timing of individual action potentials compared to the activity of others. The question how the brain encodes the neuronal information is still a hot topic in current neuroscience research. What is the temporal precision of generated action potentials? What is the functional relevance of synchronised activity of neurons?

### 1.2.1 Oscillations

Neuronal activity can be measured using a variety of techniques, from the scalp e.g. by electroencephalograms (EEG) and magnetoencephalograms (MEG) and inside the brain by microelectrodes. These measurements have revealed periodic variations in neuronal activity in particular frequency bands. These oscillations have been a topic of research for many decades. How are these oscillations generated and what is the functional role of them? How can they spread over brain areas and how can this spreading being stopped?

With a microelectrode one can measure the membrane potential of a single neuron. The recorded variations in the membrane potential between two action potentials (sub-threshold oscillations) reflect mainly the time-dependent input to the neuron. If the input is excitatory the peaks of the oscillations will reflect the contribution of many synchronised excitatory input spikes, the troughs caused by minimal (or even a lack of) input. Other experimental techniques use the fact that synaptic activity at the dendritic tree induces an intra-cellular currents of sodium and potassium ions towards the soma of the neuron. The intra cellular currents cause an extracellular return current from the soma towards the top of the dendritical tree (charge conservation). This pattern of currents corresponds to a dipole. Since neurons (and thus the dipoles) are locally aligned in cortex with the dendrites at the outside and the somas more inwards the brain, the extracellular currents generate an electric field at the scull, that can be measured by the electroencephalogram (EEG) if a large group of aligned neurons shows synchronised activity. If the activity within a group of neurons is uncorrelated the signals will be to weak to record. Synchronised activity will result in oscillatory EEG signals. The intracellular currents generate a

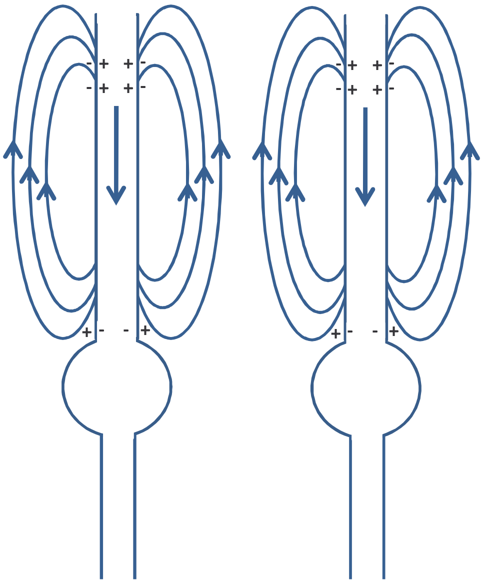

Figure 1.9: Synaptic activity at the dendrite causes an influx from positive ions, that leads to an intracellular current towards the soma. The charge difference in the extracellular liquid results in an extracellular current flowing in the opposite direction as the intracellular current. The difference between the charges at the top of the dendritic tree and near the soma form a dipole. This dipole generates an electric field at the scull that can be measured by electroencephalogram (EEG). At the same time this dipole generates a magnetic field that can be recorded by magnetoencephalograms (MEG).

small magnetic field, that can be recorded with magnetoencephalograms (MEG), if the dipoles are aligned and if the currents have a component parallel to the skull. EEG and MEG are methods that allow us to study oscillatory phenomena of large groups of neurons. The more neurons are locally synchronised, the larger the amplitudes of these oscillations will be.

Besides subthreshold membrane potential oscillations, oscillations can also be generated by a neuronal network with a delayed feedback connection. If the neurons within a network become simultaneously active, and this activity is fed back (with some delay due to signal processing time) to the network itself, than it is possible that the network will re-activate itself: the activity will repeat itself after a certain period. This implies that the physical architecture of neuronal networks and the limited speed of information transfer due to axonal conduction and synaptic delays allow oscillatory brain activity (Buzsáki and Draguhn, 2004). Another possibility how oscillations can be generated is called the pyramidal-interneuron network gamma oscillation (PING) model (Whittington et al., 2000). In this model a population of pyramidal (excitatory neurons) is recurrently connected via a population of inhibitory interneurons. The pyramidal cells are driven by a tonic input current. Their spike response activates the inhibitory interneuron population, which in turn will inhibit the pyramidal population for a certain period in time. The pyramidal cells can be excited again by the tonic excitatory input current, as soon as that the inhibition has decayed. The frequency of this oscillatory activity is mainly determined by the duration of inhibition of the excitatory cells by the inhibitory neurons.

## 1.3 Selective attention

In our daily life we are overwhelmed by visual stimuli. Each stimulus is projected on a part of our retina and encoded into action potentials in a large number of cells. These action potentials are transferred via the optic nerve to the lateral geniculate body from where the information is transferred further to the visual cortex. Depending on the exact location of the stimulus in the visual field and the receptive field of a neuron, a neuron in the visual cortex will respond to the stimulus or not. The area of the visual field where stimuli can affect the response of a neuron is called receptive field. Along the successive stages of this visual path way the size of the receptive fields of the neurons increases (Smith et al., 2002). For certain areas in the visual cortex it is possible that the receptive field of neurons is large enough to present two non-overlapping stimuli.

Usually, the world around us contains many different objects. However, not all objects are equally relevant. Yet, these objects compete for attention. The problem to select the relevant object from many competing stimuli, is called selective attention.

Moran and Desimone (1985) recorded single cell activity in the visual cortex (V4) and inferior temporal cortex (IT) of monkeys, that were trained to attend to a stimulus at one location and ignore the stimulus that was presented simultaneously at another position. They have shown that a neuron responds with a high firing rate to an effective visual stimulus, when a stimulus was presented within its receptive field; and with a low firing rate to an ineffective stimulus, respectively. If both stimuli were offered simultaneously within the receptive field of neurons in the inferior temporal cortex, the firing rate was not equal to the sum of the high and low firing rates corresponding to the effective and ineffective stimulus, but rather in between both of them. This phenomenon reflects stimulus competition in the responses of the neuron. However, when the monkey had to attend the effective stimulus, the firing rate was similar to the situation when only the effective stimulus was presented. Similarly, if the monkey had to attend the ineffective stimulus, the firing rate was as if only the ineffective stimulus was presented in the receptive field.

Reynolds et al. (1999) and other studies (e.g. McAdam and Maunsell (1999); Luck et al. (1999)) showed that if only one stimulus is presented within the receptive field of the recorded neuron, attention increases the firing rate of that neuron to that stimulus. This implies that although the visual stimulus has not been changed, attention affects the response of neurons. Fries et al. (2001b) recorded the activity of a small group of neurons (multi-unit activity) and the local field potential (LFP) with microelectrodes in macaque visual area V4. Consistent with other studies, Fries et al. (2001b) found firing rate changes due to attention. Furthermore, they examined the effect of attention on synchronisation between the spikes and the local field potential recorded by two separate electrodes. Attention increased gamma-frequency synchronisation of V4 neurons representing the behaviourally relevant stimulus, even before the firing rates were affected by attention. This raises the question what is the contribution of the synchronised oscillations to selective attention.

## 1.4 ”Communication Through Coherence” hypothesis

What determines the effectiveness of the information exchange between neuronal populations? Is it the exact timing of the (synchronised) input spikes?

If a neuron has just generated a spike, then it is not excitable for a while since it is in a refractory period. After the absolute refractory period, in which no input can cause the generation of a spike, follows the relative refractory period, in which the excitability is decreased and where only powerful input might cause a spike. After the relative refractory period follows a period in which also weak inputs can elicit an action potential. The probability that the neuron will generate a spike depends on several parameters like the actual membrane potential, the strength and type of input and the steepness of the change in the membrane potential (Azouz and Gray, 2000). If the neuron receives input when it is least excitable, it will not transfer the input to the next neurons. If the neuron receives input at the time when it is very excitable it will most likely generate rapidly an action potential and pass that on to the next layer of neurons, especially if the input is synchronised in time. This led Fries (2005) to postulate the hypothesis that during high excitability of the

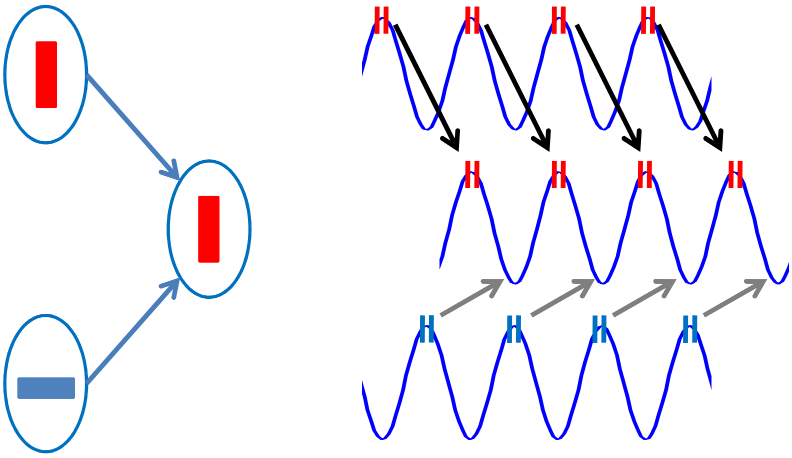

Figure 1.10: Communication through coherence hypothesis. On the left: Two population project to a third neuronal population. Each population codes a visual stimulus as shown in the oval that represents the neuronal population. On the right: the blue sine-functions represent the excitability of the neuronal populations as shown on the left. The small vertical bars on top of the sinusoid represent spikes that are elicited by the corresponding population. The arrows show at which moment that spike volley arrives in the excitability cycle of the receiving neuronal population.

receiving neuronal population the communication between the input neuron(s) and the receiving neuron is very effective. So the rhythmic excitability fluctuations of the neuron produce temporal windows for communication. This forms the basis of the ”Communication Through Coherence” (CTC) hypothesis (Fries, 2005) which implies that the effectiveness of the communication between two (populations of) neurons depends on the phase relation between them.

Figure 1.10 illustrates this idea. Suppose that one neuronal population (called the receiving population) receives input from two other populations, which each represents a visual stimulus by their activity (see left side of Fig. 1.10, where the ovals represent neuronal populations, and the bar inside the population represents the visual stimulus that was present in the receptive field of the population). When the activity of the neurons within a population is synchronised, the excitability of the individual neurons will cause an oscillation in the excitability of the population. The oscillations on the right side of the figure show the excitability of the three populations of neurons. At the top of the oscillation the population is most excitable:

the probability that the population responds to a weak input is largest. The vertical bars show the resulting spikes. A spike volley from the input population (encoding the vertical bar) arrives at the end of the cycle of the receiving population. Since the population excitability is high at that time, the receiving neuronal population will respond soon, leaving no time for inputs from other neuronal populations to transfer their information effectively. After the generation of a volley of response spikes, the excitability of the receiving population will be reduced. Input spikes that arrive at the troughs of the excitability, like those sent by the input population that encodes the horizontal bar, will generate (almost) no action potentials at the receiving population: the information flow that encodes the horizontal bar will not continue further. This suggest that the phase relation between the excitabilities of the sending and receiving neuronal populations determines the effectiveness of the information transfer between populations. Since it should be possible to change the effectiveness of information flow, e.g. selective attentional effects, the phase relations between populations should be able to change without changing the anatomy. This means that a flexible pattern of phase relations is required to realise a flexible communication structure on top of the anatomical structure.

## 1.5 Outline

The studies reported in the next chapters will shed some light on various aspects of neuronal synchronisation like its detection, its possible functional role in neglecting and selecting stimuli, and its functional role for effective neuronal communication.

The central question in chapter 2 is why experimentally derived coherence estimates between multi unit (6-10 neurons) recordings are significantly higher than between single unit recordings. I will start to derive a quantitative understanding of the interpretation of correlated output spike trains in terms of correlated input to the neurons. Then the coherence estimates between input and output spike trains and between two output spike trains are compared for spike trains of single neurons and for spike trains of small groups of neurons (about 10 neurons). I will continue with the question whether the recording of single-unit activity over a long period of time could produce the same cross correlation and coherence as multi-unit activity over a shorter period of time. Finally, I will investigate the effectiveness of analysis techniques in revealing coherent activity in multi-unit activity. For this study I use Poisson neurons for the theoretical analysis, and leaky Integrate-and-Fire and Hodgkin-Huxley neurons for the computer simulations, and I will verify the obtained results with data measured in monkey visual cortex (V4) ( Fries et al., 2001b).

In chapter 3 I will investigate whether a simple feed forward model can explain the phenomenon of stimulus competition with a role for synchronous modulation of stimulus-related activity to implement the attentional bias. In this computational study Hodgkin-Huxley neurons receive a balanced excitatory and inhibitory background input so that they behave like coincidence detectors. Besides the coherence estimate, also the phase locking value is determined in this study in order to obtain the average phase difference between the receiving output neuron and each of the two input populations of neurons.

In chapter 4 I will derive analytical expressions for the phase relation between two asymmetric Mirollo-Strogatz oscillators and include the conduction delay of the action potential travelling along the axon. This theoretical study sheds some light on the effect of different coupling strengths between the two excitatory (inhibitory, respectively) coupled oscillators.

Finally I will explore the role of coherence in the communication between two neuronal populations by modelling the corticospinal system (chapter 5), which results in reproducing the major experimental findings of van Elswijk et al. (2009). After that, I will explore the sensitivity of the model for several parameters in order to obtain a better understanding of the experimental result that the effectiveness of the neuronal communication is modulated by the phase of the population of $\alpha$-motoneurons in the spinal cord.

## Chapter 2

# Assessing neuronal coherence with single-unit, multi-unit and local field potentials

The purpose of this study was to obtain a better understanding of neuronal responses to correlated input, in particular focussing on the aspect of synchronisation of neuronal activity. The first aim was to obtain an analytical expression for the coherence between the output spike train and correlated input and for the coherence between output spike trains of neurons with correlated input. For Poisson neurons, we could derive that the peak of the coherence between the correlated input and multi-unit activity increases proportionally with the square root of the number of neurons in the multi-unit recording. The coherence between two typical multi-unit recordings (2 to 10 single-units) with partially correlated input increases proportionally with the number of units in the multi-unit recordings. The second aim of this study was to investigate to what extent the amplitude and signal-to-noise ratio of the coherence between input and output varied for single versus multi-unit activity and how they are affected by the duration of the recording. The same problem was addressed for the coherence between two single-unit spike series and between two multi-unit spike series. The analytical results for the Poisson neuron and numerical simulations for the conductance-based leaky integrate-and-fire neuron and for the conductance-based Hodgkin-Huxley neuron show that the expectation value

---

Adapted from: Magteld Zeitler, Pascal Fries and Stan Gielen, *Neural Computation* 18: 2256-2281, 2006 of the coherence function does not increase for a longer duration of the recording. The only effect of a longer duration of the spike recording is a reduction of the noise in the coherence function. The results of analytical derivations and computer simulations for model neurons show that the coherence for multi-unit activity is larger than that for single-unit activity. This is in agreement with the results of experimental data obtained from monkey visual cortex (V4). Finally, we show that multi-taper techniques greatly contribute to a more accurate estimate of the coherence by reducing the bias and variance in the coherence estimate.

## 2.1 Introduction

The recent advent of multiple electrode recording technology makes it possible to study the simultaneous spiking activity of many neurons. This allows us to explore how stimuli are encoded by Rols et al. (2001) neuronal activity and how groups of neurons act in concert to define the function of a given brain region. However, in spite of the considerable technological developments and the advanced analysis tools (for an overview, see Brown et al., 2004) there are many fundamental questions regarding the interpretation of multi-unit activity.

The gold standard in animal neurophysiology has been thought to be the study of isolated single-units for a long time. However, it appears as if the use of measures of neuronal aggregate activity, like multi-unit or local field potential recordings, greatly enhances the sensitivity of correlation and coherence analyses (see e.g. Baker et al., 2003; Rolls et al., 2003). This empirical observation is not yet understood. Related to this is the question whether a multi-unit recording for time T and consisting of m single-units with the same correlated input carries the same information as a single-unit recording for time mT?

Many studies (see e.g. Singer and Gray, 1995; Kreiter and Singer, 1996; Engel et al., 2001; Fries et al., 2001a) have so far demonstrated that neurons in early and intermediate visual cortex in cat and macaque exhibit significant correlated fluctuations in their responses to visual stimuli. These cells undergo attention-modulated fluctuations in excitability that enhance temporal coherence of the responses to visual stimuli (Fries et al., 2001b, 2005). The coherence is an important parameter, since it provides a measure for the similarity between two signals. Moreover, coherence among subthreshold membrane potential fluctuations likely expresses functional relationships during states of expectancy or attention, allowing the grouping and selection of distributed neuronal responses for further processing (Fries et al., 2001a). The coherence between spike activity and local field potential was larger for multi-unit activity than for single-unit activity. Along the same lines, Baker et al. (2003) studied the cross-correlation and coherence between local field potentials and neural spike trains in monkey primary motor cortex. They concluded that a (small) population of neurons is necessary to encode the cortical oscillatory signal, i.e. the rapid modulations of synaptic input reflected in the oscillatory local field potential, effectively.

Several studies reported a lack of evidence for synchronised neuronal activity. For example, Tovee and Rolls (1992), in the inferior temporal visual cortex and Luck et al. (1997) did not observe clear synchronisation in neuronal responses in V2 and V4. However, Kreiter and Singer (1996) did find clear synchronisation in the middle temporal area (MT) if two cells were activated by the same stimulus. Besides recording in different recording areas and the use of different types of stimuli, also the statistical analysis technique might play an important role in detecting synchronisation. Advanced multitaper techniques (Percival and Walden, 2002) have proven to be useful in estimating coherence between spike trains and local field potentials by improving the signal-to-noise ratio (Pesaran et al., 2002; Jarvis and Mitra, 2001). These multitaper techniques improved the significance of synchronised oscillatory neuronal activity.

The aim of this study was threefold. First, we wanted to obtain a quantitative understanding of the interpretation of correlated output spike trains in terms of correlated input (indirectly related to the local-field potential) to the neurons. In order to do so, we started with a network of simple Poisson neurons, the behaviour of which could be analysed analytically. This simple model was then made more realistic by replacing the Poisson neurons by conductance-based neurons. The second aim of this study was to investigate to what extent the shape, amplitude and signal-to-noise ratio of the coherence between input and output varied for single versus multi-unit activity and whether the recording of single-unit activity over a long period of time could produce the same cross correlation and coherence with local field potential as multi-unit activity over a shorter period of time. We addressed the same question for the coherence between two spike outputs, both for two single and for two multi-unit spike series. The third aim of this study was to investigate the effectiveness of analysis techniques in revealing coherent activity in multi-unit activity. These three topics were investigated by comparing the results of coherence for single- and multi-unit activity in theoretical analyses for Poisson neurons, in computer simulations for conductance-based model neurons, and for data measured in monkey visual cortex (V4) (Fries et al., 2001b).

## 2.2 Methods and Theory

In order to obtain a better insight into the coherence between the local-field potential (LFP) at the one hand and single- or multi-unit activity at the other hand and in the coherence between spike trains of neurons that receive partially correlated input, we will start with a simple model (see Fig. 2.1). The local field potential reflects mainly the sum of postsynaptic potentials from local cell groups (Buzsáki, 2004). Therefore, the local field potential is seen to be indirectly related to the correlated input of neurons. We consider groups of neurons receiving correlated input that is reflected in a simulated LFP. Therefore, we modelled those neurons as rate varying Poisson processes with a base-line firing rate plus rate modulations driven by the LFP fluctuations. Note that in this study we refer to the LFP as common rate fluctuations of the input signal (or short: common input). In order to prevent any misunderstanding, we would like to point out that this meaning of ”common input” differs from the usual physiological meaning of common input which implies that two neurons receive the same synaptic input due to a bifurcating axon!

In this study we will determine the coherence between different signals present in the model, as shown in Fig. 2.1. First, we will concentrate on the Poisson model and derive an expression for the coherence between the common input (LFP) and the response of a single Poisson neuron (small circle in Fig. 2.1). After deriving a similar expression for multi-unit activity, we will compare both results of Spike-Field coherence functions. We will finish the theoretical part, concerning the coherence functions, by deriving expressions for the Spike-Spike coherences, first between two single-unit activities and later also between two multi-unit series of Poisson neurons. Simulation results of these coherence measures will complete the Poisson model section. We will continue by simulations of the complete model, including the conductance-based neurons (large circles in Fig. 2.1). The common input (LFP) to the Poisson neurons will be taken as the local field potential in order to determine the Spike-Field coherences between the common input and the response(s) of the conductance-based neuron(s). The Spike-Spike coherences are taken between the responses of two conductance-based neurons (single-units) and afterwards also between the sums of ten responses (multi-units) of this neuron type. We will finish with the coherence analysis of experimental data.

### 2.2.1 Poisson Model and Coherences

In the simple model (Fig. 2.1) we feed Poisson neurons with partially common rate fluctuations $N_c\sigma\eta_0(t)$ and uncorrelated noise $(1-N_c)\sigma\eta_i(t)$ (as described below), in order to translate the local field potential into a series of (partially) correlated spike trains. For this part of the model, we will derive analytical expressions for the coherence between LFP and single or multi-unit activity and for the coherence between spike trains. The spike output of the Poisson neurons is fed into a set of neurons, which could be conductance-based leaky integrate-and-fire neurons, or conductance-based Hodgkin-Huxley neurons.

The Poisson neurons each receive an input

$$x_i(t) = \lambda + N_c\sigma\eta_0(t) + (1-N_c)\sigma\eta_i(t) \tag{2.1}$$

with a constant input $\lambda$, Gaussian colored noise $\eta_0$, and Gaussian white noise $\eta_i$, with $< \eta_i(t)\eta_j(t+\tau) >= \delta_{ij}(\tau)$. The common input ratio $N_c$ varies from zero (uncorrelated input to all neurons) to one (the same input to all neurons). Both $\eta_0(t)$ and $\eta_i(t)$ have zero mean and a variance of one. In this study, $\sigma$ is set to $\lambda/3$ so, that the total input to the neurons is always positive and, therefore, the probability that a spike occurs, too.

Experiments in visual cortex (Fries et al., 2001a,b, 2005) have shown that the local field potential, which represents a measure of the local correlated input to a group of neurons (Buzsáki, 2004), has a peak in the power spectrum in the range between 40 and 60 Hz. Therefore, we used bandpass-filtered Gaussian white noise $\eta_0(t)$ as a time-dependent common rate fluctuation, which was obtained by filtering Gaussian white noise with a bandpass filter with 3 dB points at 45 and 55 Hz and a quality factor Q of 5.

The response of Poisson neuron $i$ to the input $x_i(t)$ is represented by a sequence of action potentials $y_i(t) = \sum_j \delta(t - t_j^i)$, where $\delta$ is the Dirac $\delta$ function and $t_j^i$ represents the occurrence time of the $j^{th}$ spike of neuron $i$. In this study, we will introduce a discretisation of time in bins $\Delta t$ of 1 ms, such that $y_i(t) = 1$ for an action potential in the time interval $[t, t + \Delta t)$ with probability $x_i(t)\ \Delta t$ and with $y_i(t) = 0$ with probability $(1 - x_i(t)\ \Delta t)$. Multi-unit activity is defined as the sum of $m$ single-unit activities $z(t) = \sum_{i=1}^{m} \sum_j \delta(t - t_j^i)$.

A commonly used measure to estimate the relation between input x(t) and output y(t) of a neuron is the normalised cross covariance function or correlation coefficient function, which is defined by (Marmarelis and Marmarelis, 1978)

$$\rho_{xy}(\tau) \equiv \frac{C_{xy}(\tau)}{\sqrt{C_{xx}(0)\ C_{yy}(0)}} \tag{2.2}$$

with the cross covariance function between two signals $x$ and $y$ defined as

$$C_{xy}(\tau) = \int\int x(t+\tau)\ y(t)\ p(x(t+\tau), y(t))\ dx(t+\tau)\ dy(t) - \bar{x}\,\bar{y} \tag{2.3}$$

where $p(x(t+\tau), y(t))$ is the joint probability distribution of $x(t+\tau)$ and $y(t)$ and where $\bar{x}$ and $\bar{y}$ represent the averaged value of signal $x$ and $y$, respectively.

The coherence function $\gamma(\omega)$ reflects how much of the variations in the output $y$ can be attributed to a linear filtering of the input signal $x$. The coherence function $\gamma(\omega)$ is defined by:

$$\mid \gamma(\omega) \mid = \frac{\mid C_{xy}(\omega) \mid}{\sqrt{\mid C_{xx}(\omega) \mid} \sqrt{\mid C_{yy}(\omega) \mid}} \tag{2.4}$$

The coherence takes values in the range between 0 (input and output are fully uncorrelated) and 1 (the output is equal to the input after convolution by a linear system).

First, we will determine the coherence between single-unit activity of a Poisson neuron and the common rate fluctuations by deriving expressions for the covariance

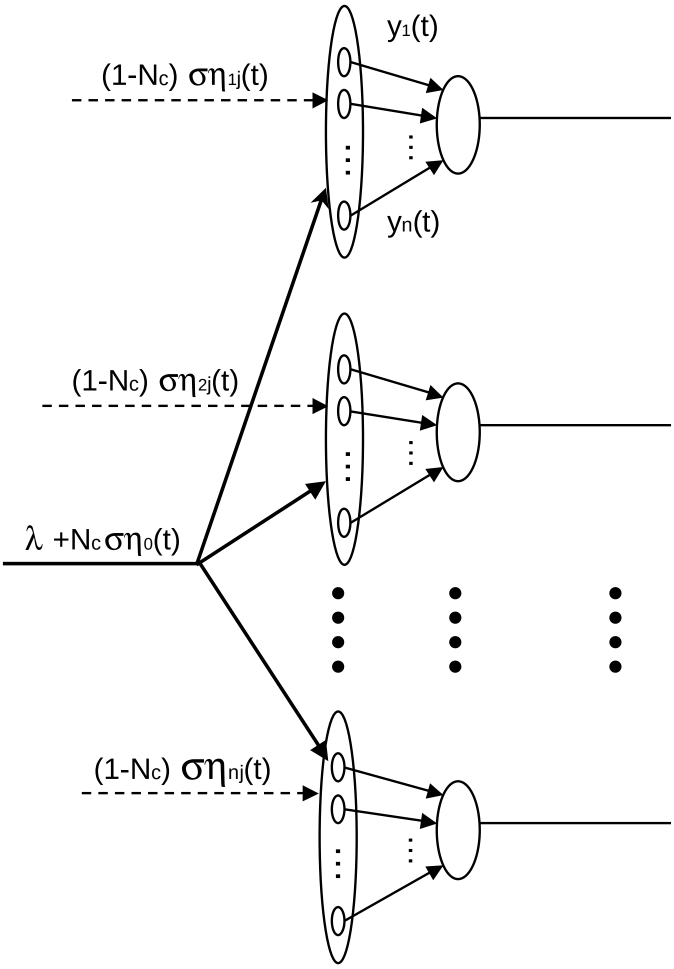

Figure 2.1: Schematic overview of the network of neurons for the simulations. A set of Poisson neurons receives common rate fluctuations (local-field potential) and uncorrelated input to generate a set of correlated spike trains. These spike trains provide the input for a set of neurons, which are modelled as leaky integrate- and-fire (LIF) neurons or Hodgkin-Huxley (HH) neurons.
A population of Poisson neurons is represented by an oval with small circles. Each Poisson neuron receives a common input given by $\lambda + N_c\sigma\eta_o(t)$ and an unique input given by $(1-N_c)\sigma\eta_{ij}(t)$, which is uncorrelated in time and space. $\lambda$ is a constant, $\eta_0$ represents the common rate fluctuations to the Poisson neurons and is represented by band-pass filtered Gaussian white noise, $\eta_{i,j}$ is Gaussian white noise for the $j^{th}$ Poisson neuron of the $i^{th}$ population.
**Poisson model**: Only one population of 20 Poisson neurons is used for the Poisson model. $y_i(t)$ represents the single-unit activity of Poisson neuron $i$, multi-unit activity is the sum of the responses of ten neurons.
**LIF (HH) model**: Each of the 20 LIF (HH) neuron (large circle) receives input from one of the 20 populations with 100 Poisson neurons each (oval). Single-unit activity is the response of one conductance-based neuron, multi-unit activity is the sum of ten single-unit activities.

functions in the denominator and the cross covariance function in the nominator of Eq. 3.2.

Consider $x(t)$ to be the input given by equation 2.1 and $y_i(t) = y(t)$ the response of a single Poisson neuron. Each Poisson neuron is represented by a small circle in Fig. 2.1. The covariance function of the input is given by:

$$\begin{aligned} C_{xx}(\tau) &= \int\int x(t)x(t+\tau)p(x(t),\, x(t+\tau))dx(t)dx(t+\tau) \\ &= \int\int\int\int x(t)\, x(t+\tau)p(\eta_0(t),\eta_0(t+\tau))\; p(\eta_i(t),\eta_i(t+\tau)) \\ &\qquad d\eta_0(t)d\eta_0(t+\tau)d\eta_i(t)d\eta_i(t+\tau) - \bar{x}^2 \\ &= N_c^2\, \sigma^2\, \rho(\tau) + (1-N_c)^2\sigma^2\delta(\tau) \end{aligned} \tag{2.5}$$

where the joint probability distributions for $\tau \neq 0$ are given by (Marmarelis and Marmarelis, 1978)

$$\begin{aligned} p(\eta_0(t+\tau),\eta_0(t)) &= \frac{1}{2\pi\sqrt{1-\rho^2(\tau)}} \\ &\quad \exp\left(-\frac{\eta_0^2(t+\tau) - 2\rho(\tau)\eta_0(t+\tau)\eta_0(t) + \eta_0^2(t)}{2(1-\rho^2(\tau))}\right) \\ p(\eta_i(t+\tau),\eta_i(t)) &= p(\eta_i(t))\; p(\eta_i(t+\tau)) \end{aligned} \tag{2.6}$$

with $\rho(\tau) = \rho_{\eta_0\eta_0}(\tau)$ being the normalised covariance function of the Gaussian coloured noise $\eta_0$. In order to obtain Eq. 2.5 we used for the common input coloured noise $\eta_0(t)$ and for the uncorrelated noise $\eta_i(t)$ in the input signal $x(t)$ defined in Eq. 2.1 for $\tau = 0$

$$\begin{aligned} \int \eta_o(t+\tau)\; p(\eta_0(t+\tau),\eta_0(t) \mid \tau)\; d\eta_0(t+\tau) &= \eta_0(t)\; p(\eta_0(t)) \\ &= \frac{\eta_0(t)}{\sqrt{2\pi}} \exp\left(-\frac{\eta_0^2(t)}{2}\right) \\ \int \eta_i(t+\tau)\; p(\eta_i(t+\tau),\eta_i(t) \mid \tau)\; d\eta_i(t+\tau) &= \eta_i(t)\; p(\eta_i(t)) \\ &= \frac{\eta_i(t)}{\sqrt{2\pi}} \exp\left(-\frac{\eta_i^2(t)}{2}\right) \end{aligned} \tag{2.7}$$

The first term at the r.h.s. of Eq. 2.5 is due to the common rate fluctuations to the neurons, the second term due to the neuron specific input fluctuations.

The covariance function of a single-unit response results in:

$$\begin{aligned}
C_{yy}(\tau) &= p(y(t+\tau)=1, y(t)=1) - \bar{y}^2 \\
&= \int\int\int\int p(y(t+\tau)=1 \mid \eta_0(t+\tau), \eta_i(t+\tau))\; p(y(t)=1 \mid \eta_0(t), \eta_i(t)) \\
&\quad\; p(\eta_0(t), \eta_0(t+\tau))\; p(\eta_i(t), \eta_i(t+\tau)) d\eta_0(t) d\eta_0(t+\tau) d\eta_i(t) d\eta_i(t+\tau) - \bar{y}^2 \\
&= \Delta t^2 \sigma^2 N_c^2 (\rho(\tau) - \delta(\tau)) + \Delta t\; \lambda (1 - \Delta t\; \lambda) \delta(\tau) \qquad (2.8)
\end{aligned}$$

where $\rho$ is the normalised covariance function of the Gaussian coloured noise.

The cross covariance function between the input $x$ and the single-unit response $y$ is given by

$$\begin{aligned}
C_{xy}(\tau) &= \int x(t+\tau) p(x(t+\tau), y(t)=1 \mid \tau)\; dx(t+\tau) - \bar{x}\,\bar{y} \\
&= \Delta t \sigma^2 N_c^2 \rho(\tau) + \Delta t \sigma^2 (1 - N_c)^2 \delta(\tau) \qquad (2.9)
\end{aligned}$$

The first term at the r.h.s. is due to the common rate fluctuations, the second term due to the neuron specific input fluctuations.

The local field potential is considered to be a measure of the local common rate fluctuation of the neurons near the recording electrode. Therefore, we will take only the contributions of the common rate fluctuations in Eqs. 2.5 and 2.9 into account for determining an analytical expression for the Spike-Field coherence between single-unit activity and local field potential. The Spike-Field coherence between the single-unit activity and the common rate fluctuations can be obtained by taking the Fourier transform of Eq. 2.8 and the first terms at the r.h.s. of Eqs. 2.5 and 2.9. This results in:

$$\begin{aligned}
\mid \gamma^{SU}_{Sp\;F}(\omega) \mid &= \frac{\Delta t\; \sigma^2 N_c^2 \mid \rho(\omega) \mid}{\sigma N_c \sqrt{\mid \rho(\omega) \mid \mid \Delta t \lambda (1 - \Delta t \lambda) + (\Delta t\; \sigma)^2 N_c^2 (\rho(\omega) - 1) \mid}} \\
&= \frac{\Delta t\; \sigma N_c \sqrt{\mid \rho(\omega) \mid}}{\sqrt{\mid \Delta t\; \lambda (1 - \Delta t\; \lambda) + (\Delta t \sigma)^2 N_c^2 (\rho(\omega) - 1) \mid}} \\
&\approx \frac{\Delta t\; \sigma N_c}{\sqrt{\Delta t\; \lambda}} \sqrt{\mid \rho(\omega) \mid} \qquad (2.10)
\end{aligned}$$

where $\rho(\omega)$ is the Fourier transform of the normalised covariance function of the coloured noise. The approximation in the last step is valid since $(\Delta t\; \sigma)^2 << \Delta t\; \lambda$.

In order to obtain an expression for the coherence between multi-unit activity and the common rate fluctuations, we have to determine the covariance function of multi-unit activity and the cross covariance function between multi-unit activity and common rate fluctuations. Since the probability that a neuron fires twice within a time bin $\Delta t$ is very small ($(\Delta t\ \lambda)^2 << 1$), we only take terms up till the second order of $\Delta t$ into account. For multi-unit activity $z$, which is the summation over $m$ simultaneously recorded single-unit signals $y_i(t)$ with a common input ratio $N_c$ and for $m << \frac{1}{\Delta t\ \lambda}$, we find for the multi-unit covariance function:

$$\begin{aligned} C_{zz}(\tau) &= \sum_{j=0}^{m}\sum_{k=0}^{m} j\ k\ p(z(t+\tau)=j, z(t)=k) - \bar{z}^2 \\ &\approx m\ (\Delta t)^2\sigma^2 N_c^2(m\ \rho(\tau)-\delta(\tau)) + m\ \Delta t\ \lambda(1-\Delta t\ \lambda)\ \delta(\tau) \end{aligned} \quad (2.11)$$

The cross covariance function between multi-unit activity and the total input is given by:

$$\begin{aligned} C_{xz}(\tau) &= \sum_{j=0}^{m}\int x(t+\tau)\ j\ p(x(t+\tau), z(t)=j)\ dx(t+\tau) - \bar{x}\,\bar{z} \\ &\approx m\ \Delta t\sigma^2\ N_c^2\ \rho(\tau) + m\ \Delta t\ \sigma^2(1-N_c)^2\delta(\tau) \end{aligned} \quad (2.12)$$

Eq. 2.12 is equal to Eq. 2.9 except for the factor $m$.

Combining equation Eq. 2.11 and the first term at the r.h.s. of Eqs. 2.5 and 2.12 leads to the expression for the Spike-Field coherence between multi-unit activity and the common rate fluctuations:

$$\begin{aligned} \mid \gamma_{SpF}^{MU}(\omega) \mid &\equiv \frac{\mid C_{xz}(\omega) \mid}{\sqrt{\mid C_{xx}(\omega) \mid}\sqrt{\mid C_{zz}(\omega) \mid}} \\ &\approx \frac{\Delta t\ \sigma N_c\sqrt{\mid m\rho(\omega) \mid}}{\sqrt{\mid \Delta t\ \lambda(1-\Delta t\ \lambda) + (\Delta t\sigma)^2 N_c^2(m\rho(\omega)-1) \mid}} \\ &\approx \frac{\Delta t\ \sigma N_c}{\sqrt{\Delta t\ \lambda}}\sqrt{\mid m\rho(\omega) \mid} \end{aligned} \quad (2.13)$$

The Spike-Field coherence for multi-unit activity, which is the summation of $m$ single-unit recordings, is equal to that for single-unit activity (Eq. 2.10) except for a coefficient $\sqrt{m}$.

We can also calculate the coherence between two single-unit responses or between two multi-unit recordings. The cross covariance function between two single-unit signals $y_1$ and $y_2$ is given by:

$$\begin{aligned} C_{y_1 y_2}(\tau) &= p(y_1(t+\tau)=1, y_2(t)=1) - \overline{y_1}\,\overline{y_2} \\ &= (\Delta t\ \sigma)^2 N_c^2\rho(\tau) \end{aligned} \quad (2.14)$$

The Spike-Spike coherence between two simultaneously recorded single-unit signals with partly common rate fluctuations is given by:

$$
\begin{aligned}
\mid \gamma_{SpSp}^{SU} \mid &\equiv \frac{\mid C_{y_1 y_2}(\omega) \mid}{\mid C_{yy}(\omega) \mid} \\
&= \frac{(\Delta t\ \sigma)^2\ N_c^2 \mid \rho(\omega) \mid}{\Delta t\ \lambda(1-\Delta t\ \lambda)+(\Delta t\ \sigma)^2 N_c^2(\rho(\omega)-1)} \\
&\approx \frac{(\Delta t\ \sigma\ N_c)^2}{\Delta t\ \lambda} \mid \rho(\omega) \mid
\end{aligned}
\tag{2.15}
$$

where we used $C_{yy} = C_{y_1 y_1} = C_{y_2 y_2}$.

The cross covariance function of two multi-unit signals is given by:

$$
\begin{aligned}
C_{z_1 z_2}(\tau) &= \sum_{j,k=0}^{m} j\ k\ p(z_1(t+\tau)=j, z_2(t)=k \mid \tau) - \bar{z}^2 \\
&\approx m^2\ N_c^2 (\Delta t\ \sigma)^2\ \rho(\tau)
\end{aligned}
\tag{2.16}
$$

The Spike-Spike coherence between two simultaneously recorded multi-unit signals is given by:

$$
\begin{aligned}
\mid \gamma_{SpSp}^{MU} \mid &= \frac{m^2 (\Delta t\ \sigma)^2\ N_c^2 \mid \rho(\omega) \mid}{\mid m^2\ (\Delta t \sigma)^2 N_c^2 \rho(\omega) + m\ (\Delta t\ \lambda(1-\Delta t\ \lambda)-(\Delta t\ \sigma)^2\ N_c^2) \mid} \\
&\approx \frac{m(\ \Delta t\ \sigma)^2\ N_c^2 \mid \rho(\omega) \mid}{\mid \Delta t\ \lambda(1-\Delta t\ \lambda)+(\Delta t\ \sigma)^2 N_c^2(m\rho(\omega)-1) \mid} \\
&\approx \frac{(\Delta t\ \sigma\ N_c)^2}{\Delta t\ \lambda} m \mid \rho(\omega) \mid
\end{aligned}
\tag{2.17}
$$

Equations 2.15 and 2.17 show that for low firing rates ($\lambda\ \Delta t << 1$) and for $m << 1/(\lambda\ \Delta t)$ the expected Spike-Spike coherence between multi-unit signals is approximately $m$-times larger than the expected Spike-Spike coherence between single-unit signals. Equations 2.13 and 2.17 show that the Spike-Spike coherence is (approximately) the square of the Spike-Field coherence and thus much smaller.

In summary, for the Poisson model, the Spike-Field coherence and the Spike-Spike coherence are larger for multi-unit recordings than for single-unit recordings and the Spike-Spike coherences are much smaller than the Spike-Field coherences.

### 2.2.2 Conductance-based LIF Model

Since the simple Poisson model is not very realistic, we will discuss a model where conductance-based leaky integrate-and-fire neurons (LIF) receive spike input from the Poisson neurons. The membrane equation of the neurons is then given by

$$C\frac{dU}{dt} = -I_e(t) - I_l(t) \tag{2.18}$$

with membrane capacitance $C$, membrane potential $U$ and excitatory and leak currents $I_e$ and $I_l$, respectively. These currents are given by

$$\begin{aligned} I_e(t) &= G_e(t)(U(t) - E_e) \\ I_l(t) &= G_l(U(t) - E_r) \end{aligned} \tag{2.19}$$

with the excitatory reversal potential $E_e$, rest potential $E_r$ and excitatory (leak) conductance $G_e(t)$ ($G_l$). The excitatory conductance depends on the recent pre-synaptic spike-times and is modelled by:

$$G_e(t) = \sum_{i=1}^{m} \sum_{k=1}^{k_i^{max}} g_e(t - t_i^k) \tag{2.20}$$

with $t_i^k$ the time of the $k^{th}$ spike of neuron $i$ and with $m$ the number of input neurons. In this study, the conductivity is modelled by an alpha function:

$$g_e(t) = g_0 \left(\frac{t}{\tau_e}\right) \exp\left(-\frac{t}{\tau_e}\right) \Theta(t) \tag{2.21}$$

Here $\tau_e$ denotes the time-to-peak of the conductivity $g_e(t)$. $\Theta$ is the Heaviside function. When the membrane potential reaches the threshold $U_{thr}$, a spike will be generated and the membrane potential $U$ is reset. Specific values for the LIF model are (Stroeve and Gielen, 2001): membrane capacitance $C = 325$ pF, threshold potential $U_{thr} = -55$ mV, excitatory reversal potential $E_e = 0$ mV, rest potential $E_r = -75$ mV, leak conductance $G_l = 25$ nS, $g_0 = 3.24$ nS and $\tau_e = 1.5$ ms.

Each LIF neuron (large circle in Fig.1) receives input from a population of 100 Poisson neurons (oval), with a spike-rate output modulated by a common input $(\lambda + N_c\ \sigma\ \eta_0(t))$ and an uncorrelated input ( $(1 - N_c)\ \lambda + \sigma\ \eta_i(t))$, where $\eta_0(t)$ is Gaussian coloured noise and $\eta_i(t)$ is Gaussian white noise, both with zero mean and variance one. For the simulations, these quantities are chosen as for the Poisson model except for $\sigma$, which has been chosen by $\sigma = 20/12$, for $\lambda = 20$. In our simulations, we derived the membrane potential by using Euler Integration with a step width of 1 ms.

### 2.2.3 Conductance-based Hodgkin-Huxley Model

The next modification of the simple model (Fig.1) is the replacement of the conductance-based LIF-neurons (circles) by conductance-based Hodgkin-Huxley neurons. These neurons are characterised by the differential equation:

$$C\frac{dU}{dt} = -I_{Na}(t) - I_K(t) - I_l(t) - I_e(t) \tag{2.22}$$

where the sodium and potassium currents are given by:

$$\begin{aligned} I_{Na}(t) &= g_{Na}m^3h(U(t) - V_{Na}) \\ I_K(t) &= g_K n^4(U(t) - V_K) \end{aligned} \tag{2.23}$$

and the leak and excitatory currents as described before (see Eq. 2.19). $V_{Na}$ and $V_K$ are the sodium and potassium reversal potentials. The time-varying gate variables $m$, $h$ and $n$ are given by the differential equation

$$\frac{dx}{dt} = \frac{x_\infty - x}{\tau_x} \tag{2.24}$$

with $x\varepsilon\{m,h,n\}$, $\tau_x = \frac{1}{\alpha_x+\beta_x}$ and $x_\infty = \frac{\alpha_x}{\alpha_x+\beta_x}$
These parameters are expressed by:

$$\begin{aligned} \alpha_m &= 0.1\frac{U+40}{1-\exp(-0.1(U+40))} \\ \beta_m &= 4\exp(-(U+65)/18) \\ \alpha_n &= \frac{0.01(U+55)}{1-\exp(0.1(U+55))} \\ \beta_n &= 0.125\exp(-(U+65)/80) \\ \alpha_h &= 0.07\exp(-(u+65)/20) \\ \beta_h &= \frac{1}{1+\exp(-0.1(U+35))} \end{aligned} \tag{2.25}$$

The typical values of the parameters at 6.3°C for the squid axon are: membrane capacitance per unit surface $C = 1$ $\mu$F/cm$^2$, maximum conductance per unit area for the sodium, potassium and leak currents, $g_{Na} = 120$ mS/cm$^2$, $g_K = 36$ mS/cm$^2$, $G_l = 0.3$ mS/cm$^2$, excitatory reversal potential $E_e = 0$ mV, rest potential $E_r = -75$ mV, sodium reversal potential $V_{Na} = 50$ mV, potassium reversal potential $V_K = -77$ mV, $g_0 = 1.5$ $\mu$S/cm$^2$ and $\tau_e = 1.5$ ms.

Like for the conductance-based LIF model, we use spike trains as input for the conductance-based HH neurons. We derived the membrane potential using Euler Integration with a step width of 0.05 ms for the HH-neurons. The sequence of output action potentials of the HH model was represented in time bins of 1 ms.

### 2.2.4 Multitaper Method

The usual way of estimating the frequency content of a signal is by taking the Fourier spectrum (periodogram). If the signal x(t) has a stochastic character, the variance of the spectral estimates in the Fourier transformed signal may be considerable. This is particularly important if we are dealing with the coherence of two stochastic spike series. This is not solved by taking a signal with a longer duration since a longer time signal gives rise to a higher spectral resolution in the Fourier transformed signal, but does not decrease the variance of each point in the frequency spectrum.

To solve this problem, the multitaper estimation procedure was introduced (see Thomson, 1982; Mitra and Pesaran, 1987). The key idea behind the Welch method and the multitaper method is that a physiological signal has no discontinuities in the frequency spectrum and that the variability in the estimate of a signal can be reduced by smoothing in the frequency domain. The multitaper method achieves this by optimising the minimum of bias and variance of the estimate. This involves the use of multiple orthonormal data tapers, which provide a local eigenbasis in frequency space for finite length data sequences. A simple example of the method is given by the direct multitaper spectral estimate $S_{MT}(f)$ of a discrete time series signal $x_t$ with $t = n\Delta t$ and $n \in 1,2,..,N$ defined as the average over individual tapered spectral estimates,

$$S_{MT}(f) = \frac{1}{N}\sum_{k=1}^{K} \mid \tilde{x_k}(f) \mid^2 \tag{2.26}$$

where

$$\tilde{x_k}(f) = \sum_{t=1}^{N} w_t(k) x_t \exp(-2\pi i f t) \tag{2.27}$$

Here $w_t$(k) (k = 1,2,...,K) are K orthogonal taper functions with appropriate properties. Let $w_k(k,W,N)$ be the k-th taper of length N and frequency bandwidth parameter W. This forms an orthogonal basis set for sequences of length N, characterised by a bandwidth W. The important feature of these sequences is that for a given bandwidth parameter W and taper length N, K=2NW-1 sequences out of a total of N each have their energy effectively concentrated within a range 2W in frequency space. This range can be shifted from [-W,W] centred around zero frequency to any nonzero centre frequency interval $[f_0 - W, f_0 + W]$ by simply multiplying by the appropriate phase factor $\exp(2\pi f_0 t)$. The product of the number N of samples in the signal and the bandwidth W of the spectral estimator (NW) is used to balance between variance and resolution of the power spectral density estimation. In this article, we use a simple set of orthonormal sine tapers $\{\omega_{t,k} : t = 1,..,N; k = 0,..,N-1\}$

(McCoy et al., 1997). The k-th taper is given by:

$$\omega_{t,k} = \sqrt{\frac{1}{N+1}} \sin\left(\frac{(k+1)\pi t}{N+1}\right) \tag{2.28}$$

For the analysis, we used signals of length 0.512 s and the first $K = 2NW - 1$ tapers, which gave $K = 6$. This means that the bandwidth W of the spectral estimator is 6.83 Hz. The frequency binwidth is $f_s/\text{nfft}= 1.95$ Hz, with sampling frequency $f_s$ (1000 Hz) and where nfft is the number of data in the FFT (512).

### 2.2.5 Neurophysiology

**SURGERY** Experiments were performed on two male Macaca mulatta, weighting 8-11 kg. Each monkey was surgically implanted with a head post, a scleral eye coil, and a recordings chamber. Surgery was conducted under aseptic conditions with isofluorane anesthesia. Antibiotics and analgesics were administered after the operation. The skull remained intact during the surgery. Subsequently, small holes ($\sim$5 mm in diameter) were drilled within the recording chamber under ketamine anesthesia and xylazine analgesic. All experimental procedures were performed in accordance with the National Institute of Health guidelines and approved by the National Institute of Mental Health Intramural Animal Care and Use Committee.

**RECORDING TECHNIQUE** Neuronal recordings were made through the surgically implanted chamber overlying area V4. Recordings were made from two hemispheres in two monkeys. Four to eight tungsten microelectrodes (Frederick Haer and Co., Brunswick, ME) were inserted through the intact dura mater by means of a hydraulic microdrive (Frederick Haer) mounted to the recording chamber. The electrodes had tip impedances of one to two MΩ and were separated by 650 or 900 mm. Each electrode was advanced separately at a very slow rate (1.5 mm/s) to minimise suppression artifacts (dimpling) resulting from the deformation of the cortical surface by the electrode. Data amplification, filtering and acquisition was done with a Multichannel Acquisition Processor (MAP) system from Plexon Incorporated (Dallas, TX). The signal from each electrode was passed through a headstage with unit gain and an output impedance of 240 Ω. It was then split to separately extract the spike and the LFP components. For spike recordings, the signals were filtered with a passband of 100 - 8000 Hz, further amplified and digitised with 40 kHz. A threshold was set interactively and spike waveforms were stored for a time window from 150 $\mu$s before to 700 $\mu$s after threshold crossing. The threshold clearly separated spikes from noise, but was chosen to include multi-unit activity. Offline, a principal component analysis of the waveforms was performed and the first against the second principal component were plotted. Those waveforms that corresponded to artifacts were excluded. For multi-unit analyses, all other waveforms were accepted. For single-unit analyses, only clearly isolated clusters of high-amplitude spikes were accepted. For all further analyses involving spikes, only the times of threshold crossing were kept and downsampled to 1 kHz. For LFP recordings, the signals were filtered with a passband of 0.7-170 Hz, further amplified and digitised at 1 kHz.

Each electrode was lowered separately until it recorded visually driven activity. Once this had been achieved for all electrodes, the electrode positions were fine-tuned to optimise the signal-to-noise ratio of the multiple spike recordings and to obtain as many isolated single-units as possible. Since the penetration was halted as soon as clear visually driven activity was obtained, most of the recordings were presumably done from the superficial layers of the cortex.

**BEHAVIOURAL PARADIGM AND VISUAL STIMULATION** Stimuli were presented on a 17 inch CRT monitor 0.57 m from the monkey's eyes that had a resolution of 800 × 600 pixel and a screen refresh rate of 120 Hz non-interlaced. Stimulus generation and behavioural control were accomplished with the CORTEX software package (http://www.cortex.salk.edu/). A trial started when the monkey touched a bar mounted in front of him and 250 ms later, a fixation point appeared at the centre of the screen. When the monkey brought his gaze within 0.7° of the fixation spot for at least 1000 ms, stimulus presentation commenced. The task of the monkey was to fixate the fixation target while a drifting sine wave grating was presented within the receptive field. He had to release the bar between 150 and 650 ms after a change in stimulus colour of the sine-wave grating. That change in stimulus colour could occur at an unpredictable moment in time between 500 and 5000 ms after stimulus onset. With this task, we assured that the monkey was constantly monitoring the grating that induced the recorded neuronal activity while fixating the fixation target. The first 300 ms after stimulus-onset were discarded in order to avoid strong stimulus onset related transients and the rest of the data were analysed until the time of the colour change. Successful trial completion was rewarded with four drops of diluted apple juice. If the monkey released the bar too early or if he moved his gaze out of the fixation window, the trial was immediately aborted and followed by a timeout.

## 2.3 Results

In this section we will describe coherence estimates between various signals. We always first analyse the Spike-Field coherence followed by the Spike-Spike coherence, for both single-unit and multi-unit activity. The simulation results will be shown first for the Poisson model neurons (small circles in Fig. 2.1), followed by the conductance-based neurons (LIF and HH; big circles in Fig. 2.1). We will end this section with the results of the Spike-Field and Spike-Spike coherences of experimental data. Finally we compare an analysis without and with the use of multitaper techniques.

### 2.3.1 Simulation results of the Poisson model

The top panels of Fig. 2.2 show the predicted (dashed line) and the simulated (solid line) coherence between the LFP and single-unit activity (Fig. 2.2A) and between LFP and multi-unit activity (Fig. 2.2B) for the Poisson neurons. In both cases, there is a good match between the simulated and predicted Spike-Field coherence functions.

The ”predicted” coherence functions were obtained using the Fourier transform of the normalised covariance function $\rho(\tau)$ of the LFP. Since the LFP had a finite duration, $\rho(\omega)$ has noisy fluctuations which are evident in the ”predicted” coherence function of Fig. 2.2. The coherence is larger for the multi-unit activity (Fig. 2.2B) than for the single-unit activity (Fig. 2.2A). The ratio between the peak coherence for multi-unit versus single-unit activity (0.37/0.12=3.08) is in agreement with the square root of the number of neurons ($\sqrt{10} = 3.16$) that contributes to the multi-unit activity (see Eqs. 2.10 and 2.13). One could argue that the larger coherence for the multi-unit case could be due to the fact that the multi-unit recording with ten (simultaneously measured) single-unit signals contains ten times more action potentials. In order to correct for this, the single-unit signal in our simulations was ten times longer than the multi-unit signal such that the number of action potentials was the same in both signals.

Figure 2.2C shows the simulated (solid line) and predicted (dashed line) Spike-Spike coherence for single-unit activity for the Poisson neurons. Figure 2.2D shows the same results for multi-unit activity. The simulated and predicted coherence are in agreement for the single-unit and multi-unit data.

The Spike-Spike coherence for multi-unit activity increases linearly with the number of units ($m = 10$) in the multi-unit recording for the Spike-Spike coherence as long as $m << 1/(\lambda \ \Delta t)$. This is shown by the peaks of the coherences in Figs. 2.2C and 2.2D (0.015 vs. 0.14).

The Spike-Spike coherence differs from the Spike-Field coherence in two aspects (see equations 2.17 and 2.13). The first difference concerns the factor $m$ versus $\sqrt{m}$ for Spike-Spike versus Spike-Field coherence. The second difference is that the Spike-Field coherence is proportional to $\sqrt{\rho(\omega)}$, whereas the Spike-Spike coherence is proportional to the normalised covariance function of the common rate

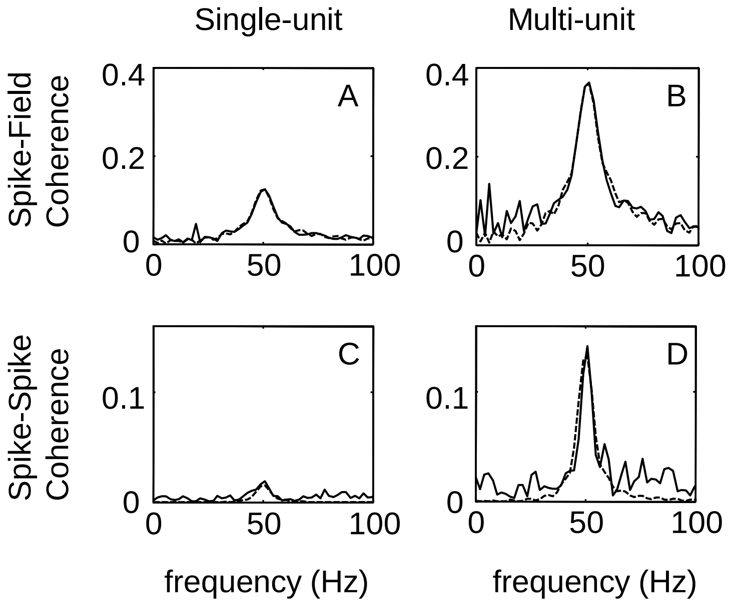

Figure 2.2: Predicted (dashed lines) and simulated (solid lines) coherence functions for LFP and single-unit (A,C) and multi-unit (B,D) signals for the Poisson neurons ( see Fig. 2.1).
Parameter values used were $\lambda = 20$, $\sigma = 20/3$, $N_c = 0.4$, and a simulation duration of 512 s. The number of action potentials in the multi- and in the single-unit signals is about 20 480 spikes.
A) The coherence between LFP and single-unit activity. B) The coherence between LFP and multi-unit activity shows a peak near 50 Hz, which is larger than that for single-unit activity shown in A. C) The predicted and simulated coherences between two single-unit activities. D) The predicted and simulated coherence function between two multi-unit activities.

fluctuations, $\rho(\omega)$. Since $0 <\mid \rho(\omega) \mid< 1$, $\rho(\omega)$ is smaller and more narrow than $\sqrt{\rho(\omega)}$.

Both aspects are reproduced in Fig. 2.2. The peak value of the Spike-Spike coherence (fig. 2.2D: 0.14) is approximately the square root of the maximum peak value of the Spike-Field coherence (fig. 2.2B: 0.37).

Equations 2.10, 2.13, 2.15 and 2.17 for the Spike-Field and Spike-Spike coherence do not depend on the duration of the LFP and spike series. Therefore, the expectation value for the coherence functions will not change if the duration of the single-unit recordings increases. The only effect of a longer duration of the spike

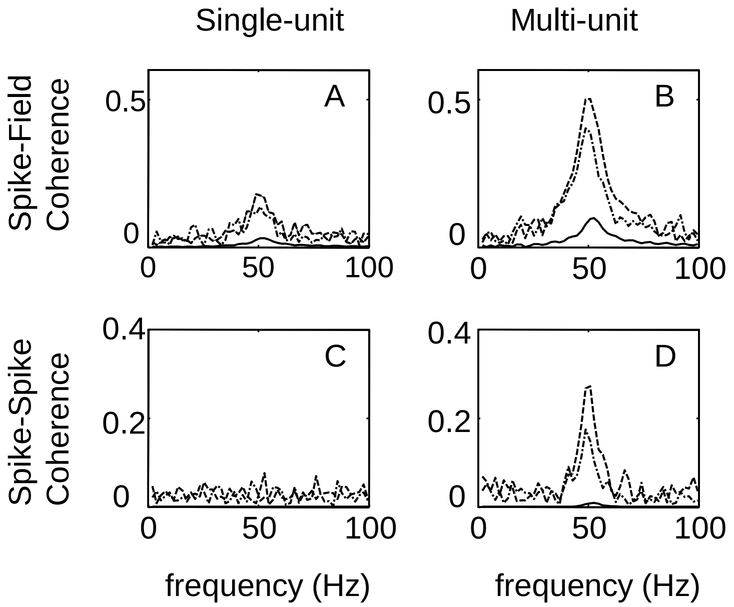

Figure 2.3: Coherences between LFP and single-/multi-unit activities for the conductance-based LIF model (dashed-dotted lines), the HH model (dashed lines) and the predictions for the Poisson model (solid line) according to Eqs. 2.10 ,2.13, 2.15 and 2.17. Parameter values used were $\lambda = 20$, $\sigma = 20/12$, $N_c = 0.4$, and a simulation duration of 512 s.

A) Spike-Field coherence estimates for single-unit activity. B) Spike-Field coherence estimates for multi-unit activity. C) Spike-Spike coherence estimates for single-unit activity. D) Spike-Spike coherence estimates for multi-unit activity.

recording is a reduction of the noise in the coherence function. Therefore, a smaller coherence for single-unit recording relative to multi-unit recording can not be compensated by a longer recording time for the single-unit recordings.

### 2.3.2 Simulation results for the conductance-based LIF and HH model

Figure 2.3 shows the Spike-Field and the Spike-Spike coherences for single-unit and multi-unit recordings for the conductance-based LIF-neuron (dashed-dotted line), the conductance-based HH-neuron (dashed line) model and the predictions for the Poisson model (solid line) according to Eqs. 2.10, 2.13, 2.15 and 2.17, all with $\sigma = 20/12$. The parameters were chosen in such a way that the mean firing rate was the same for the Poisson neuron, the LIF and the HH-neurons. Figure 2.3A

( 2.3B) shows the coherence between the LFP and single-unit (multi-unit) activity. Both, for the single- and multi-unit recordings, the Spike-Field coherence estimate shows a significant peak near 50 Hz. The peak value of the Spike-Field coherence estimates for multi-unit recording (Fig. 2.3B) is considerably higher than the peak value for the single-unit recording (Fig. 2.3A). The Spike-Field coherence estimates for the LIF and HH network have much higher values than the Spike-Field estimates of the Poisson network. The ratio of the two peak Spike-Field coherence values (multi-unit/single-unit) is smaller than the square root of the number $m$ ($m = 10$; $\sqrt{m} = 3.16$) of neurons active in the multi-unit.

Figure 2.3C ( 2.3D) shows the coherence between two single-unit (multi-unit) recordings. For the single-unit recordings, no significant peak near 50 Hz is visible. The predicted coherence for the Poisson model is small and lies almost on the x-axis, with a small (hardly visible) peak near 50 Hz for the multi-unit activity. For multi-unit activity (Fig. 2.3D), a significant peak near 50 Hz is visible.

The peak coherence is larger for the LIF neuron and the HH model than for the Poisson neuron, both for the Spike-Field coherence as well as for the Spike-Spike coherence. The question is whether the higher coherence values for the LIF and HH neuron are due to the dynamics of these neurons or due to the different type of input (continuous LFP-signal for the Poisson neurons versus spike input to the LIF and HH neuron). In order to investigate this, we have calculated the coherence between the spike input to the LIF and HH neuron (i.e. the sum of spike series of the Poisson neurons) and their output. These coherence values are much higher than the coherence between the input and the output of a Poisson neuron, with the same input as the LIF and HH neuron. Therefore, we conclude that the higher coherence values of the LIF and HH neuron are the result of the dynamic properties of those neuron types.

### 2.3.3 Data from monkey visual cortex

As a final test of the significance of the model simulations, we have analysed data obtained in monkey visual cortex (Fries et al., 2001b). The data consisted of single- and multi-unit activity and local field potential activity recorded simultaneously in area V4 of the awake macaque monkey.

Figure 2.4A shows the coherence between the measured LFP and the single-unit signal, which contains 15 371 spikes. The dashed-dotted lines indicate the 95% confidence levels of the coherence estimates, calculated with 130 bootstraps, the solid line is the average of the bootstrap replications. For a multi-unit recording with a similar number (n=16 031) of spikes and thus a shorter duration, the Spike-Field coherence is shown in Fig. 2.4B. In both Fig. 2.4A and 2.4B, there is a peak in Spike-Field coherence near 50 Hz. For multi-unit activity (sum of approximately

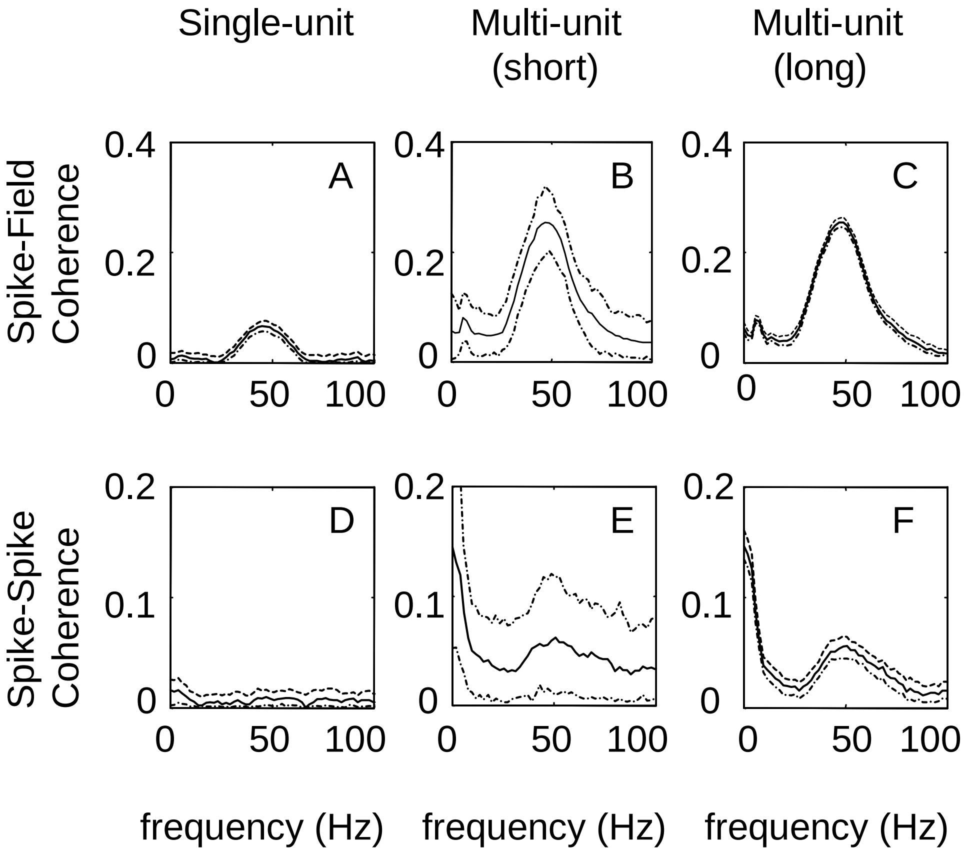

Figure 2.4: Coherences between LFP and single- or multi-unit recordings (experimental data), using the multi taper method.
For the multi taper method we used a set of six orthonormal sine tapers. The 95% confidence level (dashed-dotted lines) is obtained using 130 bootstraps. A) Coherence between LFP and single-unit recording with 15 371 spikes. B) Coherence between LFP and multi-unit recording, with 16 031 spikes. C) Coherence between LFP and multi-unit recording, with 668 766 spikes. D) Coherence between two single-unit recordings. The variance in coherence is too large to detect a significant peak near 50 Hz. E) Coherence between two multi-unit recordings. F) Coherence between two multi-unit recordings, with durations equal to those of the single-unit recordings used in Fig. 2.4A. Compared to Fig. 2.4E the 95% confidence regime has been reduced.

eight single-unit activities), this peak is significantly higher than that for single-unit activity. Fig. 2.4C shows the Spike-Field coherence for a multi-unit signal with a duration equal to the duration of the single-unit recording used for Fig. 2.4A. The coherence estimate, including the 95% confidence level, in Fig. 2.4C is entirely within the 95% regime shown in Fig. 2.4B. Figs. 2.4B and C illustrate that increasing the duration of a spike recording improves the signal-to-noise ratio but does not change the expectation value of the coherence function.

The Spike-Spike coherence for single-unit signals (Fig. 2.4D) does not show a significant peak near 50 Hz. Neither does the Spike-Spike coherence for multi-unit signals, if the analysed time period is shortened such that the number of spikes is the same as in the longer single-unit recording (Fig. 2.4E). The coherence values for the multi-unit signals in Fig. 2.4E are larger than for single-unit signals, shown in Fig. 2.4D. However, the 95% confidence regime is relatively large. Fig. 2.4F shows the Spike-Spike coherence for multi-unit signals with duration equal to the duration of the single-unit activities used in Fig. 2.4D. The coherence function in Fig. 2.4F shows a significant peak near 50 Hz. The signal-to-noise ratio is considerably better than in Fig. 2.4E. The results shown in Fig. 2.4 are typical for the spike signals that were obtained in the study by Fries et al.(2001b).

All coherence estimates of Fig. 2.4 were obtained with the multitaper method as described in the Methods and Theory section. Each trial was cut into equally long segments of 512 ms such, that the number of tapers was constant. In fact this is a combination of the Welch method and the multitaper technique.
As an alternative to using the Welch method with equally long time segments, one could use the multitaper technique for the analysis of spike signals, which in general each have a different duration. Since the trial durations are different, so is the number of samples in each trial. In order to keep the frequency of smoothing in the frequency domain (2W) constant, the number of tapers given by K=2NW-1, is different for each trial. Since averaging over power spectra of different trials requires that the frequency resolution of the spectra should be the same for all trials, all signals (after application of the tapers) are made of equal duration by adding zeros (zero padding). Now the average FFTs of the cross and covariance functions can be derived for the coherence functions.

Figure 2.5A shows the Spike-Spike coherence estimate of experimental multi-unit spike trains without the use of multitapers and without using the Welch method. The frequency resolution in Fig. 2.5 is much higher than that in Fig. 2.4F, because the number of data points in the frequency domain is eight times larger. The variance in the coherence estimate is large and no significant peak is visible near 50 hz.

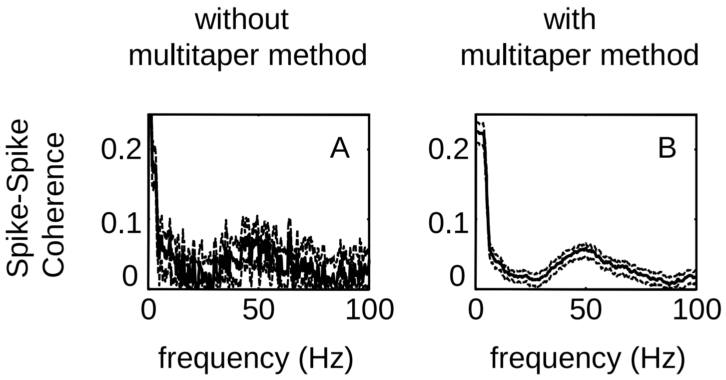

Figure 2.5: The effect of the multitaper method on the Spike-Spike Coherence between multi-units.
A) shows the Spike-Spike coherence estimate of experimental data without the use of multitapers. There is no significant peak near 50 hz. Using the multitaper method with sine-tapers resulted in a significant peak (B) and a significant reduction of the 95% regime.

By applying the multitaper method with $W = 5$ Hz, the variance is reduced and a significant peak near 50 Hz is visible in the same data (see Fig. 2.5B).

## 2.4 Discussion

The coherence between neuronal signals (e.g. EEG, MEG, two spike trains) or between neuronal input (e.g. a local field potential) and neuronal output is generally considered as an important measure for synchronisation or temporal locking. The main result of this study is that the coherence reaches higher values when multi-unit spike activity is used instead of single-unit activity. This cannot be overcome by extending the recording time of the single-unit signal. The latter only improves the signal-to-noise ratio (SNR) of the coherence. The SNR can also be improved by using multitaper techniques or by using the Welch-method. Experimental data obtained in monkey V4 could be reproduced by simulations. The results illustrate the significance of multi-unit activity over single-unit activity, and provide new insights for the interpretation of multi-unit activity and for the interpretation of coherence estimates using oscillatory activity such as $\beta$ and $\gamma$-oscillations, in cognitive neuroscience studies. The results will be discussed in more detail below.

Although many studies have investigated the firing behaviour of Poisson neurons and Integrate-and-Fire neurons for partially correlated and uncorrelated input (for an overview, see Salinas and Sejnowski, 2001), most studies have focussed on the mean firing rate and the coefficient of variation (see e.g. Feng and Brown, 2000; Stroeve and Gielen, 2001; Salinas and Sejnowski, 2000, 2002; Kuhn et al., 2004). The coefficient of variation is an important parameter to understand the temporal structure of spike trains, but this parameter itself cannot provide insight in the temporal correlation of the action potential signals of different neurons receiving partially correlated input. As far as we know, the present study is the first to give analytical expressions and results of computer simulations for the coherence between local-field potential and neuronal firing and for the coherence between spike signals for neurons receiving (partly) correlated input.

In this study, we investigated the relations between Spike-Field and Spike-Spike coherences for single-unit and multi- unit activity. Analytical expressions (Eqs.2.10, 2.13, 2.15 and 2.17) showed that the Spike-Field coherence values are higher than the Spike-Spike coherence values and that the coherences are larger for multi-unit recordings than for single-unit recordings. Although we could only derive analytical expressions for the coherence between input and spike output for the Poisson neurons, simulations show qualitatively similar results for an ensemble of conductance-based LIF neurons or HH neurons.

For Poisson neurons, the Spike-Spike coherence should be proportional to the square of the Spike-Field coherence. This was confirmed by simulations (compare Figs 2.2B and 2.2D) where the spike-spike coherence equals the square of the spike-field coherence for the Poisson model. Figs. 2.3A, 2.3B and 2.3D show similar results for the conductance-based LIF model and for the Hodgkin-Huxley neuron model. The full width at half maximum and the amplitude of the peak are smaller for the Spike-Spike than for the Spike-Field coherence, as expected in case the Spike-Spike coherence is proportional to the square of the Spike-Field coherence, which has values between zero and one. However, coherence values were typically larger for the conductance-based LIF and Hodgkin-Huxley neuron than for the Poisson neuron. This is due to the characteristic dynamic properties of the neuron models.

The results demonstrate that multi-unit activity gives significantly higher estimates for the coherence than single-unit activity, even if the number of action potentials in both signals is the same (see Figs. 2.4A, 2.4B and 2.4D, 2.4E). This is partially due to the fact that the mean firing rate is typically higher in a multi-unit recording than in a single-unit recording and the modulations in firing rate are larger. Eqs. 2.10 and 2.13 show that the coherence decreases with the square root of firing rate (proportional to $\lambda$) but increases linearly with modulation depth $\sigma$. Since firing rate and modulation depth increase proportionally when adding single-unit signals, the coherence will effectively increase with the number of single-unit contributions in a multi-unit signal.

Several studies have reported a lack of evidence for synchronised neuronal activity, see e.g. Tovee and Rolls (1992) in the inferior temporal visual cortex and Luck et al. (1997) who did not observe clear synchronisation in neuronal responses in V2 and V4. This is in contrast to findings by Fries et al. (2001b). The results indicate that the explanation for these apparently contradictory findings may be related to the techniques used to analyse the neuronal data. In figure 2.3C the Spike-Spike coherence between single-unit signals is small and disappears in the relatively high variance of the estimate. Simulations with larger values of $\sigma$ (larger modulations of the stimulus) showed a clear, small and narrow peak near 50 Hz. However, the signal-to-noise ratio increases to plausible levels only for unrealistically high modulations of the input. Therefore, the variance in experimental data should be reduced by using dedicated data analysis techniques like the multitaper method (see Figs. 2.4 and 2.5).

The simulations were done for data segments of equal duration (512 ms) and with a constant number (K=6) of tapers repeated over many time segments. This results in smoothing of the frequency spectrum by averaging over many signals.

In electrophysiological experiments the recording duration will vary in different experiments and will typically be much longer than 512 ms. Therefore, Fries et al. (2001b) used a different number of tapers for each recording signal, such that smoothing was done over the same frequency window (2W= constant) for all experimental data. Since the duration of their recordings was typically much longer than 512 ms, the longer duration gives more samples in the time domain, which results in a higher resolution in the frequency domain. This is illustrated in Fig. 2.5. Their result shows a higher resolution in the frequency domain but averaging over a smaller number of signals. Effectively the result is the same: the reduction of smoothing by the smaller number of signals is compensated by smoothing by the tapers over a larger number of samples in the frequency domain. However, note that the multitaper method with Slepian sequences as tapers is optimal among quadratic estimators because of the good concentration properties of Slepian sequences (see Percival and Walden, 2002). The lack of optimality of the Welch estimates means that it is a more biased estimate than the multitaper estimate with Slepian sequences, the variance and the frequency resolution being equal. The bias will grow as the size of the windows becomes smaller.

## Acknowledgement

We would like to thank Robert Desimone and John Reynolds for supporting the experimental recordings.

## Chapter 3

# Biased competition through variations in amplitude of $\gamma$-oscillations

Experiments in visual cortex have shown that the firing rate of a neuron in response to the simultaneous presentation of a preferred and non-preferred stimulus within the receptive field is intermediate between that for the two stimuli alone (stimulus competition). Attention directed to one of the stimuli drives the response towards the response induced by the attended stimulus alone (selective attention). This study shows that a simple feedforward model with fixed synaptic conductance values can reproduce these two phenomena using synchronisation in the gamma-frequency range to increase the effective synaptic gain for the responses to the attended stimulus. The performance of the model is robust to changes in the parameter values. The model predicts that the phase locking between presynaptic input and output spikes increases with attention.

---

Adapted from: Magteld Zeitler, Pascal Fries and Stan Gielen, *Journal of Computational Neuroscience* 25: 89-107 , 2008

## 3.1 Introduction

Our retinas are constantly stimulated by an overwhelming amount of information and the brain faces the task of reducing a potentially overloading amount of information into a manageable flow that reflects both the current needs of the organism and the external demands placed on it. In order to solve this problem, the brain uses a strategy to select the relevant information and to suppress information which is not relevant. The focus on and selection of relevant information is referred to as ”attention”. If just one single stimulus falls within the receptive field of a neuron, this stimulus can be attended or not, and in the latter case a stimulus outside the receptive field may be attended. Since higher cortical areas have large receptive fields (Desimone and Duncan, 1995), it is quite common that two (or even more) stimuli fall within the receptive field of a neuron. In that case one of them can be attended (selective attention) or none of them. In order to understand the neuronal substrate of attention, many single-unit studies in visual cortex have investigated how attended and unattended stimuli are encoded in the firing rate of neurons.

Neural correlates of attention have been studied using single-unit recordings in areas V1, V2, V4 and V5/MT in primate visual cortex. Several studies have shown that attention increases a neuron’s firing rate in response to a single stimulus in its receptive field (Treue and Maunsell, 1999; Luck et al., 1997; Reynolds et al., 1999; McAdam and Maunsell, 1999; Fries et al., 2001b). When two stimuli are presented in the receptive field of the neuron, the firing rate lies between the firing rates elicited by each of the stimuli presented alone (Moran and Desimone, 1985; Treue and Maunsell, 1996, 1999; Luck et al., 1997; Chelazzi et al., 1998, 2001; Reynolds et al., 1999; Reynolds and Desimone, 2003). This phenomenon is called stimulus competition, since populations of input neurons, encoding different stimuli, are thought to compete with one another to generate neuronal responses intermediate between the responses to the individual stimuli. When attention is directed to the neuron’s preferred stimulus, the neuron’s firing rate increases, whereas attention to the non-preferred stimulus decreases the firing rate (Chelazzi et al., 1998; Reynolds et al., 1999).

Several models have been proposed to reproduce these experimental observations regarding stimulus competition and selective attention. Reynolds et al. (1999) could explain their experimental results by assuming that the synaptic weights of an input representing one of the two stimuli increase five-fold when attention is directed towards that stimulus. However, it is not clear how synaptic efficacies could change five-fold at the time scale of attentional shifts.

Most approaches to come up with an explanation for stimulus competition and selective attention have focused on the effects of attention on the firing rate of neurons (see e.g. Tiesinga, 2005; Deco and Rolls, 2005; Buia and Tiesinga, 2006; Mishra et al., 2006). In addition to firing rate, several studies have provided convincing evidence that selective attention also increases rhythmic synchronisation among selected neuronal signals (Kreiter and Singer, 1996; Fries et al., 2001b; Schoffelen et al., 2005; Taylor et al., 2005; Womelsdorf et al., 2006). Several groups have published a model for neural implementation of attentional processes that attributes a possible role to the neuronal oscillatory activity in stimulus competition and/or selective attention (Tiesinga, 2005; Buia and Tiesinga, 2006; Mishra et al., 2006). Mishra et al. (2006) used gamma range correlations in the feedforward inhibitory inputs to the V4 neuron which are out of phase with the gamma band correlations within the excitatory input corresponding to the attended stimulus. Tiesinga (2005) used two asynchronous excitatory input populations and two stimulus-driven inhibitory input populations, which send 40 Hz spike volleys with some temporal dispersion to a V4 model neuron. In that study attention is modelled by changing the temporal dispersion or the relative phase between the volleys coming from the two inhibitory populations. Tiesinga (2005) used the crosscorrelation function as a measure for the synchronisation between the responses of two V4 neurons. Since he did this only for the condition that two stimuli are presented in the same receptive field, it is difficult to compare the result with the experimental results of one stimulus within and one outside the receptive field of a neuron as measured by Fries et al. (2001b). Another measure for the synchronisation between two signals is the coherence function. We will use the coherence function as a measure in the frequency domain for the synchronisation between the input and output of the excitatory neuron in our model for different conditions.

Since it is well known that the excitatory input in visual cortex from V1 to V2 and from V2 to V4 contains gamma frequency oscillations (Eckhorn et al., 1993; Frien et al., 1994; Maldonado et al., 2000), we have explored the possible role of gamma frequency oscillatory input in stimulus competition and selective attention. We tried to reproduce the experimental observations by a simple feedforward model. Therefore, the aim of the present study was to explore whether a simple feedforward model could explain the phenomenon of stimulus competition with a role for synchronous modulation of stimulus-related activity to implement the attentional bias. Our results show that a feedforward model, very similar to the gain modulation model of Reynolds et al. (1999) but with fixed synaptic weights, can explain stimulus competition. Assuming that attention is implemented by increased synchronisation of multi-unit spike activity, the model can reproduce the results by

Chelazzi et al. (1998) and Reynolds et al. (1999) on stimulus competition and selective attention. Although this model has a feedforward architecture, the underlying mechanism for changes in attention-related modulations of synchronous activity is not specified, this requires a role for some top-down feedback mechanism capable of enhancing synchrony.

## 3.2 Methods and Theory

We will start this section with a description of our model and the input signals to the model. In the second part of this section we will describe the methods to calculate the coherence, the phase coherence and the phase locking value between synaptic input and spike output.

### 3.2.1 Model

Fig. 3.1 shows the feedforward network, that we propose to explain stimulus-competition and selective attention. The output neuron $Y$ receives excitatory spike-trains from two populations ($X1$ and $X2$) with 80 Poisson neurons each and also receives inhibitory input from a population of 40 inhibitory neurons, for brevity called interneurons, I. In this study $X1$ and $X2$ represent the population of neurons encoding the preferred and non-preferred stimulus, respectively. With two populations of 80 excitatory neurons and a population of 40 inhibitory neurons projecting to the output neuron, the ratio of excitatory versus inhibitory synapses is 80% vs. 20% in agreement with experimental observations (Beaulieu et al., 1992). The two excitatory populations of neurons also project to the interneuron population. There is a small time delay $\tau_d$ of 2 ms between the spike times of the interneurons and the arrival times of these spikes at neuron $Y$. The interneurons and the output neuron $Y$ have been implemented in NEURON, as Hodgkin-Huxley type neurons (see below).

### 3.2.2 Stimulus-related input signals

The outputs from $X1$ and $X2$ are Poisson trains of spikes with a time-dependent rate $r^i(t)$:

$$r^i(t) \quad = \quad r + A^i_m \eta^i(t) \tag{3.1}$$

with $i \in \{1,2\}$, $r$ the constant rate, $\eta^i$ bandpass filtered Gaussian white noise with 3 dB points at 45 and 55 Hz, a quality factor Q of 5, zero mean and a variance of one, and with $A^i_m$ the modulation amplitude of the Gaussian white noise (GWN)

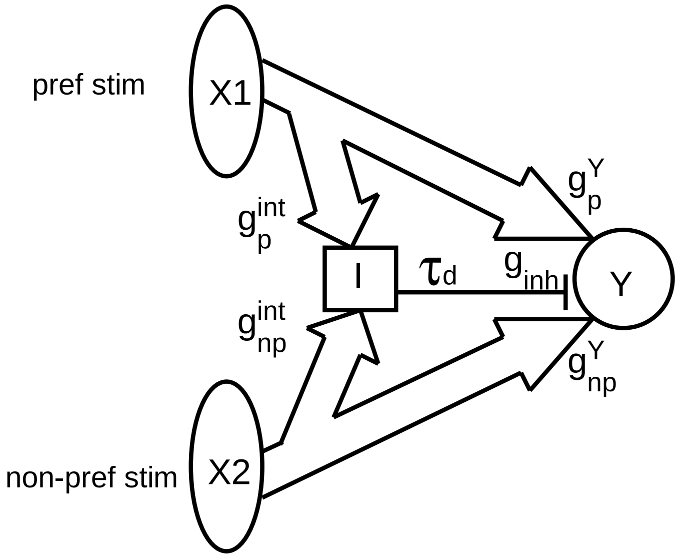

Figure 3.1: Schematic overview of the simple feedforward model. A preferred and a non-preferred stimulus are represented by spike trains, coming from two populations ($X1$ and $X2$) of 80 Poisson model neurons, each. These two populations project to a population of 40 Hodgkin-Huxley type interneurons ($I$) and to the Hodgkin-Huxley type output neuron $Y$. Each population receives its own time-dependent rate defined in Eqn. 3.1. Therefore, the spike trains within a population are correlated with each other, but not with spike trains in the other population. The two population activities are statistically the same as long as they are both unattended or both attended. The difference between responses to preferred and non-preferred stimulus is determined by the different synaptic conductances. Population $X2$ (non-preferred stimulus) has stronger projections to the interneurons $I$ and weaker to the output neuron $Y$ than population $X1$ (preferred stimulus) ($g_{np}^{int} > g_p^{int}$ and $g_{np}^Y < g_p^Y$ ). Spikes, generated by the interneurons arrive after a short delay $\tau_d$ of 2 ms at neuron $Y$. In addition both HH-like neurons ($I$ and $Y$) receive background noise, represented by conductance injections in the soma.

for population $i$. When the modulation amplitudes $A_m^i$ are the same for the non-preferred and the preferred stimulus, the spike trains encoding the non-preferred and the preferred stimulus are statistically identical. The different responses of the output neuron to the two stimulus inputs are due to the differences in synaptic conductances of the projections of the two populations of Poisson neurons to the inhibitory neurons and output neuron (will be explained later). Since we are not aware of any hard physiological data about these synaptic conductances in the literature, the different projections of the preferred and non-preferred stimulus to the interneurons and to the output neuron are an assumption of the model.

Several studies have shown that attention to a visual stimulus results in increased coherence between the local field potential and the activity of neurons, especially in the $\gamma$-band range (Fries et al., 2001b; Womelsdorf et al., 2006). In the visual system $\gamma$-band oscillations have been reported at frequencies in the range 40-80 Hz. Based on these findings we postulate that selective attention to a sensory stimulus is implemented as an increased amplitude $A_m$ for the neuronal activity encoding that stimulus. For the simulations of the responses of the output neuron $Y$ to various input signals we used a time duration $T$ of 8 092 s and time step $dt$ of 0.1 ms. The spike trains of the two Poisson populations $X_1$ and $X_2$ were modulated by a constant mean rate $r$=20 and with a modulation amplitude $A_m = 6$ for a non-attended stimulus and $A_m = 8$ for an attended stimulus (see Eqn. 3.1). If no input is presented to $X_1$ or $X_2$, $r = 3$ and $A_m = 0$. In order to explore the role of the modulation amplitude on the results of this study, some simulations used a modulation amplitude of 12 and 16 for the unattended and attended stimulus, respectively.

### 3.2.3 Geometry and properties of the HH-type interneurons and output neuron

The interneurons and output neuron $Y$ were implemented in the NEURON simulation environment (Hines and Carnevale, 1997) as single-compartment Hodgkin-Huxley type neurons with an area of 34 636 $\mu\text{m}^2$, in agreement with Destexhe et al. (2001). The inhibitory interneurons contain two sets of 80 synapses, the output neuron $Y$ has 40 inhibitory and two sets of 80 excitatory synapses. The synaptic conductivity $g$ is modelled by the default alpha function in NEURON. In this study most results were obtained for modulation amplitude $A_m$ values of 6 or 8. In that case the excitatory synapses from the populations $X_1$ and $X_2$ onto the interneurons have a maximum conductance of $g_{np}^{int} = 0.84$ nS and $g_p^{int} = 0.55$ nS for the non-preferred and preferred stimulus input, respectively and a time constant $\tau_e = 2$ ms. For the excitatory synapses onto the output neuron $Y$, the following values are taken: $g_{np}^{Y} = 1.52$ nS, $g_p^{Y} = 1.71$ nS, $\tau_e = 2$ ms. For the synapses from the inhibiting interneurons to the output neuron $Y$ we had $g_{inh} = 4.5$ nS and $\tau_i = 5$ ms. For modulation amplitudes $A_m$ with values of 12 ('no attention') and 16 ('with attention') the synaptic conductance values were $g_{np}^{int} = 0.84$ nS, $g_p^{int} = 0.55$ nS, $g_{np}^{Y} = 1.52$ nS, $g_p^{Y}$

= 1.71 nS and $g_{inh}$ = 3.8 nS. With these values for $A_m = 12$ the output neuron in our model generates, in agreement with experimental data of Reynolds et al. (1999), a firing rate ($f_p$) of about 20 sp/s in response to the 'preferred' stimulus condition and a firing rate ($f_{np}$) of about 10 sp/s in response to the 'non-preferred' stimulus.

The somata of the Hodgkin-Huxley type neurons have passive and active cell properties. The passive properties are the leak reversal potential (-80 mV), leak conductance (4.52 $10^{-5}$ S/cm$^2$) and membrane capacitance (1 $\mu$ F/cm$^2$). The active properties refer to the voltage-dependent $Na^+$ current and the "delayed-rectifier" $K^+$ current. The parameter values for the voltage-dependent $Na^+$ and $K^+$ currents were as described by Traub and Miles (1991) (see Appendix A).

The synaptic background activity of the Hodgkin-Huxley-like neurons (interneurons and output neuron) was approximated by conductance injections in the soma as described in Destexhe et al. (2001) (see Appendix A). In agreement with Destexhe et al. (2001), we used the following parameter values for the output neuron: the reversal potentials of the excitatory and inhibitory inputs $E_e$ = 0 mV, $E_i$ = -75 mV, the average conductances $g_{eo}$ = 12.1 nS, $g_{i0}$ = 57.3 nS and the time constants $\tau_e$ = 2.73 ms, $\tau_i$ = 10.49 ms. The standard deviations of the conductances corresponding to the background activity of output neuron $Y$ are given by $\sigma_e$ = 3.0 nS and $\sigma_i$ = 6.0 nS. For the interneurons the average conductances and the standard deviations of these conductances are 50% of the corresponding values of the output neuron.

In order to understand the responses of the interneurons, it is helpful to appreciate the relative size of the synaptic currents due to the background noise and due to stimulus related inputs. These synaptic currents due to the spike input are rough estimates, since the precise relation between spike input and synaptic current depends on the membrane potential of the neuron, and thereby also depends on other synaptic inputs that affect the membrane potential. Assuming that the mean membrane potential is near -55 mV (i.e. halfway between the membrane potential at rest near -75 mV and the threshold for firing) the mean current due to background activity for the interneurons is about 60% of the total excitatory input current. The remaining 40% comes from the mean excitatory input related to the preferred stimulus (16%) and to the non-preferred stimulus (24%). For the output neuron, the inhibitory stimulus related input is about 20% of the current due to the background activity, whereas the excitatory stimulus related input is about 85% of the background current. More details on these relative contributions and their effect on the relation between mean input current and firing rate is provided in Appendix B.

### 3.2.4 Coherence estimate

One of the predictions that flows from our hypothesis (see section 3.1) is that the output spike train is more coherent to the "attended" input spike train than to the

”ignored” input spike train. To quantify this, we will use the coherence function, in addition to firing rate to investigate the effect of attention on the spike output of neuron $Y$. In order to distinguish between the effect of the non-preferred and the preferred stimulus on the spike output, the non-preferred and preferred stimulus are statistically uncorrelated ($<\eta_i^{(t)}\eta_j^{(t)}>=\delta_{ij}$). This is in agreement with Gray et al. (1989) and Kreiter and Singer (1996) who reported that correlations between neuron population activities encoding different stimuli are absent.

The coherence function $\gamma(\omega)$ reflects how much of the variations in the output $y$ can be attributed to a linear filtering of the input signal $x$. The coherence function $\gamma(\omega)$ is defined by:

$$\mid \gamma(\omega) \mid = \frac{\mid C_{xy}(\omega) \mid}{\sqrt{\mid C_{xx}(\omega) \mid}\sqrt{\mid C_{yy}(\omega) \mid}} \tag{3.2}$$

with $C_{xy}(\omega)$ the Fourier transform of the cross covariance function (Marmarelis and Marmarelis, 1978). The coherence takes values in the range between 0 (input and output are uncorrelated) and 1 (the output is equal to the input after convolution by a linear system). Since the neuron itself is not a linear system, the coherence between the bandpass filtered Gaussian white noise input of one of the two Poisson populations and the spike output of neuron $Y$ will not reach the upper limit of one.

To estimate the coherence and its variance, we used the multi-taper method (Thomson, 1982; Mitra and Pesaran, 1987). The key idea behind the multi-taper method is that a physiological signal does not have discontinuities in the frequency spectrum and that the variance in the estimate of a signal can be reduced by smoothing in the frequency domain. The multi-taper method minimises bias and variance of the estimate by using multiple orthonormal data tapers. We have used sine-tapers as described in Zeitler et al. (2006) with length $N$ = 1.024 s and bandwidth $W$ = 2.9 Hz. Since the number of tapers to be used is $K = 2NW - 1$ tapers, the values for $N$ and $W$ used in this study gave $K$ = 5. The binwidth in the frequency domain is the Rayleigh frequency $f_r = 1/T = 1/(\mathrm{nfft}/f_s) = 0.98$ Hz, with sampling frequency $f_s$ (1000 Hz) and where nfft (1024) is the number of data points in the FFT . The input and output signals were both segmented in $T/N$ non-overlapping time segments of 1024 ms, with $T$ the duration of the simulation.

### 3.2.5 Phase locking

A high value of the regular coherence (Eq. 3.2) implies a strong relation between both amplitude and phase of input and output. Previous studies have shown that pairs of neuronal responses can undergo variations in relative amplitude even in the presence of tight phase coupling (Tass et al., 1998; Lachaux et al., 1999). For

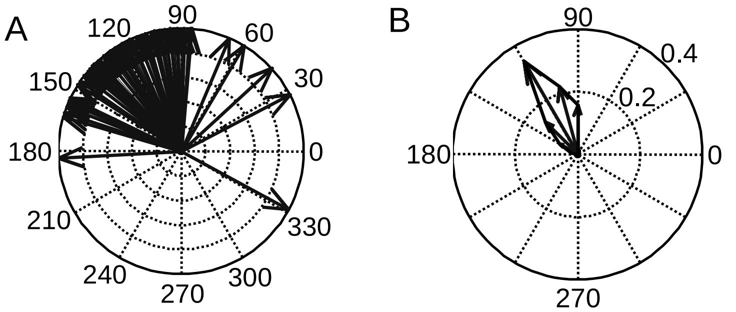

Figure 3.2: Illustration of phase-coherence analysis between stimulus and response. (A) shows a polar plot of the phase differences for 150 pairs of stimulus and response. In this example, the stimulus and its response have a preferred phase difference in the range between 90 and 150 degrees. (B) shows data in (A) in a polar plot. The length of the arrows show the fraction of phase differences falling in the corresponding phase bin.

this reason, the phase coherence has been introduced, which only considers the variability in relative phase between two signals $s_1$ and $s_2$. In this study, the phase coherence is calculated by segmentation of the two signals $s_1(t)$ and $s_2(t)$, both segmented in $T/N$ non-overlapping time segments of 1024 ms. Each segment of the signal $s_1$ and the corresponding segment of the second signal $s_2$ form a pair. The phase difference $\Delta\varphi(f)$ at frequency $f$ for each pair is given by:

$$\exp(i\Delta\varphi(f)) = \frac{S_1(f)S_2^*(f)}{|S_1(f)S_2(f)|} \tag{3.3}$$

where $S_i(f)$ is the Fourier transform of $s_i(t)$ and $^*$ refers to complex conjugate.

Fig. 3.2A shows a typical polar plot of the phase differences between 150 stimulus-response pairs for the neuron model in Fig. 3.1. The full range of 360 degrees was subdivided into 24 bins of 15 degrees $[15(j-1), 15j]$ for $j \in \{1, .., 24\}$. The number of phase differences falling into a bin, divided by the total number of phase differences in the unit circle, is the fraction of stimulus-response pairs with a phase difference in that bin. For each of the twenty bins, this fraction is represented by the length of the arrow, drawn in the middle of each bin (see Fig. 3.2B). All fractions are connected by a line. When stimulus and response are not phase locked at all, the phase differences will be distributed uniformly over 360 degrees. Complete phase locking with phase difference $\Phi$ corresponds to an arrow of unit length pointing in the direction $\Phi$.

Lachaux et al. (1999) introduced a method to quantify the degree of phase-locking between two signals. The phase locking value ($PLV$) between the two periodically repeated signals measures the inter-trial variability of the phase difference between these two signals. In our simulations, we average the phase relation over all stimulus-response pairs of the $M = T/N$ time segments:

$$PLV(f) = |\frac{1}{M}\sum_{m=1}^{M} exp(i\,\Delta\varphi_m(f))| \tag{3.4}$$

This phase locking value measures the average variability of the phase difference and takes values between 0 (complete lack of phase-locking) and 1 (completely phased locked).

The phase locking value is a function of frequency. In order to reduce the variance of the phase locking value, we used the multi-taper method, with $K = 5$ sine-tapers to reduce the variance of the spectra $S1(f)$ and $S2(f)$ in Eqn. 3.3. Since the phase locking value was very similar for all frequencies near 50 Hz, we determined the phase locking value for $f$ = 50 Hz as this gave the best signal-to-noise ratio for the 50 Hz bandpass filtered Gaussian white noise input.

## 3.3 Results

In this section the simulation results will be described for the firing rate of the output neuron $Y$ (section 3.3.2) and the coherences between the spikes of the output neuron and each of the stimulus-related inputs to the populations of Poisson neurons (section 3.3.3). We will conclude this section with the phase locking results.

### 3.3.1 Input-output relation of an interneuron

The interneuron plays a crucial role to explain stimulus competition (Fig. 3.3). If an interneuron receives input of the preferred stimulus with firing rate $f_{in}$ (this implies that all 80 neurons encoding the preferred stimulus have a constant firing rate of $f_{in}$ and the 80 neurons encoding the (absent) non-preferred stimulus have a firing rate of 3 spikes/s) the interneuron starts to respond at relatively high input firing rates (dashed line). Since the synaptic projections to the interneuron of the neural activity encoding the non-preferred stimulus are stronger than for the neural activity related to the preferred stimulus, the relation shifts to the left for the non-preferred stimulus only ( solid line, lower threshold for firing). The inset shows the population activity

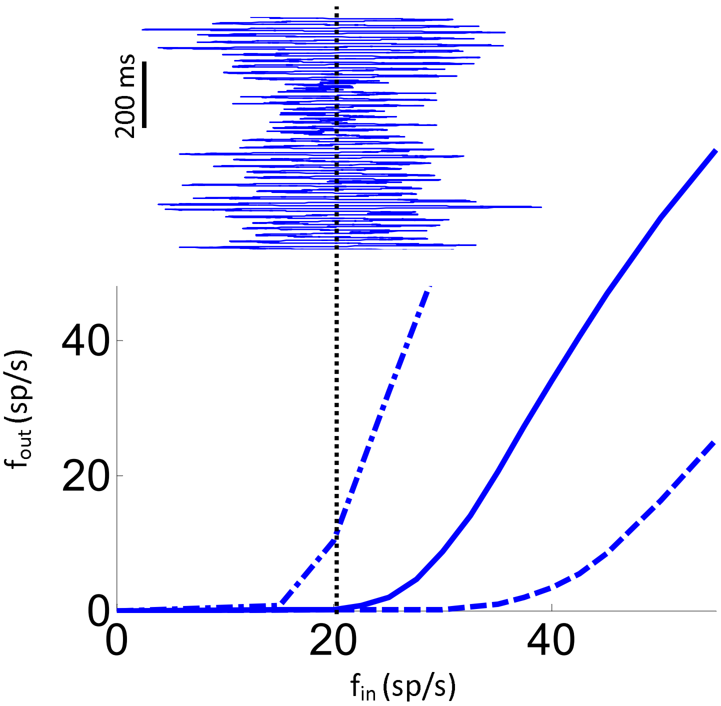

Figure 3.3: Relation between constant firing rate of neural activity representing the non-preferred and preferred stimulus and firing rate at the output of one interneuron for ”non-preferred stimulus only” (solid line), ”preferred stimulus only” (dashed line) and for ”both stimuli” (dashed-dotted line). For the condition ”non-preferred stimulus only” (solid line), the input to the interneuron has two components. One component represents the non-preferred stimulus by 80 Poisson spike series, each with a constant firing rate $f_{in}$. The other component represents the activity of 3 spikes/s in the population encoding the absence of the preferred stimulus. The dashed line shows the output of the interneuron for the preferred stimulus only. The dashed-dotted line shows the output of the interneuron to both stimuli, each represented by 80 Poisson spike series with a constant firing rate $f_{in}$. The inset shows the population activity of GWN-modulated Poison spike series, according to Eq. 3.1 with $A_m$=6.

of the Gaussian white noise (GWN) modulated Poisson spike input. This explains why the mean firing rate of the interneuron increases with increasing amplitude of the GWN-modulated Poisson spike input. For the output neuron qualitatively similar relations hold for the excitatory stimulus-related input, except for the fact that the output neuron responds better to the preferred stimulus alone, than to the non-preferred stimulus alone (solid and dashed lines interchanged).

### 3.3.2 Simulation results for the firing rate

Fig. 3.4 shows the firing rate of the output neuron for various stimulus conditions. The upper panel (A) shows the results for small modulation amplitudes ($A_m = 6$ and 8), the lower panel (B) for larger modulation amplitudes ($A_m = 12$ and 16). The results at the left part of the figure show the results for the 'no attention' condition, the right part of the figure the results for the stimulus conditions with one stimulus attended. We will first discuss Fig. 3.4A.

As explained in section 3.2, the statistical properties of the spike series, representing the non-preferred and preferred stimulus with no attention, are identical. The different effectiveness of the non-preferred and preferred stimulus is mainly due to the different conductance of the excitatory synapses from $X_1$ and $X_2$ to the output neuron. Since $g_p^Y$ (1.71 nS) $>$ $g_{np}^Y$ (1.52 nS) the direct excitatory projections of the population representing the preferred stimulus to the output neuron induce more action potentials in the output neuron than that of the population of neurons representing the non-preferred stimulus.

The population activities representing the preferred ($X_1$) and non-preferred stimulus ($X_2$) also reach the output neuron via the interneurons. In case only one stimulus is offered, the interneurons have a low firing rate. This is shown in Figure 3.5. For each stimulus separately, the induced firing rate of the interneurons is increasing as a function of the modulation amplitude $A_m$. However, the firing rates in response to the preferred and non-preferred stimulus are rather small (range between 0 and 0.03 sp/s and between 0 and 1.99 sp/s for the preferred and non-preferred stimulus, respectively). Therefore, it is mainly the larger conductance of the excitatory synapses from population $X_1$ to $Y$ which explains the higher firing rate of the output neuron to the activity of population $X_1$ ($f_p = 14.15$ sp/s, SD = 0.05 sp/s) than to the population activity $X_2$ ($f_{np} = 8.09$ sp/s, SD = 0.04 sp/s), see left side of Fig. 3.4A.

If the two neuronal populations, representing the activity of the preferred and non-preferred stimulus, would project to the output neuron only via excitatory synapses, one would expect a summation of firing rates when the preferred and non-preferred stimulus are presented simultaneously. However, we find stimulus competition in the responses of the output neuron, which is in agreement with experimental single-unit recordings (Reynolds et al., 1999), which most likely reflect the activity of excitatory neurons by their greater number and larger extracellular spikes. The interneurons play a crucial role in stimulus competition. This is

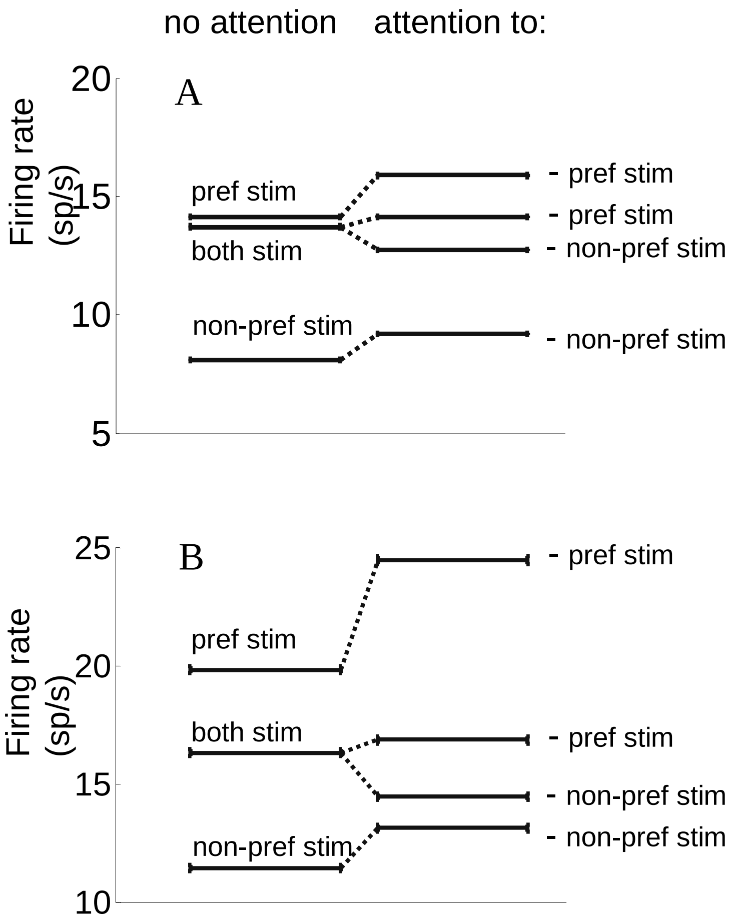

Figure 3.4: Mean firing rates of neuron $Y$ for different stimulus combinations for the 'with attention' and 'no attention' condition. (A) shows the results for small modulation amplitudes $A_m$ (see text), (B) for two times larger modulation amplitudes. The left side shows the results for the 'no attention', the right for the 'with attention' condition. The firing rate for responses to the preferred stimulus and non-preferred stimulus increases when the preferred or non-preferred stimulus is attended. The firing rate for responses to both stimuli (middle line on the left side) is not the summation of the firing rates for each of the stimuli alone, but is in between. The right side shows that if both stimuli are presented, attention to the preferred stimulus increases the firing rate (second line from the top) and decreases the firing rate when non-preferred stimulus is attended (second line from the bottom of the right side). The following maximum conductance values are used for the simulations to obtain the firing rate results as shown in (A) and (B): $g_{np}^{int}$ = 0.84 nS, $g_{p}^{int}$ = 0.55 nS, $g_{np}^{Y}$ = 1.52 nS, $g_{p}^{Y}$ = 1.71 nS and $g_{inh}$ = 4.50 nS for(A) and $g_{inh}$ = 3.8 nS for (B).

illustrated in Fig. 3.5, which shows the response of an interneuron for the three conditions: 'non-preferred stimulus only', 'preferred stimulus only' and 'preferred and non-preferred stimulus simultaneously' as a function of the modulation amplitudes $A_m$ of each stimulus. For all three conditions the response increases as a function of increasing $A_m$ which shows that the interneurons are sensitive to correlated input. As mentioned before, the firing rate of the interneuron is very small when only one stimulus is presented. Therefore, the inhibition is small. When two stimuli are presented simultaneously the firing rate of the interneurons increases more than linearly due to the sigmoidal relation between synaptic input and firing rate of neurons in general. For the preferred and non-preferred stimulus alone the interneurons operate at the bottom of the sigmoidal relation, whereas the combined input of the preferred and non-preferred input shifts the firing rate to the steep phase of the sigmoidal relation, see also Fig. 3.11 in Appendix B. So stimulus competition is caused by the activity of inhibitory interneurons, which generate a much higher firing rate when two stimuli are presented simultaneously compared to the condition that only one stimulus is presented. This higher response causes more inhibition for the target neuron and thus explains why the firing rate of the output neuron to both stimuli ($f_{both}$ = 13.72 sp/s, SD = 0.05 sp/s) falls between the firing rates to the preferred and the non-preferred stimulus presented alone.

In summary, the responses to the preferred and non-preferred stimulus alone are mainly due to excitatory inputs and the difference in firing rates ($f_{np} < f_p$) is caused by the different synaptic conductances. Competition ($f_{np} < f_{both} < f_p$) is the net effect of the two direct excitatory inputs plus the inhibition via the interneurons, which are mainly actively if both stimuli are offered simultaneously.

Based on experimental observations that have revealed larger amplitudes of $\gamma$-range activity during attention (Fries et al., 2001b; Womelsdorf et al., 2006; Taylor et al., 2005), attention to the preferred or non-preferred stimulus is implemented by a larger amplitude $A_m$ of the band-pass filtered noise to the Poisson neurons. Increasing $A_m$ leads to more spikes in the bursts of the population activity. Since the interneurons and output neuron receive a background synaptic input, they are sensitive to synchronous input (Martinez, 2006; Higley and Contreras, 2005). This explains the higher firing rate of the output neuron to the preferred ($f_p^{att}$ = 15.88 sp/s, SD = 0.05 sp/s) and non-preferred ($f_{np}^{att}$ = 9.18 sp/s, SD = 0.04 sp/s) stimulus with attention, relative to the 'no attention' condition (see right sight of Fig. 3.4A, which shows the responses to the attended stimuli).

A larger modulation depth causes larger excitatory spike volleys in the populations of Poisson neurons and results in higher firing rates of the 41 HH-like neurons. Since the larger modulation depth impacts also the interneurons, this in-

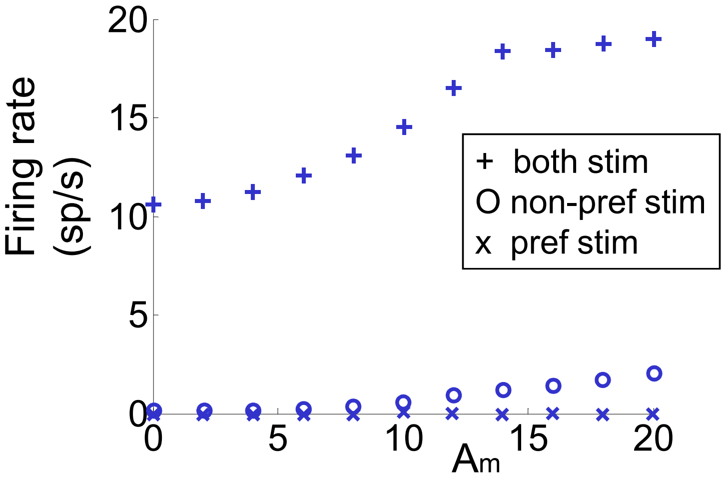

Figure 3.5: Input-output relationship of one interneuron. The response of an interneuron (firing rate in spikes/s) is shown as a function of the modulation amplitude $A_m$ for the stimulus condition with the preferred (x) and non-preferred (o) stimuli only, and for the condition with the preferred and non-preferred stimulus simultaneously (+). In the latter condition, the modulation amplitude was the same for both stimuli.

creased modulation can increase or even decrease the firing rate of the output neuron depending on the net balance between excitatory and inhibitory input. When both stimuli are presented simultaneously and when the preferred stimulus is attended, the effect of the larger excitatory spike volleys encoding the attended preferred stimulus is larger than the effect of inhibition by the increased firing rate of the interneuron. Therefore, the resulting firing rate $f_{both}^{att.pref}$ = 14.14 sp/s, SD = 0.05 sp/s (second line from top at the right side of Fig. 3.4A) is slightly larger than that in the condition of 'no attention, both stimuli' ($f_{both}$ = 13.72 sp/s, SD = 0.05 sp/s). If the non-preferred stimulus is attended instead of the preferred stimulus, the effect of larger excitatory spike volleys is smaller than the effect of inhibition by the increased firing rate of the interneurons. Therefore, the resulting firing rate $f_{both}^{att.np}$ = 12.73 sp/s, SD = 0.05 sp/s (third line from top at the right side of Fig. 3.4A) is significantly lower than in the condition 'no attention, both stimuli'.

In summary, the attended stimulus, presented alone, gives higher firing rates than the unattended stimulus alone due to the increased number of spikes in the population volleys. If both stimuli are presented and one is attended, the firing rate of the output neuron changes towards the firing rate elicited by that stimulus alone ($f_{both}^{att.np} < f_{both} < f_{both}^{att.pref}$).

Fig. 3.4B shows that stimulus competition and the stimulus selection effect can also occur for other values of the modulation amplitude $A_m$.

Obviously, the performance of the model depends on the strength of the excitatory projections of the non-preferred and preferred stimulus ($g_{np}^{Y}$ and $g_{p}^{Y}$), on their projections to the interneurons ($g_{np}^{int}$ and $g_{p}^{int}$), and on the synaptic connection $g_{inh}$ of the interneurons to the output neuron. The results presented in Fig. 3.4A were obtained with a fixed set of parameter values. The results presented in Fig. 3.4B (with a modulation amplitude twice as large as in Fig. 3.4A) were obtained with the same parameter values except for $g_{inh}$ which was decreased to 3.8 nS. The increase in modulation amplitude gives rise to an increased excitatory drive to both the output neuron $Y$ and the inhibitory neuron. Since the output neuron is inhibited by the interneurons, the change in firing rate of the output neuron $Y$ related to the increased modulation amplitude depends on the relative amounts of background noise, excitatory input and the strength of inhibition by the interneurons. The new value for $g_{inh}$ of 3.8 nS brings the firing rate of the output neuron to both stimuli halfway between that for the preferred and non-preferred stimulus only. Without reduction of $g_{inh}$ the firing rate to both stimuli would have been strongly biased towards the firing rate for the non-preferred stimulus only.

| $A_m$ | 6 and | 8 | 12 and | 16 |
|---|---|---|---|---|
| firing rate (sp/s) | $< f_I >$ | $< f_Y >$ | $< f_I >$ | $< f_Y >$ |
| non-pref only | 0.28 | 8.09 | 0.90 | 11.43 |
| non-pref att | 0.36 | 9.18 | 1.87 | 13.12 |
| pref only | 0.002 | 14.15 | 0.01 | 19.81 |
| pref att | 0.002 | 15.88 | 0.03 | 24.45 |
| both, non-pref att | 12.85 | 12.73 | 19.38 | 14.47 |
| both | 12.08 | 13.72 | 16.52 | 16.31 |
| both, pref att | 12.36 | 14.14 | 18.04 | 16.86 |

Table 1: average responses of an interneuron and the output neuron $Y$.

In order to investigate to what extent the results in Fig. 3.4B depend on the particular choice of synaptic conductances, we have analysed the model for a range of values of the relevant five synaptic conductances, $g_{np}^{int}$, $g_{p}^{int}$, $g_{np}^{Y}$, $g_{p}^{Y}$ and $g_{inh}$. As it is difficult to visualise a five dimensional parameter space, we have varied the synaptic conductances of the non-preferred and preferred stimulus to the interneurons ($g_{np}^{int}$ and $g_{p}^{int}$), and tried to find the proper values for $g_{np}^{Y}$, $g_{p}^{Y}$ and $g_{inh}$ such, that the model reproduced the properties of stimulus competition and selective attention. In detail, we adjusted the values of $g^{Y}_{np}$, $g^{Y}_{p}$ and $g_{inh}$ for each pair of ($g^{int}_{np}$, $g^{int}_{p}$) values such that the model had the following properties:

1. the firing rate to the preferred and non-preferred stimulus alone should be in the range between 19.6 to 20.1 sp/s and 9.7 to 10.4 sp/s, respectively. As explained before this is implemented by the requirement that $g^{Y}_{p} > g^{Y}_{np}$;
2. the firing rate of the output neuron to the non-preferred and preferred stimulus presented together should be between the firing rates of the non-preferred and the preferred stimulus presented alone (stimulus competition);
3. attention should give higher firing rates than without attention, when the non-preferred or preferred stimulus is presented alone;
4. attention to either the non-preferred or preferred stimulus, presented simultaneously, changes the firing rate towards that for the attended non-preferred or preferred stimulus presented alone.

We found 1.45 nS $\leq g^{Y}_{np} \leq$ 1.52 nS, 1.70 nS $\leq g^{Y}_{p} \leq$ 1.74nS and 3.3 nS $\leq g_{inh} \leq$ 5.04 nS for the three values of the synaptic connections to the output neuron $Y$, which are not shown in figure 3.6A.

The fitted ellips in Fig. 3.6A shows the range of parameter values for $g^{int}_{np}$ and $g^{int}_{p}$ where the effects of competition and selective attention can be reproduced for $A_m = 12$ (no attention) and $A_m = 16$ (with attention). For the region with parameters left of the grey area, either the inhibition is too small to reproduce the effect of stimulus competition or the inhibition is too strong, such that attention to the preferred stimulus does not increase but decrease the firing rate of the output neuron $Y$. For the region with parameters at the lower right of the grey area the model fails on a third aspect: attention to the non-preferred stimulus only decreases rather than increases the firing rate of the output neuron. Outside the upper boundary either the condition $f^{att.np}_{both} < f_{both}$ or $f_{np} < f_{both}$ is violated.

Fig. 3.6A shows that stimulus competition and selective attention occur for different values of the pair ($g^{int}_{np}, g^{int}_{p}$). Variations in the parameter values $g^{int}_{np}$ and $g^{int}_{p}$ cause changes in firing rates of the interneurons. The fitted line in Fig. 3.6B shows the firing rate $f_Y$ of the output neuron in the 'no attention, both stimuli' condition as a function of the firing rate $f_I$ of the interneurons. The firing rate of the output neuron, when both the preferred and the non-preferred stimulus are presented falls between the firing rates of the preferred stimulus alone (20 sp/s) and of the non-preferred stimulus alone (10 sp/s). This firing rate is high (small) for low (high)

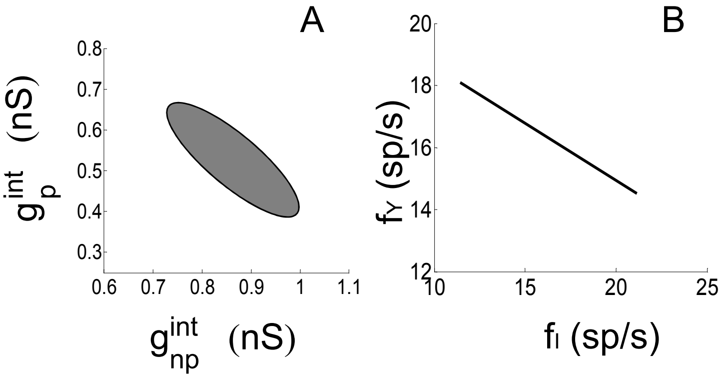

Figure 3.6: (A) Range of parameter values for $g_{np}^{int}$ and $g_{p}^{int}$ where the effects of attention, competition and selective attention can be reproduced. (B) Firing rates of the output neuron for the 'no attention, both stimuli' condition as a function of the corresponding average firing rate of the interneurons. Synaptic conductance values are chosen such that the effects of attention, competition and selective attention could be reproduced (grey area of (A)).

firing rates of the inhibitory neurons.

In summary, our results show that i) the competition and attention effects as shown in Fig. 3.4 occur for a range of synaptic conductance values; ii) the firing rate in the 'no attention, both stimuli' condition takes values between $f_{np}$ and $f_p$.

### 3.3.3 Simulation results for coherence estimate

Fig. 3.7 shows the coherence between the response of the output neuron and the time-dependent rate to populations $X_1$ and $X_2$ when either the non-preferred (upper row) or the preferred (lower row) stimulus is presented. The left and right column show the results for the 'no attention' ($A_m$=6) and 'with attention' ($A_m$=8) condition, respectively. Each of the panels shows a peak at 50 Hz, corresponding to the frequency content of the band-pass filtered stimuli.

Both for the non-preferred and preferred stimulus, the peak value of the coherence is larger for the 'with attention' condition (0.50 and 0.60, respectively) than for the 'no attention' condition (0.40 and 0.50, respectively). The 95% confidence level corresponds roughly to the range of the mean value, plus or minus 0.04. The larger coherence for the 'with attention' condition relative to the 'no attention'

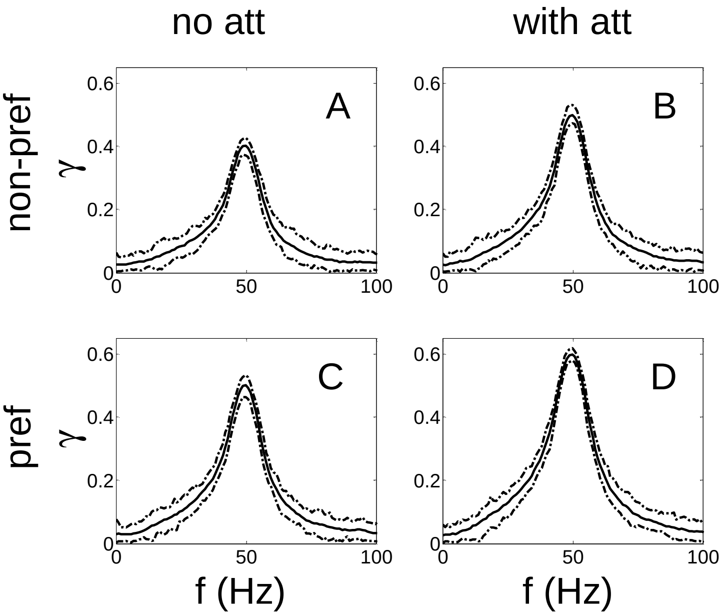

Figure 3.7: Coherence between the response and the modulation $A_m\eta(t)$ of the non-preferred (upper panels) and preferred (lower panels) stimulus for the 'no attention' (left panels) and 'with attention' (right panels) condition in case just one stimulus is presented. The dotted lines show the 95% confidence level. Attention increases the peak value of the coherence estimate. The peak values of the coherence between the response and the non-preferred stimulus modulation are smaller than for the preferred stimulus.

condition is due to the fact that larger spike volleys in the input will cause more precise spike timing (less variability). The peak values of the coherence for the non-preferred stimulus (Figs. 3.7A and B) are smaller than those for the preferred stimulus (Figs. 3.7C and D). This is caused by two facts: the preferred stimulus has stronger excitatory synapses to the output neuron than the non-preferred stimulus ($g_p^Y > g_{np}^Y$) and will therefore cause spikes which are more precisely time-locked to the stimulus. The second reason is that the stronger synaptic projections of the non-preferred stimulus to the interneurons cause more frequent inhibitory post-synaptic potentials in the output neuron, which can delay or even prevent the non-preferred stimulus to elicit a spike in the output neuron, resulting in a smaller coherence peak value.

Fig. 3.8 shows the coherence between the response of the output neuron and the input to population $X_2$ (non-preferred stimulus) (upper row) and to population $X_1$ (preferred stimulus) (lower row), respectively, when both stimuli are presented. The middle column (Figs. 3.8B and E) shows the results when both stimuli are presented simultaneously without attention ($A_m = 6$). For the non-preferred and preferred stimulus the coherence estimate has a peak value of 0.35 and 0.40, respectively. These two peak values are smaller than for the condition when these stimuli were presented alone (Figs. 3.7A, C). When the non-preferred and preferred stimulus are presented simultaneously, the spikes of the output neuron reflect the contribution of both stimuli. The effect of the non-preferred (preferred) stimulus on the spike responses acts as a noise term in the response to the preferred (non-preferred) stimulus, which explains the smaller coherence values in Fig. 3.8 compared to that in Fig. 3.7.

When the preferred or non-preferred stimulus is attended (Figs. 3.8F, A), this stimulus becomes more effective, causing a better locking of the spike response to that stimulus. This more precise locking of the neuron to the attended stimulus leads to a larger coherence value for the attended stimulus and a lower coherence for the non-attended stimulus (compare Figs. 3.8F and A with Figs. 3.8D and C, respectively). The larger coherence for the attended preferred stimulus (0.49 vs. 0.40) and for the attended non-preferred stimulus (0.43 vs. 0.35) is significant ($p < 0.001$). The tendency that the coherence for the non-attended stimulus decreases when the other stimulus is attended (0.37 vs. 0.40 for the preferred and 0.33 vs. 0.35 for the non-preferred stimulus) is significant ($p < 0.001$). The 95% confidence level of the values corresponds roughly to the range of the mean value, plus or minus 0.04.

The coherence results for modulation amplitudes, which are twice as large, are similar and therefore not shown.

In summary: by attending a stimulus, the peak value of the coherence between the attended input and the response is larger compared to the condition 'no attention'. The coherence between the non-attended input and the response does significantly decrease compared to the 'both stimuli' condition.

### 3.3.4 Phase locking results

Fig. 3.9 shows polar plots of the probability distributions of phase differences between stimulus and response. The solid line shows the results for the 'no attention', the dashed line for the 'with attention' condition. For the 'non-preferred stimulus only' condition Fig. 3.9A shows that there is clear phase locking between the stimulus and the response of the output neuron which increases with attention (dashed line). The narrower the ellipse, the better the signals are locked to a certain phase

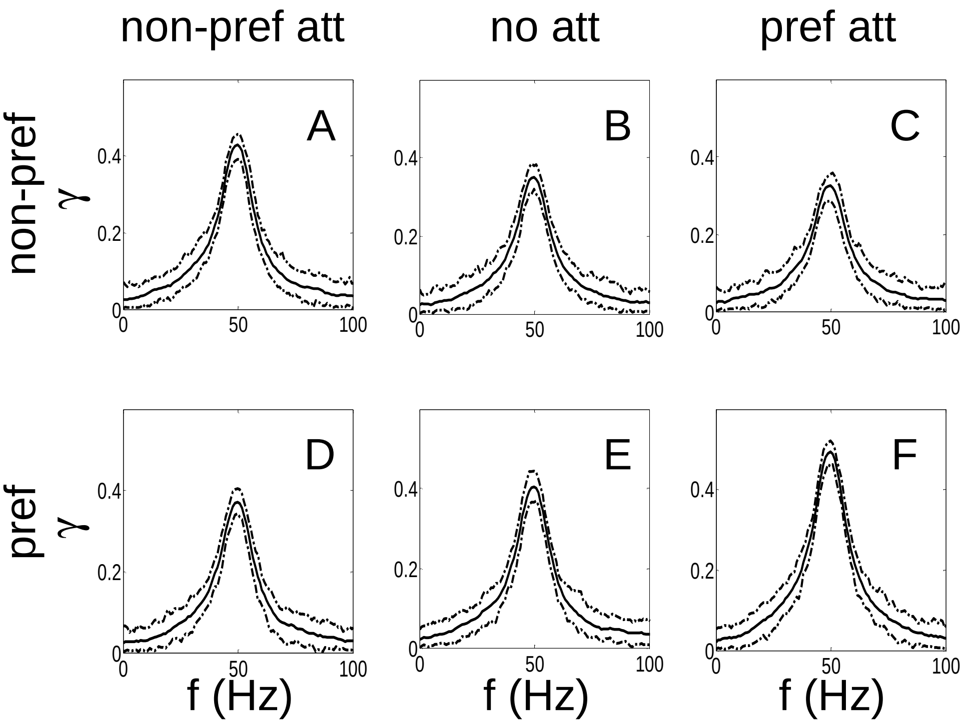

Figure 3.8: Coherence between the response and the modulation $A_m\eta(t)$ of the non-preferred (upper panels) and of the preferred (lower panels) stimulus for different attention conditions. The middle panels (B and E) show the results when both stimuli are presented simultaneously and unattended. The left panels (A and D) show the coherence when the non-preferred stimulus has been attended, the right panels (C and F) when the preferred stimulus is attended. The 95% confidence level is shown by the dotted lines. Attention to one of the two stimuli results in a significantly larger peak value for the coherence for the attended stimulus and a significantly smaller peak value for the other stimulus.

difference and the higher the phase locking value (PLV) will be. The increase of the PLV for the 'attention' condition is significant (0.69 ± 0.01 ('non-preferred stimulus only') versus 0.80 ± 0.01 ('attended non-preferred stimulus only'), $p < 0.001$), where phase locking values are given as the mean plus or minus the standard deviation. Fig. 3.9B shows similar results for the 'preferred stimulus only' condition (mean PLV 0.80 ± 0.01 and 0.88 ± 0.01, $p < 0.001$, for the 'non-attended preferred stimulus only' and 'attended preferred stimulus only' condition, respectively).

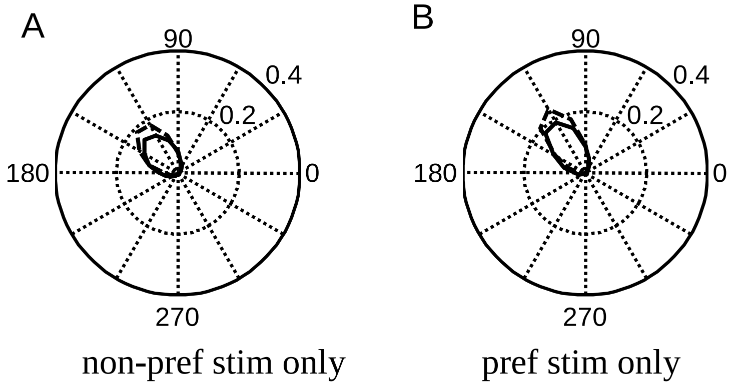

Figure 3.9: Polar plots of the fraction of phase differences between stimulus and response for the ’one stimulus only’ condition. The solid (dashed) line shows the polar plots for the ’no attention’ (’with attention’) condition. (A) shows the results for the ’non-preferred stimulus only’ condition. (B) shows the ratios for the ’preferred stimulus only’ condition. The response is better phase locked to the preferred (B) than to the non-preferred stimulus (A). (See text for further details).

Figs. 3.10A and B show the polar distribution of the phase relation between input and spike output, when the preferred and non-preferred stimulus are presented simultaneously. Fig. 3.10A (B) shows the phase relation between the output and the input to $X_2$ (non-preferred) and $X_1$ (preferred), respectively. The solid line shows the results for the condition ’no attention, both stimuli’, the dashed line for the condition ’with attention’. Both panels show that attention increases the phase locking between input and response. The phase locking values for the non-preferred (preferred) stimulus are significantly larger for the condition ’with attention’ ($0.73 \pm 0.01$, $0.79 \pm 0.01$, respectively, $p < 0.001$) than for the ’no attention, both stimuli’ ($0.63 \pm 0.01$, $0.70 \pm 0.01$, respectively, $p < 0.001$) condition. The mean PLV for the preferred (non-preferred) stimulus for the ’no attention, both stimuli’ condition, PLV = $0.70 \pm 0.01$ ($0.63 \pm 0.01$ ) is significantly different for the condition ’with attention to the other stimulus’, PLV = $0.64 \pm 0.01$ ($0.59 \pm 0.01$).

The phase locking value results for two times larger modulation amplitudes are similar and therefore not shown.

In our simulations, the results of the coherence function and phase locking values at 50 Hz are very similar: attention significantly increases the coherence and the phase locking value between the response and the attended stimulus.

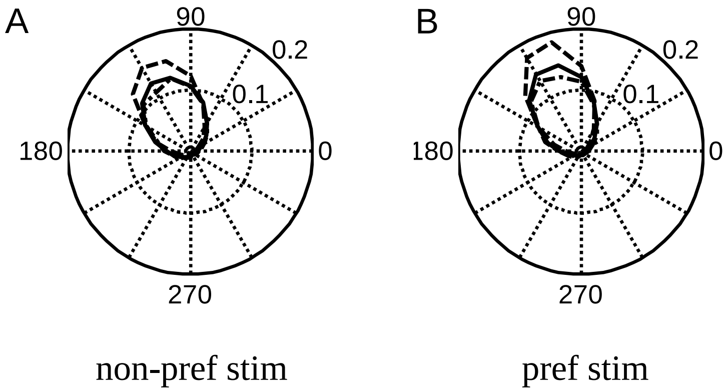

Figure 3.10: Polar plots for the fraction of phase differences between stimulus and response for the 'no attention, both stimuli' condition. (A) shows the results for the non-preferred stimulus. Attending the non-preferred stimulus (dashed line) increases the phase locking between the non-preferred stimulus and the response compared to the 'both stimuli with no attention'. Attending the preferred stimulus (dashed-dotted line) decreases the phase locking between the non-preferred stimulus and the response. (B) shows the results for the preferred stimulus. Attending the preferred stimulus (dashed line) increases the phase locking between the preferred stimulus and the response compared to the 'both stimuli with no attention'. Attending the non-preferred stimulus (dashed-dotted line) decreases the phase locking between the preferred stimulus and the response.

## 3.4 Discussion

Many experimental and modelling studies have focussed on the neuronal implementation of attention (Bushnell et al., 1981; Spitzer et al., 1988; Motter, 1993; McAdam and Maunsell, 1999; Treue and Trujillo, 1999; Fries et al., 2001b; Tiesinga, 2005) and on stimulus competition (Moran and Desimone, 1985; Desimone and Duncan, 1995; Reynolds et al., 1999; Treue and Trujillo, 1999; Tiesinga, 2005) at different levels of neuronal processing varying from brain areas (Corbetta and Shulman, 2002) to single neurons (Deco and Rolls, 2005; Tiesinga, 2005). Most of these studies have focussed on firing rate to encode attended and unattended stimuli. However, it is well known that rhythmic neuronal activity, such as in $\beta$- and $\gamma$-oscillations, plays an important role in encoding sensory stimuli (see e.g. Kreiter and Singer, 1996) and that attention affects the amplitude of the rhythmic neuronal oscillations. The latter is illustrated by the coherence between the local field potential and spike output, which provides a sensitive measure of local neuronal synchronisation. Fries et al. (2001b) found that for the 'with attention' condition, the coherence between the local field potential and the simultaneously recorded spike train was significantly larger with than without attention to the stimulus. Our results will be discussed in more detail below, starting with a comparison of the model responses with other models.

The architecture of our model is quite similar to the gain modulation model by Reynolds and coworkers (Reynolds et al., 1999). The main differences with respect to the gain modulation model are related to the nature of the neuronal input signals and to the neuronal implementation of attention. In the Reynolds model constant firing rates are used to encode the preferred and non-preferred stimuli and attention was implemented by a five-fold increase of the efficacy of the synapses that transmit the attended stimulus. This model left open the question of how synaptic efficacy can be modulated selectively for the attended stimulus input at such a short time scale. In agreement with experimental observations (Fries et al., 2001b), our working hypothesis was that attention is implemented through enhanced gamma activity, which makes this input more effective in eliciting a spike in the output neuron, and thus increases the effective strength of the signal encoding the attended stimulus.

Our model is an alternative for the model proposed by Tiesinga (2005) which postulates a stimulus-related excitatory input without rhythmic oscillations and with top-down input from the Frontal Eye Fields (FEF). The main difference between our model and that by Tiesinga (2005) is that we assume that attention is implemented in the $\gamma$-modulated stimulus-related neural input, whereas Tiesinga (2005) does not assume $\gamma$-modulated stimulus-related input. In the Tiesinga model the $\gamma$-oscillations are postulated to be induced by FEF input to the interneurons. Although it is well know that the FEF is involved in attention-related modulations of neuronal activity (Moore and Amstrong, 2003), it is still a matter of debate how the FEF input affects the neuronal processing. Our model allows a role for top-down attentional modulation of the amplitude of the $\gamma$-oscillations in the input population activity representing the visual stimulus. It is a topic for future research to investigate the details of attention-related top-down mechanisms.

One of the values of models is that they can provide possible explanations for experimentally observed phenomena. When developing a model, one should always try to explain as many experimental findings with as few as possible model assumptions. In our model, we assumed that the stimulus-related neuronal activity has rhythmic oscillatory components. This assumption is supported by experimental observations which have revealed stimulus-related rhythmic activity in V1 (van der Togt et al., 2006; Roelfsema et al., 2004; Rols et al., 2001), V2 (Frien et al., 1994) and V4 (Fries et al., 2001b; Taylor et al., 2005). Moreover, we assume that attention is implemented by increased amplitudes of the rhythmic excitatory activity. This is in agreement with experimental observations by Fries et al. (2001b); Taylor et al. (2005); Womelsdorf et al. (2006), who reported that attention is related to an increased coherence between local field potentials and single-unit activity. The simple feed-forward model reproduces experimental data of stimulus competition and attention effects on firing rate (see e.g. Reynolds et al. (1999)). Moreover, our model predicts an increased peak value of the coherence due to attention, emphasising the increased neuronal synchronisation by attention. Our predictions concerning an increased coherence for attended stimuli and a decreased coherence in case the other stimulus within the receptive field is attended, are in agreement with what is found by Smiyukha et al. (2006). These authors placed two small stimuli close to each other, causing two spatially well separated foci of gamma-band activity in area V1 of a macaque. The corresponding foci in V4 were largely overlapping. Wavelet based analysis of correlations revealed strong synchronisation of field potentials in the gamma-band between the site in V1, processing the attended shape, and the site in V4 responsive to both stimuli. Synchronisation with activity in V4 is weak for other sites in V1, processing non-attended stimuli. This strong synchronisation between the area in V1, which processes the attended stimulus, and the site in V4, is at least qualitatively similar to the increase in coherence between input and spike output in our model.

Recently, a model with an architecture very similar to our model was proposed by Mishra et al. (2006) to explain the phenomena of stimulus competition and selective attention. The neuronal mechanisms in their model to explain stimulus competition are feedforward inhibition, like in our model, and synaptic depression, which is effective for input frequencies of 40 Hz and above. Like in our model, each stimulus is represented by excitatory multi-unit activity. In their model the excitatory neuronal signals that encode the preferred and non-preferred stimuli are always in anti-phase. The phenomenon of selective attention in their model is achieved by imposing a phase shift of the response of the interneuron relative to the excitatory activity encoding the attended stimulus. This implies that the inhibition is more or less in anti-phase with the excitatory drive of the attended stimulus, but in phase with the excitatory drive of the unattended stimulus. Therefore, the excitatory input of the unattended stimulus is cancelled by inhibition from the interneuron. This works well when the excitatory drive and the inhibitory input from the interneurons is tuned at the same frequency (40 Hz in the paper by Mishra et al. (2006)) and more or less in anti-phase. However, experimental studies have found that rhythmic synchronisation is broadly tuned and that the neuronal activity representing two different stimuli is uncorrelated (Gray et al., 1989; Kreiter and Singer, 1996). Therefore, we decided to generate the neuronal signals for attended and unattended stimuli by band-pass filtering two independent noise signals.

Fries et al. (2001b) showed that the amplitude of the input fluctuations of neurons in V4 is larger when the stimulus is attended than when the same stimulus is not attended. Therefore, we increased the amplitude of our input modulation by 33% to implement the effect of attention (from $A_m = 6$ to 8). This increase in amplitude caused a 12% higher firing rate of the output neuron, a 20-25% increase in the coherence between input and output and a 10-16% larger phase locking value (PLV). We have also done the simulations for amplitudes of the input modulations, twice as large. Now, the 33% increase in amplitude of the input modulation, which implemented the effect of attention, caused a 15-25% higher firing rate of the output neuron, a 11% increase in the coherence between input and output and a 3% larger PLV. This indicates that all results for firing rate, coherence and phase coherence are qualitatively similar, independent of modulation amplitude, showing that our model is quite robust.

The results of this study were obtained for various modulation amplitudes of the stimulus-related input with the same set of parameters, except for the value of $g_{inh}$ which was reduced from 4.5 nS to 3.8 nS when the modulation amplitude was made twice as large. If we had kept the synaptic strength at 4.5 nS, the response of the output neuron to both stimuli would have been more biased towards the output for the non-preferred stimulus. As far as we know there have been no studies which have systematically investigated the effect of changes in modulation amplitude of excitatory drive to neurons in V2 and V4 on stimulus competition. Maybe a bias to the response to the non-preferred stimulus alone for larger modulation amplitudes is what will be observed. Another alternative might be that dynamic synapses (Tsodyks et al., 1998, 2000) reduce the effective synaptic strength of the projection of the inhibitory neurons to the output neuron when the increased modulation amplitude causes a larger increase of the firing rate of the inhibitory neurons. The latter seems a plausible mechanism which we saw as a justification to reduce the synaptic efficacy of the projections of the inhibitory neurons. The size of the reduction is certainly not critical to qualitatively reproduce the results in this study.

A similar robustness was found for variations in the synaptic strengths. As shown in Fig.3.6A stimulus competition could be reproduced over a range from 0.7 to 1.0 nS for $g_{np}^{int}$ and from 0.4 to 0.7 nS for $g_{p}^{int}$. Changes in the parameter values lead to variations in the firing rate of the output neuron (Fig.3.6B). For the condition 'no attention, both stimuli' this range goes from about 15 sp/s to 18 sp/s depending on the firing rates of the inhibitory neurons. This range of attenuation of the firing rate of the output neuron to both stimuli compared to the firing rate for the preferred stimulus alone, is within the range reported by Reynolds et al. (1999) and Gawne and Martin (2002) for V4, by Miller et al. (1993) for the inferior temporal cortex and by Rolls and Tovee (1995) in the anterior part of the superior temporal sulcus.

We want to remark that the effect of competition in the experimental results in the literature is not always as large as in the paper shown by Reynolds et al. (1999). See for example the study of Gawne and Martin (2002). For a substantial fraction of the neurons these authors found that the firing rate to both stimuli was close to the highest firing rate to the stimuli presented separately.

Lachaux et al. (1999) showed that the coherence cannot distinguish phase and amplitude covariance. As an alternative they introduced the PLV to detect phase synchrony. For our simulation results we determined the coherence values (typically 0.33 - 0.60) as well as the phase locking values (typically 0.59 - 0.88). These two sets of values lead to the same qualitative conclusions: (i) the input and response of the output neuron $Y$ are more synchronised if the stimulus, represented by the neuronal input, is attended compared to be not attended; (ii) the input representing the not-attended stimulus is less synchronised with the response of the output neuron $Y$ than the input which represents the simultaneously offered but attended stimulus. In addition, the polar plots of Figs. 3.9 and 3.10 show that the average phase difference between input and response of the output neuron $Y$ are different for the stimulus conditions 'non-preferred stimulus, only', 'preferred stimulus, only' and 'both stimuli'. The average phase difference for the 'preferred stimulus, only' condition ($< \varphi_p > \sim 125$ degree, Fig. 3.9B ) is smaller than for the 'non-preferred stimulus, only' condition ($< \varphi_{np} > \sim 133$ degree, Fig. 3.9A). This can be explained by the fact that the maximum conductance of the excitatory synapses to the output neuron is larger for the excitatory neuronal activity representing the preferred than for that representing the non-preferred stimulus. For the condition 'both stimuli, no attention' this average phase difference ($< \varphi_{both} > \sim 114$ degree, solid line in Fig. 3.10A and B) is even smaller since the neuron receives more input, so that it can generate even faster a spike (in case it is not inhibited!).

In this study we have presented a feedforward model which can reproduce neuronal responses in visual cortex related to stimulus competition and selective attention effect, by: i) using gamma-modulated population activities to represent the stimuli; ii) increasing the modulation depth of the population activity representing the attended stimulus; iii) determining the non-preferred and preferred stimulus response by using different values for each group of the various synaptical conductances of the interneuron and output neuron. The numerically obtained firing-rate results are similar to experimental results reported by Reynolds et al. (1999), Miller et al. (1993) and Rolls and Tovee (1995).

## Acknowledgements

We thank Michelle Lilith for fruitful discussions during and after the Advanced Course in Computational Neuroscience in Arcachon (France), where we started this project. This project was funded by the Netherlands Organisation for Scientific Research (NWO 051.02.050).

## APPENDIX A

The parameter values for the voltage-dependent $Na^+$ and $K^+$ currents were described by (Traub and Miles, 1991):

$$\begin{aligned}
I_{Na} &= \bar{g}_{Na} m^3 h (V - E_{Na}) && (3.5)\\
\frac{dm}{dt} &= \alpha_m(V)(1-m) - \beta_m(V)m && (3.6)\\
\frac{dh}{dt} &= \alpha_h(V)(1-h) - \beta_h(V)h && (3.7)\\
\alpha_m &= \frac{-0.32(V - V_T - 13)}{exp[-(V - V_T - 13)/4] - 1} && (3.8)\\
\beta_m &= \frac{0.28(V - V_T - 40)}{exp[(V - V_T - 40)/5] - 1} && (3.9)\\
\alpha_h &= 0.128 exp[-(V - V_T - V_S - 17)/18] && (3.10)\\
\beta_h &= \frac{4}{1 + exp[-(V - V_T - V_S - 40)/5]} && (3.11)
\end{aligned}$$

where $V_T$ = -58 mV and $V_S$ = -10 mV (Destexhe and Paré, 1999). $\bar{g}$ is the maximum conductance ($\bar{g}_{Na}$ = 361.2 $10^{-4}$ S/cm$^2$, $\bar{g}_{Kd}$ = 70 $10^{-4}$ S/cm$^2$), *m*, *h* and *n* are the time-varying gate variables, $E_{Na}$ = 50 mV is the sodium reversal potential, $E_{Kd}$ = -90 mV the potassium reversal potential, $\alpha$ is the forward and $\beta$ the backward rate. The "delayed-rectifier" $K^+$ current was described by:

$$\begin{aligned}
I_{Kd} &= \bar{g}_{Kd} n^4 (V - E_K) && (3.12)\\
\frac{dn}{dt} &= \alpha_n(V)(1-n) - \beta_n(V)n && (3.13)\\
\alpha_n &= \frac{-0.032(V - V_T - 15)}{exp[-(V - V_T - 15)/5] - 1} && (3.14)\\
\beta_n &= 0.5 exp[-(V - V_T - 10)/40] && (3.15)
\end{aligned}$$

In our model both the interneurons and the output neuron receive background synaptic input as received by cortical neurons *in vivo*, represented by fluctuating background conductance injections in the soma. These conductances are produced by an Ornstein-Uhlenbeck process, as described by Destexhe et al. (2001):

$$\frac{dg(t)}{dt} = \frac{g_0 - g(t)}{\tau} + \chi(t)\sqrt{\frac{\sigma^2}{\tau}} \tag{3.16}$$

where $g_0$ is the mean conductance, $\tau$ is the conductance time constant, $\sigma^2$ is the variance of the conductance and $\chi(t)$ is Gaussian white noise with zero mean and a standard deviation of 1. For the inhibitory background conductance of the output neuron we use $g_{i0}$ = 57.3 nS, $\tau_i$ = 10.49 ms and $\sigma_i$ = 6.0 nS with a reversal potential $E_i$ = -75 mV. For the excitatory background conductance of the output neuron we use $g_{e0}$ = 12.1 nS, $\tau_e$ = 2.73 ms and $\sigma_e$ = 3.0 nS with a reversal potential $E_e$ = 0 mV. For the interneurons the average conductances and the standard deviations of these conductances are 50% of the corresponding values of the output neuron.

For the implementation in NEURON of the passive and active properties and of the synaptic background we used parts of the code of example 5 of the NEURON tutorial from the Obidos 2004 course
($http://www.neuron.yale.edu/ftp/neuron/contrib/obidos\_tutorials/$).

## APPENDIX B

In this appendix we provide a rough estimate of the currents injected as a noisy background and the currents due to the stimulus related inputs to the conductance based neurons in out model. Current and conductance are related by:

$$I_{i,e}(t) = G_{i,e}(t)(V(t) - E_{i,e}) \tag{3.17}$$

where $G_{i,e}$ is the total conductance, $E_{i,e}$ the reversal potential and $V$ the membrane potential for the inhibitory (i) or excitatory (e) input. The total input current is the sum over all excitatory and inhibitory currents. The amount of current is time-dependent since it is a function of the fluctuating membrane potential and of the total amount of the conductance at time t. We will approximate the currents by taking time-averages for conductance and membrane potential. The mean value for the membrane potential $V$ depends on the contribution of all excitatory and inhibitory inputs. From the simulations in NEURON we know that the average membrane potential $< V >$ of the interneurons (output neuron $Y$) is about -55 mV (-60 mV, respectively), i.e., well between the rest membrane potential near -75 mV and the threshold for action potential generation. The value of the reversal potentials are $E_i$ = -75 mV and $E_e$ = 0 mV for both the interneuron and excitatory neuron, with these values the average currents caused by the noisy background in the interneurons is

$$\begin{aligned} I_i = & \quad g^I_{i0}(< V^I > - E_i) &= -0.6\,nA \\ I_e = & \quad g^I_{e0}(< V^I > - E_e) &= 0.3\,nA \end{aligned} \tag{3.18}$$

The average input currents caused by the stimuli in the interneurons is

$$\begin{aligned} I_i = & \quad N_i \ < f_I > \ g_{inh}\ \tau_i(< V^I > - E_i) &= -0\,nA \\ I_e = & \quad N_e \ < r > \ (g^{int}_p + g^{int}_{np})\tau_e(< V^I > - E_e) &= 0.2\,nA \end{aligned} \tag{3.19}$$

with $N_{i,e}$ the number of input spike trains, $< f_I >$ the average firing rate of the stimulus-related inhibitory input spike trains, $< r >$ the average rate of the stimulus-related excitatory Poisson spike trains and $\tau_{i,e}$ the rise time of the $\alpha$-synapses. This means that the inhibitory input current of the interneurons is only due to the noisy background and the excitatory current comes for 58% from the noisy background and 42% comes from the stimulus related input.

The average input currents caused by the noisy background in the output neuron are

$$\begin{aligned} I_i &= g_{i0}(< V^Y > -E_i) &= -0.9\ nA \\ I_e &= g_{e0}(< V^Y > -E_e) &= 0.7\ nA \end{aligned} \tag{3.20}$$

where $g_0$ is the mean conductance of the conductance injections in the soma as described in appendix A. The average input currents caused by the stimuli in output neuron $Y$ are

$$\begin{aligned} I_i &= N_i < f_I > g_{inh}\ \tau_i(< V^Y > -E_i) &= -0.2\ nA \\ I_e &= N_e < r > (g_p^Y + g_{np}^Y)\ \tau_e\ (< V^Y > -E_e) &= 0.6\ nA \end{aligned} \tag{3.21}$$

with $N_{i,e}$ the number of input spike trains, $< f_I >$ the averaged inhibitory input spike train, $< r >$ the averaged rate of the excitatory Poisson spike train, $\tau_{i,e}$ the rise time of the $\alpha$-synapses. The noisy background is responsible for 84 % of the total inhibitory input current and the stimulus related input contributes 16%. The excitatory current contributes for 54% of the noisy background and 46% is due to the stimulus related input.

The input current for the 'preferred stimulus only' condition (p) consist of the background current plus the excitatory related to the preferred stimulus. For the 'non-preferred stimulus only' condition (np) the excitatory stimulus-related current to the inhibitory neuron is larger than the current for the preferred stimulus because of the larger value of the synaptic connections for the non-preferred stimulus input.

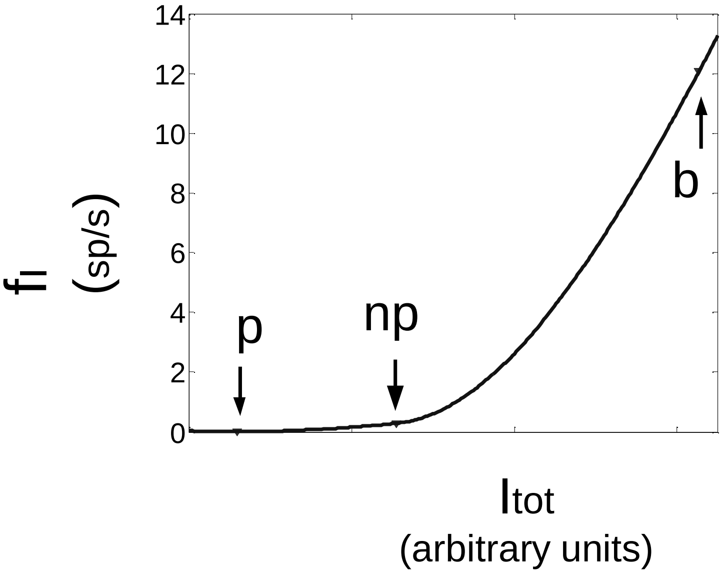

Figure 3.11: Firing rate $f_I$ of the interneurons as a function of the total synaptic input current $I_{tot}$ to the interneuron. The three arrows refer to the mean current input to the inhibitory neurons for the different conditions: 'preferred stimulus only' (p), 'non-preferred stimulus only' (np) and 'both stimuli' (b).

## Chapter 4

# Asymmetry in pulse-coupled oscillators with delay

We studied the dynamics of synchronisation in asymmetrically coupled neural oscillators with time delay. Stability analysis revealed that symmetric excitatory coupling results in synchrony at multiple phase relations. Asymmetry yields two saddle-node bifurcations of the stable states when coupling is asymmetric. By contrast, with inhibitory coupling only in phase or antiphase is stable as long as coupling is symmetric. Otherwise, these stable states shift or even vanish. The reduced bistability range suggests the beneficial role of asymmetric coupling for reliable neural information transfer.

---

Adapted from: M. Zeitler, A. Daffertshofer, and C.C.A.M Gielen, *Physical Review E* 79: 065203(R), 2009

## 4.1 Introduction

Entrainment of weakly coupled nonlinear oscillators is well known for many years (Kuramoto, 1984; Tass, 1999). More recently, the synchronisation dynamics in realistic settings received considerable interest, e.g., in nanomechanical oscillators (Shim et al., 2007), dynamic gene expression (Mazzitello et al., 2008; Horikawa et al., 2006), and in neuronal networks (Shusterman and Troy, 2008; Câteau et al., 2008; Battaglia et al., 2007), to mention a few. Interestingly, entrainment is believed to support information transfer in biological networks (Winfree, 1980; Schoffelen et al., 2005; Fries, 2005; Canolty et al., 2006). In this study, we discuss the emergence of and changes in synchronisation between realistic neuronal systems described by nonlinear pulse-coupled oscillators (Mirollo and Strogatz, 1990; Haken, 2008). Interaction between neurons is realised via changes in the membrane potential of a neuron due to the arrival of action potentials from another neuron at corresponding synapses. In several studies, neural systems were investigated in the case of symmetric coupling. Mirollo and Strogatz (1990) provided a rigourous discussion of two pulse-coupled oscillators with symmetric excitatory connections and showed that they synchronise at zero phase difference. Ernst et al. (1995, 1998) extended this study by introducing a time delay in the coupling due to finite conduction velocities of action potentials. The analytically derived return map of their model revealed that neurons with symmetric excitatory coupling synchronise at a phase lag equal to the delay, whereas in agreement with Vreeswijk et al. (1994) inhibitory coupling results in stable in-phase synchronisation, irrespective of the delay.

For two mutually connected neurons, the coupling strength from neuron *1* to neuron *2* can differ significantly from that from *2* to *1*. Symmetrical coupling between neurons is indeed the exception rather than the rule. A previous study (Senn and Urbancik, 2000) has shown that a network of excitatory all-to-all pulse-coupled oscillators without delay but with slightly different coupling strengths always synchronises, similar to the fully symmetric case in Mirollo and Strogatz (1990). If time delays are introduced in a population of excitatory neurons with symmetric coupling, the network reveals emerging and decaying synchronised clusters (Ernst et al., 1995). For inhibitory coupling with time delays, the activity reveals synchronisation in multistable clusters of common phases. A network with mainly inhibitory pulse-coupled oscillators with time delays and sparse coupling, which synchronises for symmetric coupling strengths, desynchronises when coupling strengths become asymmetric (Denker et al., 2004). For increasing variation in the coupling strengths, the network state changes to an asynchronous, aperiodic state. In the present study we will investigate the stable states and the bifurcation diagram for two asymmetrically pulse-coupled oscillators with time delays for a large range of asymmetry in the coupling, both for excitatory and inhibitory couplings. To anticipate, the analytically derived bifurcation diagrams reveal distinct patterns of mono stable and bistable states for asymmetric coupling and, more importantly, the present bifurcation routes. For the excitation, one of the states looses its stability and disappears; for inhibition, the asymmetry shifts the in-phase and antiphase solutions to stable ”out-of-phase” states.

## 4.2 Method and Theory

Like Mirollo and Strogatz (1990), we consider two Mirollo-Strogatz (MS-) oscillators with identical cycle period $T$ and describe them by their phases $\phi_i$ with $d\phi_i/dt = 1/T$. Without loss of generality, we normalise the period to $T = 1$. At $\phi_i = 0$ oscillator, $i$ is at its lowest state and at $\phi_i = 1$, i.e., at the end of the cycle, the oscillator reaches threshold, emits a pulse, and resets its phase to zero. To cover a broad class of neuron models such as the leaky-integrate-and-fire neuron with fast synaptic responses or conductance-based threshold neurons (Timme et al., 2003), we describe the state of an oscillator by a smooth, monotonically increasing, and concave function $f\colon [0,1] \to [0,1]$ as in Mirollo and Strogatz (1990) and Ernst et al. (1995),

$$f(\phi) = b^{-1} \ln\left[1 + \left(e^{b} - 1\right)\phi\right]. \tag{4.1}$$

Since the neural oscillator is confined to $f(\phi)$, an input pulse yields a state change that is tantamount to a phase shift by a fixed amount depending on coupling type and strength. Two distinct shift $\pm\varepsilon_{21}$ and $\pm\varepsilon_{12}$ have to be considered which reflect the coupling *1 → 2* and *2 → 1*, respectively; the type of coupling, i.e., excitation or inhibition, determines whether the phase will be advanced (”+”) or delayed (”−”), respectively. More formally we use the updating rule for oscillator $i$ (Ernst et al., 1995, 1998),

$$\phi^{(\pm)}_{i,\mathrm{new}} = \begin{cases} 1 \to 0 & \text{for } 1 < f(\phi_i) + \varepsilon_{ij} \\ f^{-1}\left[f(\phi_i) \pm \varepsilon_{ij}\right] & \text{for } 0 \le f(\phi_i) \pm \varepsilon_{ij} \le 1 \\ 0 & \text{for } f(\phi_i) - \varepsilon_{ij} \le 0 \end{cases}. \tag{4.2}$$

If the oscillator receives a pulse at state $f(\phi_i) > 1 - \varepsilon_{ij}$, the phase shift immediately causes a pulse and a reset to phase zero ($\phi^{+}_{i,\mathrm{new}} = 1 \to 0$). Each input changes the phase of the oscillator and thereby the time of the next firing of the oscillator. The change in the time of the next action potential for input at various phases in the cycle of the oscillator relative to the period of the oscillator defines the phase response curve (Izhikevich, 2007) of the MS-oscillator $\mathrm{PRC}^{(\pm)}[\phi_i] = \frac{T_{new} - T}{T} = \phi^{(\pm)}_{i,\mathrm{new}} - \phi_i$.

Positive (negative) values of this function correspond to phase advances (delays) in the sense that they advance (delay) the time of the next spike.

We assess stability of the system via the phase difference at times $t_k$ at which oscillator *1* generates the $k$th pulse, i.e., $\Phi_k = \phi_2(t_k) - \phi_1(t_k)$. Because oscillator *1* fires and resets immediately, $\phi_1(t_k) \rightarrow 0$ holds, and $\Phi_k = \phi_2(t_k)$ can be simplified. This stroboscopic view yields the system's return map $R[\Phi]$ with fixed points $R[\Phi^*] = \Phi^*$. To illustrate the subsequent stability classification[1], we briefly sketch the synchronisation characteristics in the case of two excitatory couplings (Mirollo and Strogatz, 1990); the inhibitory case can be treated equivalently. For instantaneous couplings, i.e., without finite conduction delays, three different regimes can be distinguished depending on the firing moments $t_k$ and the $\mathrm{PRC}^{(+)}$. We note that here the latter is readily parameterised via the coupling strength $\varepsilon_{ij}$ since we fixed $b$. In regime I, oscillator *1* receives a pulse from oscillator *2* late in its cycle and fires immediately, i.e., both are synchronised in phase. In regime II, *1* receives a pulse and returns it with a finite lag and so does *2*, i.e., the system is synchronised out of phase. Finally, in regime III, oscillator *1* reacts with a certain lag but *2* does reply immediately yielding again in-phase synchronisation. The corresponding return maps reveal that the synchronised states are stable in I and III but not in II. That is, the oscillators always synchronise with zero phase lag (in phase). Further, we incorporate a delay because the emitted pulse may arrive at the other oscillator after a finite time $\tau$. With delay, an excitatory coupling results not in three but 14 different regimes. The corresponding return maps contain in total six fixed points, from which one half is asymptotically stable and the other half is unstable. The latter separate the attraction domains of the stable fixed points. Unlike the excitatory coupling, inhibition with delay results in marginally stable fixed points next to the asymptotically stable ones.

## 4.3 Results

Figure 4.1 shows the fixed points of the return map as a function of coupling strengths $\varepsilon_{ij}$ and delay $\tau$; in all figures we used $b = 3$. With symmetric coupling $\varepsilon_{21} = \varepsilon_{12} = \varepsilon$, two stable fixed points coexist for small delay $\tau$ as shown in Fig. 4.1B (upper panel). One state is at $\Phi^* = \tau$ which implies that oscillator *2* drives *1*, which in response, fires an action potential immediately after the arrival of the pulse. The other one is at $\Phi^* = 1 - \tau - \mathrm{PRC}^{(+)}(2\tau)$. The arrival of the $\tau$-delayed pulse of oscillator *1* yields a phase shift $\mathrm{PRC}^{(+)}(2\tau) > 0$, which shortens the period of os-

---

[1] The map $R[\Phi] \in [0,1]$ is defined via $R[\Phi_k] = \Phi_{k+1}$. Fixed points $R[\Phi^*] = \Phi^*$ are asymptotically stable for $|R'| < 1$, unstable for $|R'| > 1$, and marginally stable if $|R'| = 1$ when $R'$ denotes the map's derivative with respect to $\Phi$.

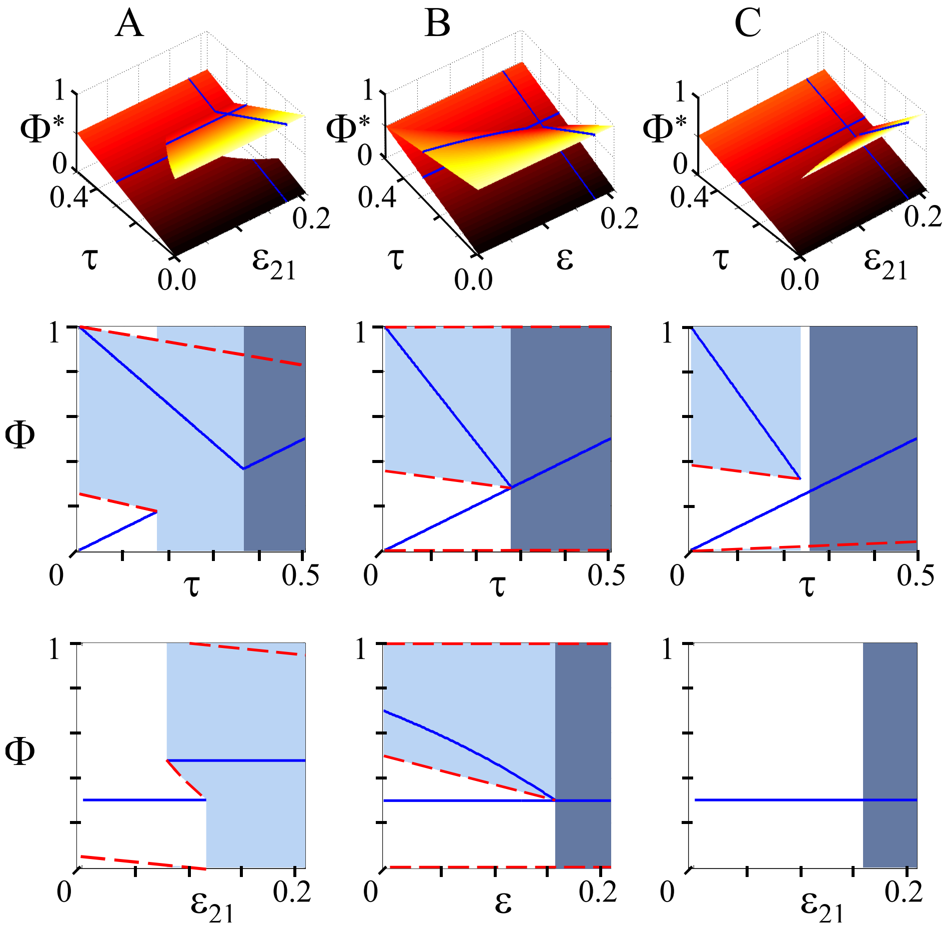

Figure 4.1: (Un-)stable states for two excitatory, pulse-coupled oscillators with delay. (A) asymmetric coupling with $\varepsilon_{12} = 0.1$. (B) symmetric coupling with $\varepsilon_{21} = \varepsilon_{12} = \varepsilon$. (C) Asymmetric coupling with $\varepsilon_{12} = 0.2$. Top: asymptotically stable fixed points of the return map as a function of $\tau$ and $\varepsilon_{21}$. Blue lines represent the cross-sections shown in middle and bottom rows. Middle: stable (blue, solid line) and unstable (red, dashed line) fixed points and their attraction domains as a function of $\tau$ for $\varepsilon_{21} = 0.18$. Bottom: same as middle row as a function of coupling strength for $\tau = 0.3$.

cillator *2* to $T_{\text{new}} = 1 - \text{PRC}^{(+)}(2\tau)$ and induces a pulse delayed by $\tau$ after *1* has fired. The resulting phase shift increases for larger delays because $\text{PRC}^{(+)}(2\tau) = 2\tau\left[\left(1/\phi^{(+)}_{\text{crit}}\right) - 1\right]$; here we abbreviated $\phi^{(+)}_{\text{crit}} = \left(e^{b(1-\varepsilon_{12})} - 1\right) / \left(e^{b} - 1\right)$ (see also the appendix). The period of the coupled system hence decreases for increasing $\tau$ until it reaches $T_{\text{new}} = 2\tau$. For larger values of $\tau$, the period increases and only one stable state remains representing antiphase synchrony, i.e., $\Phi^* = 0.5T_{\text{new}} = \tau$. At $\varepsilon = 1 - b^{-1}\ln\left[2\tau\left(\mathrm{e}^b - 1\right) + 1\right]$, two stable states merge via a supercritical pitchfork bifurcation into a single stable state in which the neurons oscillate in antiphase [Fig. 4.1B, middle and lower panels]. Put differently, in the absence of time delays, an excitatory coupling leads to in-phase synchronisation (Mirollo and Strogatz, 1990), whereas a delay yields out-of-phase synchronisation (Vreeswijk et al., 1994; Ernst et al., 1998). Note that the dynamics of synaptic connections, which is typically modelled via $\left(t/\tau_s^2\right)\exp\{-t/\tau_s\}$ may add to the here-discussed delay so that larger values of $\tau_s$ may contribute to the aforementioned supercritical pitchfork bifurcation from out-of-phase into antiphase synchrony (Vreeswijk et al., 1994). The explicit form of that dynamics, however, does not alter the qualitative behaviour of our system so that a pulselike coupling appears proper for the current discussion.

As soon as the synaptic coupling strengths differ ($\varepsilon_{12} \neq \varepsilon_{21}$), the pitchfork bifurcation is no longer present and the upper stable state $\Phi^* = T_{\text{new}} - \tau$ disappears for

$$\varepsilon_{21} < 1 - b^{-1}\ln\left[1 + (\mathrm{e}^b - 1)\left(1 - \frac{2\tau(1-\phi_{\text{crit}}^{(+)})}{\phi_{\text{crit}}^{(+)}}\right)\right], \tag{4.3}$$

e.g., in the lower panel of Fig. 4.1A. That is, there is only one stable branch $\Phi^* = \tau$, in which oscillator *2* drives oscillator *1*, which, in turn, disappears for

$$\varepsilon_{21} > 1 - b^{-1}\ln\left[1 + \frac{\mathrm{e}^b - 1}{1 + \frac{1-\phi_{\text{crit}}^{(+)}}{2\tau}}\right]. \tag{4.4}$$

Stable states and corresponding attraction domains are shown in the lower panel of Fig. 4.1A as a function of coupling strength $\varepsilon_{21}$. At a critical value $\varepsilon_{21} < \varepsilon_{12}$, the upper stable state merges with an unstable equilibrium through a saddle-node bifurcation and vanishes for smaller $\varepsilon_{21}$. For slightly larger coupling strength $\varepsilon_{21}$, the lower stable state merges with an unstable state. Figure 4.1A (middle panel) shows the corresponding stable and unstable states as a function of $\tau$ for $\varepsilon_{12} < \varepsilon_{21}$. For this asymmetry, the pitchfork bifurcation at $\varepsilon_{12} = \varepsilon_{21}$ (4.1B, middle panel) disappears and a saddle-node bifurcation emerges. The two excitatory coupled oscillators are precisely in antiphase if both coupling strengths $\varepsilon_{ij}$ obey

$$\varepsilon_{ij} \geq 1 - b^{-1}\ln\left[2\tau(\mathrm{e}^b - 1) + 1\right]. \tag{4.5}$$

From Fig. 4.1 and Eq. (4.5), we can conclude that only if

$$\varepsilon_{12} = \varepsilon_{21} = 1 - b^{-1}\ln\left[2\tau(\mathrm{e}^b - 1) + 1\right], \tag{4.6}$$

the two stable out-of-phase states will merge (in the antiphase state). The supercritical pitchfork bifurcation, which is characteristic for excitatory symmetrically pulse-coupled oscillators with delay, does not exist for asymmetric coupling and is replaced by two saddle-node bifurcations with two stable states, at least when the difference between the two coupling strengths is sufficiently small.

If coupling is inhibitory, the spectrum of solutions and bifurcations changes entirely. Figure 4.2B shows the results for inhibitory symmetrically pulse-coupled oscillators with delay. The in-phase synchronisation $\Phi^* = 0$ is a stable state for all coupling strengths and delays and a stable antiphase state exists for

$$\varepsilon \leq -b^{-1} \ln \left[ \frac{2\tau - 1}{1 + \frac{1}{\mathrm{e}^b - 1}} + 1 \right]; \tag{4.7}$$

[see upper surface in Fig. 4.2B (upper panel) and the cross-section at fixed $\tau$ in the lower panel]. Since unstable states are absent, the attraction domain of the antiphase solution is an open manifold. If the phase difference $\Phi$ lies on one of the two separatrices, here at

$$\Phi = 1 - \tau \;\text{ and }\; \Phi = \left(2\mathrm{e}^{b\varepsilon} - 1\right)\tau + \phi_{\mathrm{crit}}^{(-)}, \tag{4.8}$$

it converges to the stable in-phase state or to the region of marginal stability ($\varepsilon \geq b^{-1} \ln \left[\tau \left(\mathrm{e}^b - 1\right) + 1\right]$). The cross section for fixed $\tau$ [Fig. 4.2B, lower panel] shows that in-phase and antiphase states coexist for small $\varepsilon$ and marginally stable states exist for large $\varepsilon$, which agrees with previous studies (e.g., Ernst et al., 1995). In the middle and lower panels of Fig. 4.2B we find that one stable fixed point and two separatrices merge and vanish. This bifurcation occurs at

$$\varepsilon = -b^{-1} \ln \left[ \frac{2\tau - 1}{1 + 1/\left(\mathrm{e}^b - 1\right)} + 1 \right]. \tag{4.9}$$

If asymmetry is introduced to the inhibitory coupling, the in phase and antiphase do not remain stable [upper panels of Figs. 4.2A and 4.2C]. The stable state $\Phi^* = 0$ changes to a stable phase difference near zero [middle and lower panels of Figs. 4.2A and 4.2C]. Similarly, a stable near antiphase state exists for a range of values for $\tau$ and $\varepsilon$ being smaller than for the antiphase oscillation in the symmetrically coupled system. For $\varepsilon_{12} < \varepsilon_{21}$, this state merges with the lower separatrix for

$$\varepsilon_{21} = b^{-1} \ln \left[ 1 - \frac{\mathrm{e}^{-b\varepsilon_{12}} - 1}{\mathrm{e}^{-b} + 2\tau\left(1 - \mathrm{e}^{-b}\right)} \right]; \tag{4.10}$$

[see also the right-hand side of the stable state range in the middle panel of Fig. 4.2A

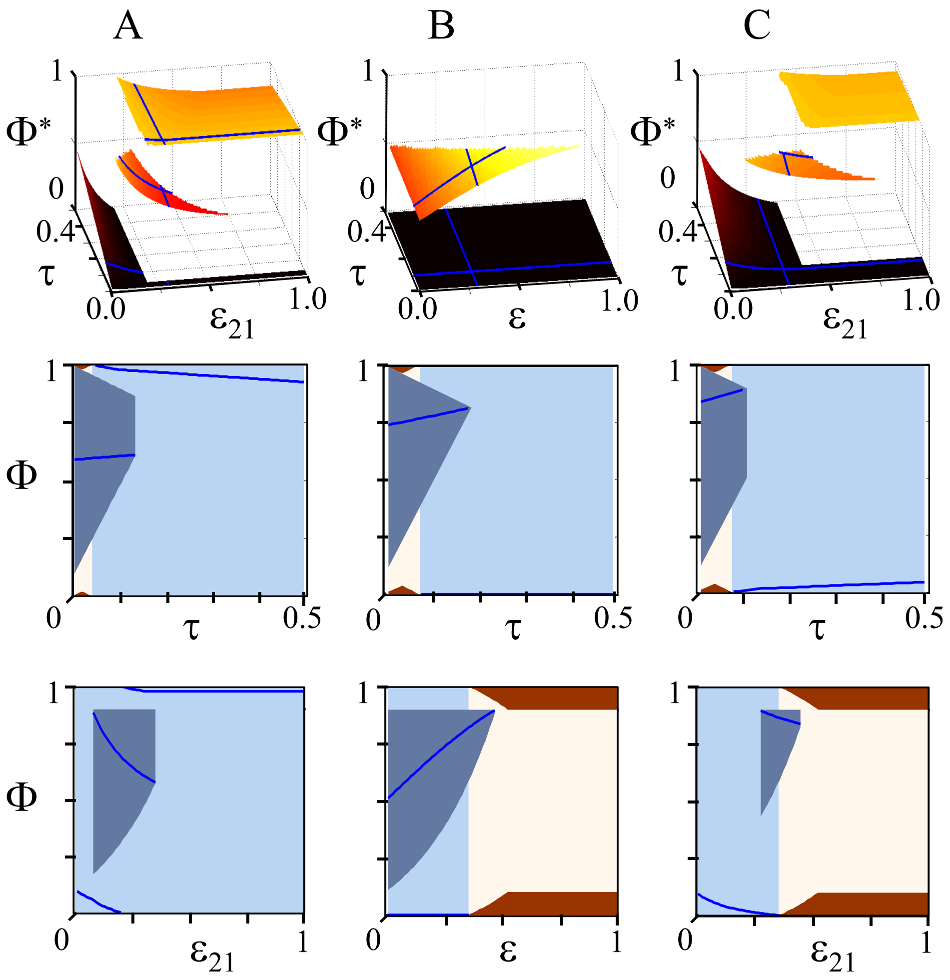

Figure 4.2: (Un-)stable states for two inhibitory pulse-coupled oscillators with delay. (A) asymmetric case with $\varepsilon_{12} = 0.2$. (B) symmetric case: $\varepsilon_{21} = \varepsilon_{12} = \varepsilon$. (C) asymmetric coupling with $\varepsilon_{12} = 0.4$. Asymptotically stable fixed points $\Phi^*$ of the return map as a function of $\tau$ and $\varepsilon_{21}$ [cf. Fig. 4.1 now with $\varepsilon_{21} = 0.3$ (middle row) and $\tau = 0.1$ (bottom row)].

and the lower panels of Figs. 4.2A, and 4.2C. Similarly, for $\varepsilon_{12} > \varepsilon_{21}$, the near antiphase state merges with the upper separatrix at

$$\varepsilon_{21} = -b^{-1} \ln \left[1 + \left(1 - e^{b\varepsilon_{12}} \left(2\tau(1 - e^{-b}) + e^{-b}\right)\right)\right]; \tag{4.11}$$

[see the left-hand side of the stable state range in the lower panels of Figs. 4.2A, and 4.2C and the right-hand side of the stable state range in the middle panel of Fig. 4.2C]. At $\Phi^* = 0$, a degeneration to multiple stable states occurs if the minimum value of the actual coupling strengths equals $b^{-1} \ln \left[\tau \left(\mathrm{e}^{b} - 1\right) + 1\right]$ [see middle panels of Figs. 4.2A and 4.2C and lower panel of Fig. 4.2C]. Notice that the dynamics of synapses, i.e., $\left(t/\tau_s^2\right) \exp\left\{-t/\tau_s\right\}$ in the inhibitory case with delay makes the marginally stable states disappear and causes the co-existence of stable in phase and antiphase states for all delays and coupling strengths as long as coupling is symmetric. For asymmetric coupling, two stable states coexist, which are not precisely in phase or antiphase.

Figure 4.3 summarises the results for different values of $\tau$. A system with two excitatory pulse-coupled oscillators with delay hence reveals monostability or bistability depending on $\varepsilon_{12}$, $\varepsilon_{21}$, and $\tau$. At the transition from monostability to bistability, a saddle-node bifurcation is found. These two saddle-node bifurcations meet at the diagonal $\varepsilon_{12} = \varepsilon_{21}$ and combine into a supercritical pitchfork bifurcation.

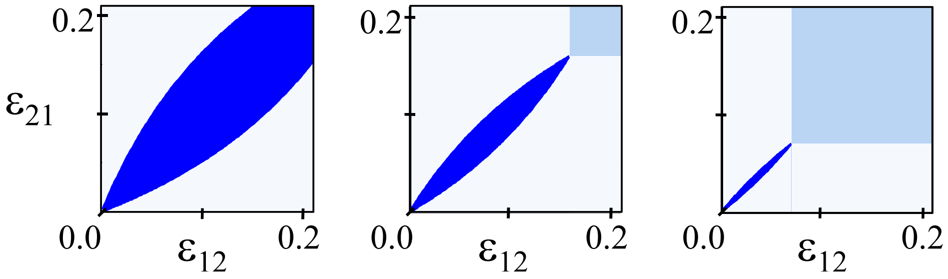

Figure 4.3: Number of stable states for two asymmetric pulse-coupled oscillators as function of excitatory coupling strengths $\tau = \{0.2, 0.3, 0.4\}$ (from left to right). Dark blue areas corresponds to bi-stability contrasting mono-stability outside this area. The light-blue square in the right upper corner represents the region where the two oscillators are in antiphase.

## 4.4 Discussion

Several studies have studied asymmetry in the coupling between excitatory oscillators. For small differences in mutual coupling strength, the results are qualitatively similar to that for symmetrical coupling (Senn and Urbancik, 2000). In this study, we show that two stable states merge into a single stable state, when the differences in coupling strengths increase. Networks with inhibitory pulse-coupled oscillators behave qualitatively different. Denker et al. (2004) showed that a population of mainly inhibitory pulse-coupled oscillators desynchronises if asymmetry in coupling strengths increases. In addition to Denker et al. (2004), who started with a synchronised network which turns into a desynchronised state for asymmetric coupling, we find that both the in-phase and anti-phase states become unstable.

Symmetrically and asymmetrically coupled oscillators show qualitatively different behaviour of monostability/bistability. Asymmetric excitatory coupling yields a bifurcation pattern in which two saddle-node bifurcations merge into a pitchfork bifurcation when switching to symmetry. For inhibitory coupled oscillators two stable states are present corresponding to either in phase or antiphase synchronisation in the symmetric case or near in phase or antiphase for asymmetric coupling. In the latter case, stable states vanish by merging with a separatrix. When synaptic dynamics are incorporated, marginal stability vanishes and the symmetric inhibitory coupled system has two stable states for all coupling strengths and delays. Irrespective of the coupling type (excitatory or inhibitory, with or without synaptic dynamics), asymmetry generally leads to a smaller range of bi-stability as compared to its symmetric counterpart. A pronounced asymmetry in coupling hence supports the (directed) information exchange between neurons. Information is transmitted reliably in one direction since the receiving excitatory neuron will instantaneously emit a pulse after the arrival of the pulse from the sending neuron. The bifurcation diagrams show that the transfer of information is robust for fluctuations in coupling strength. Transmission is readily achieved since the receiving neuron is driven by the sending neuron and the phase relation between the neurons does not change in case of small changes in coupling strengths caused by the synaptic plasticity.

## Acknowledgements

This work was supported by the Netherlands Organisation for Scientific Research (NWO 051.02.050 & 452.04.344).

## APPENDIX

The PRC of Mirollo and Strogatz showed always a phase advance if the oscillator generates a pulse, which seems improper for realistic neurons. Hence, we corrected

$$\mathrm{PRC}^{(+)} = 1 - \phi + \begin{cases} \phi/\phi_{\mathrm{crit}}^{(+)} - 1 & \text{for } \phi \leq \phi_{\mathrm{crit}}^{(+)} \\ 0 & \text{otherwise} \end{cases} ;$$

where $\phi_{\mathrm{crit}}^{(+)} = \left(\mathrm{e}^{b(1-\varepsilon)} - 1\right) / \left(\mathrm{e}^{b} - 1\right)$ represents the phase at which the maximum shift is reached. When a pulse arrives at the oscillator at phase $\phi > \phi_{\mathrm{crit}}^{(+)}$, the oscillator emits a pulse. For biological systems, the phase shift reaches its maximum when the input arrives in the second half of the cycle period (see Tsubo et al., 2007)), i.e., $\phi_{\text{crit}}^{(+)} > 0.5$, yielding $\varepsilon \leq 0.21$. Similarly, for the inhibitory case, we used

$$\text{PRC}^{(-)} = -\phi + \begin{cases} \mathrm{e}^{-b\varepsilon}\left(\phi - \phi_{\text{crit}}^{(-)}\right) & \text{for } \phi > \phi_{\text{crit}}^{(-)} \\ 0 & \text{otherwise} \end{cases} ;$$

with $\phi_{\text{crit}}^{(-)} = \left(\mathrm{e}^{b\varepsilon} - 1\right) / \left(\mathrm{e}^{b} - 1\right)$ and $\phi \in [0, 1)$. Note that here the coupling is not bounded apart from $\varepsilon < 1$.

## Chapter 5

# Effective communication by neuronal coherence: a model study

Cognitive function requires flexibility in the routing of signals through the brain such that different brain regions are functionally connected depending on the context and intention of the subject. The flexible organisation of communicating subsets of neuronal populations in the brain is thought to be implemented by coherent rhythmic changes in neuronal excitability as postulated by the communication-through-coherence (CTC) hypothesis.

In a previous study (van Elswijk et al., 2009) Transcranial Magnetic Stimulation (TMS) of motor cortex was used to test the CTC-hypothesis. The amplitude of the TMS induced Motor Evoked Potential (MEP) appeared to depend on the phase of the spinal cord activity, reflected in the EMG, in agreement with the CTC-hypothesis. In this study, we developed a corticospinal model to reproduce and understand the experimental findings obtained by van Elswijk et al. (2009). Using advanced analysis techniques we find that the effectiveness of information transfer between two populations depends on the phase of the ongoing activity of the receiving neuronal population at the arrival of the TMS-induced spike volley. The correlation within the receiving population determines the difference in maximum and minimum communication effectiveness.

Our simulation results are the first computational results which support the CTC-hypothesis. Moreover, our results explain how the CTC-hypothesis can be implemented in neuronal interactions and reveal the underlying mechanisms that facilitate effective communication by coherent neuronal activity.

---

In preparation M. Zeitler, J. Tramper, D.F. Stegeman, and C.C.A.M. Gielen

## 5.1 Introduction

In many daily-life activities the brain has to select relevant information in order to give adequate behavioural responses in a changing environment. This implies that, depending on context, identical physical sensory information may be processed differently in order to meet the specific goals of the organism. This means that on top of the anatomical connections, we need a communication structure that is flexible in effectiveness, so that depending on the relevance of the stimulus, we can ignore it completely or focus on it.

Recently, Fries (2005) postulated a possible mechanism to realise a flexible effective communication structure: the pattern of coherence within and among neuronal groups. The central argument in this communication-though-coherence (CTC) hypothesis is that activated neuronal groups have the intrinsic property to oscillate and that those oscillations in population activity cause modulations in excitability, which do relate the likelihood of spike output to the sensitivity to specific neuronal inputs. This hypothesis implies that neuronal groups adjust the frequency and phase of the oscillations to optimise communication and information transfer. Only coherently oscillating neuronal groups are thought to be able to interact effectively in time, because their communication windows for input and output are open at the proper time periods. There are several experimental observations, which are in support of this hypothesis, not only in the gamma band in the visual system, as reported by Fries et al. (2001b, 2005) and Womelsdorf et al. (2007)), but also for the beta band (see e.g. Schoffelen et al., 2005). Beta-band activity has been found to synchronise between two remote electrode sites at the time when information is passed from one brain area to another (Nicolaev et al., 2001). Moreover, field potential recordings from motor cortex in monkey (Baker et al., 1997; Baker, 2007) have shown that oscillations in the beta band are coherent with similar oscillations in the activity of contralateral contracting muscles. This finding is in agreement with the hypothesis of Fries that flexible effective communication between groups of neurons is possible by rhythmic excitability fluctuations which, at the appropriate relative phase, produce temporal windows for communication.

In order to test this hypothesis, van Elswijk et al. (2009) recorded the electromyogram (EMG) of the first dorsal interosseus muscle while subjects maintained an isometric contraction. During isometric contraction, the motor system engages in rhythmic synchronisation in the beta-frequency range (Kilner et al., 2000; Schoffelen et al., 2005; Conway et al., 2001; Waldert et al., 2008) where oscillations in EEG are coherent with oscillations in EMG activity in arm and hand muscles (Conway et al., 2001; Baker et al., 1997; Salenius et al., 2000; Hari and Salenius, 1999; Kilner et al., 1999). Van Elswijk et al. (2009) tested the effectiveness of neuronal communication between motor cortex and spinal cord by applying an excitatory input by transcranial magnetic stimulation (TMS) at different phases of the EEG and EMG oscillations. In the study of van Elswijk et al. (2009) TMS pulses were applied to the contralateral motor cortex at random moments in order to test whether the input gain of $\alpha$-motoneurons in the spinal cord is modulated by the phase of the spinal beta-rhythm. A TMS pulse generates a motor-evoked potential (MEP) in the muscle EMG. The amplitude of this MEP was related to the phase of the EMG, which reflects spinal beta-rhythm, when the input volley induced by the TMS pulse arrived. This finding demonstrates that the motor system′s physiological beta-rhythm entails rhythmic changes in excitability of the spinal cord.

Contrary to the EMG findings, van Elswijk et al. (2009) observed that the amplitude of the MEP appeared to be unrelated to the phase of the EEG beta-rhythm at which the input volley arrived. In this study we have developed a detailed model for the cortical-spinal system to investigate why the MEP amplitude is related to the pre-TMS EMG-phase, and not the pre-TMS EEG-phase. In particular we will explore the interaction between various components in the model which are important for this flexible communication effectiveness such as the cortical-spinal beta-rhythm and the firing rate of the neurons in motor cortex, and the firing rate of the $\alpha$-motoneurons in the spinal cord. All three peak around 20 Hz, 20 spikes/s, respectively. The model for the corticospinal system consists of Hodgkin-Huxley neurons that mimic the dynamics of neurons in motor cortex and spinal cord. Moreover, the model simulates the motor-unit action potentials in muscle to reproduce the EMG signal. This allowed us to simulate the experiments by van Elswijk et al. (2009). By variations in the model parameters we were able to explore the critical properties of neuronal interaction that are responsible for flexibility in neuronal communication.

## 5.2 Theory and Methods

In this chapter, the cortico-spinal model will be explained (see Figure 1). First, we will describe the neurons in motor cortex and spinal cord. The objective is to build a model that includes the essential properties of the cortical neurons and $\alpha$-motoneurons, but lacks details, which may obscure its basic mechanisms. Therefore, the neuron model is based on a simple Hodgkin-Huxley model. For the $\alpha$-motoneuron, this model is extended by a slow potassium current (Jones and Bawa, 1997) to incorporate the long after-hyperpolarisation, which is characteristic for $\alpha$-motoneurons. Then we describe the cortico-spinal model by two interacting populations of neurons in order to simulate neural activity in motor cortex, spinal cord, and muscle (represented by the EMG signal). The motoneuron model and the neural networks were implemented in Neuron (www.neuron.yale.edu).

### 5.2.1 Motoneuron model

A one-compartmental Hodgkin-Huxley model was developed to simulate the firing behaviour of the neurons in the spinal cord. The model was based on multi-compartment models by Jones and Bawa (1997) and Vieira and Kohn (2007). For simplification we reduced these models to a single-compartment model.

The soma was represented by a sphere with diameter $D$. The specific membrane capacitance $C_m$ was 1.0 F/cm$^2$ and the specific cytoplasmic resistivity $R_i$ was 70 $\Omega \cdot$ cm (Fleshman et al., 1988).

Active cell properties were introduced by three different voltage-gated ion currents, i.e. a sodium current, and a fast and slow potassium current (see Appendix for a detailed description of the model equations). The membrane potential $V_m$ of the motoneuron is given by the following differential equation:

$$C_m \frac{dV_m}{dt} = -G_{Na}(V_m - E_{Na}) - (G_{K,fast} + G_{K,slow})(V_m - E_K) - G_L(V_m - E_L) + I_{ext}(t) \tag{5.1}$$

$G_{Na}$, $G_{K,fast}$ and $G_{K,slow}$ are the electrical conductances for sodium, fast potassium and slow potassium currents, respectively. $E_{Na}$ and $E_K$ are the reversal potentials for sodium and potassium, respectively. $G_L$ is the leak conductance and $E_L$ is the leak-current reversal potential. $I_{ext}$ is an externally applied current, which in our case can be a synaptic input or input current elicited by a TMS pulse.

Several studies have reported that $\alpha$-motoneurons show a long after-hyperpolarisation (AHP) (Kernell and Zwaagstra, 1989), which is due to slow calcium-dependent potassium currents, which depend on variations in the intracellular calcium concentration (Vieira and Kohn, 2007). Since we are interested in modelling the functional properties of the motoneuron rather than the detailed biophysical mechanisms, we do not model the calcium-mediated process for simplicity. Therefore, the long AHP was implemented by introducing a slow calcium-independent potassium current. This current is a function of the activation variable $q$ (see Aradi and Holmes, 1999). The activation of the slow current potassium channel remains near zero as long as the membrane potential is below the threshold for spiking and then quickly rises to full activation if an action potential is elicited, after which it decays exponentially. For the slow potassium current, the decay time is long compared to the fast current. Since the outflow of potassium pulls the membrane potential towards the reversal potential of potassium, a new action potential can only be elicited if the potassium current has become small compared to the depolarising current.

| Parameter | Value | Description |
|---|---|---|
| $D$ | $89\ \mu$ m [d] | cell diameter |
| $C_m$ | 1.0 F / cm$^2$ [a] | specific membrane capacitance |
| $R_i$ | 70 $\Omega \cdot$ cm [a] | specific cytoplasmic resistivity |
| $G_L$ | 1 mS/cm$^2$ [a] | leak conductance |
| $g_{Na}^{max}$ | 140 mS/cm$^2$ [a] | maximum sodium conductance |
| $g_{K,fast}^{max}$ | 35 mS/cm$^2$ [a] | maximum potassium conductance, fast current |
| $g_{K,slow}^{max}$ | 35 mS/cm$^2$ [a] | maximum potassium conductance, slow current |
| $E_L$ | 0 mV | leak current reversal potential |
| $E_{Na}$ | 115 mV [a] | sodium reversal potential |
| $E_K$ | -10 mV [a] | potassium reversal potential |
| $E_{syn}$ | 70 mV [c] | excitatory synaptic reversal potential |
| $\tau_s$ | 0.2 ms [b] | time constant of alpha synapse |

Table 1. Motoneuron model parameters. These values were taken from (a) Jones and Bawa (1997), (b) Vieira and Kohn (2007), (c) Destexhe et al. (2001) and (d) van der Heyden et al. (1994). Note that in this paper, like in Vieira and Kohn (2007), the membrane potential of the neuron at rest was defined relative to a rest potential of -70 mV.

The synaptic input $I_{syn}(t)$ was modelled using the standard synaptic current given by

$$I_{syn}(t) = g_{syn}(t)(V_m(t) - E_{syn}). \tag{5.2}$$

In this study, the rest potential was defined relative to a rest potential of -70 mV and therefore all other relevant parameters were adjusted to this rest potential, e.g. reversal potential of the excitatory synaptic input was set to $E_{syn}$ = 70 mV. For the conductance $g_{syn}(t)$ the usual alpha-function was chosen (see appendix) with a time constant of 0.2 ms (Vieira and Kohn, 2007) and a maximum unitary conductance of $\varepsilon = 0.4/17\ \mu$S.

### 5.2.2 Properties of the spinal motoneuron pool

The size-principle (Henneman et al., 1965; Burke, 1981) is one of the oldest dogmas in the neurophysiology of the motor system. It states that the fine control of muscle tension depends on the orderly recruitment of motor neurons in a heterogeneous pool. Recruitment is related to the size of the motoneuron soma in the sense that motoneurons with the smallest soma are recruited first. To simulate the response of an ensemble of motoneurons we assigned a different size $S$ of the soma to each $\alpha$-motoneuron. The size $S$ gives the relative membrane area (van der Heyden et al., 1994) and is thus related to the diameter $D$ by

$$S = \frac{D^2}{D_{max}^2} \quad (0 < S < 1) \tag{5.3}$$

where $D_{max}$ is the maximum diameter, i.e. the soma diameter of the largest motoneuron in the pool. The maximum diameter $D_{max}$ was derived from the maximum membrane area reported in van der Heyden et al. (1994). This resulted in $D_{max}$ = 126 $\mu m$. For each size of the soma of the motoneuron, the total conductance and capacitance of the cell membrane were calculated using the parameter values for the specific membrane capacitance $C_m$ and the specific cytoplasmic resistivity $R_i$ in Table 1.

The population of $\alpha$-motoneurons (see Figure 1) was represented by 17 neurons with different soma sizes to account for the size principle. Cell diameters of the $\alpha$-motoneurons in our study were equally distributed from 88 to 104 $\mu$m. According to the size principle motoneurons with a large soma are recruited only for large forces, which did not occur in the study by Mitchell et al. (2007)) and van Elswijk et al. (2009). Therefore, in our study motoneurons with a cell diameter larger than 104 $\mu$m were considered to be inactive. Since the firing rate of $\alpha$-motoneurons depends both on descending projection from motor cortex, as well as on projections from afferent input from various muscle receptors (Webb and Cope, 1992; Macefield et al., 1993) and on plateau potentials (Binder et al., 1993; Kiehn and Eken, 1998), we added an additional current of 10 nA to the $\alpha$-motoneurons. Because of the different soma sizes, the same input gives higher firing rates for cells with a small soma than for cells with a large soma.

Experimental data of cat hindlimb motoneurons has revealed an unexpectedly small input resistance for large motoneurons (Kernell and Zwaagstra, 1989). This resistance was attributed to a relatively high leak conductance (or specific resting membrane conductance) for large motoneurons. Therefore, a linear scaling of the leak conductance was incorporated into the model by the following expression (taken from van der Heyden et al., 1994)

$$G_L = G_{L,min} + S(G_{L,max} - G_{L,min}) \tag{5.4}$$

where $G_{L,min}$ and $G_{L,max}$ represent the leak conductances for the smallest and largest cell in the pool, respectively. The values for these conductances were determined by assuming that the median cell size ($S$ = 0.5) gives a conductance $G_L$ of 1.0 mS/cm$^2$ and that $G_{L,max}$ = 3.3 $G_{L,min}$ (Kernell and Zwaagstra, 1989). This resulted in $G_{L,min}$ = 0.47 mS/cm$^2$ and $G_{L,max}$ = 1.5 mS/cm$^2$.

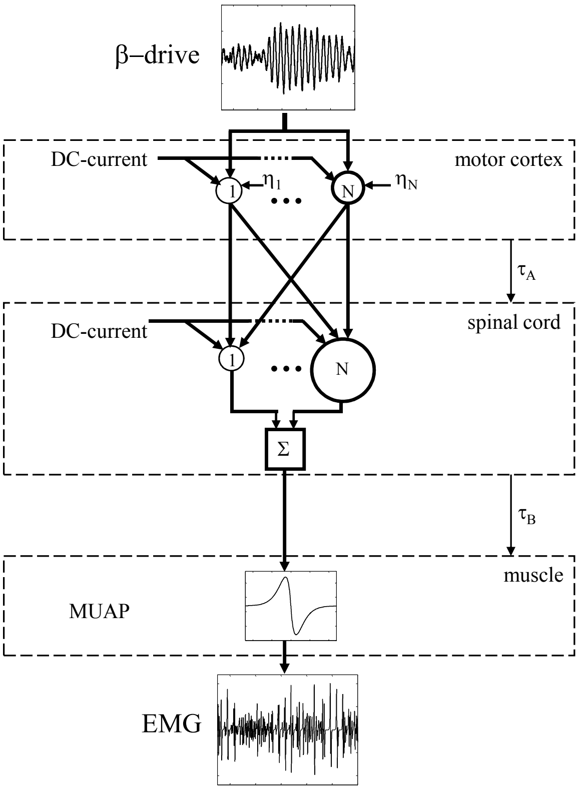

Figure 5.1: A schematic overview of the cortico-spinal model. The motor cortex is represented by 17 neurons with soma diameters equally distributed in the range from from 86 to 92 $\mu$m resulting in firing rates between 18.5 and 21.5 spikes/s by stimulation with a constant input current of 10 nA, the GWN-filtered beta-drive (with standard deviation of 0.05 nA) and the neuron-specific GWN noise, $\eta_i$ (with standard deviation of 0.10 nA). The spinal cord is modelled by a set of 17 neurons with soma diameters equally distributed in the range from 88 to 104 $\mu$m, that receive a DC-current of 10 nA and the spike activity of the motor cortex (resulting in firing rates between 15 and 21 spikes/s). Each cortical cell projects to all 17 $\alpha$-motoneurons by the same coupling strength $\varepsilon = \varepsilon_{SM}/17$. $\varepsilon_{SM}$ represents the total coupling strength from motor cortex to an $\alpha$-motorneuron in the spinal cord and is set to 0.4 $\mu$S. Spikes from cells in motor cortex arrive at the $\alpha$-motoneurons in the spinal cord after a delay $\tau_A$ = 8 ms. All spikes generated by the $\alpha$-motoneurons are summed and after convolution with the MUAP make up the EMG signal. A delay $\tau_B$ of 14 ms is introduced between spinal cord and the first dorsal interosseus (muscle). In addition to conduction delays of 8 ms from motor cortex to spinal cord and of 14 ms from spinal cord to first dorsal interosseus, the dynamics of synapses and neuronal dynamics adds another 1 ms such that the total time between TMS pulse to motor cortex and EMG onset is 23 ms. A TMS pulse is simulated by the activation of a special $\alpha$-synapse on all neurons in motor cortex with a maximum conductance of 5 mS, $\tau_{syn}$ = 0.2 ms and $E_{syn}$ = 70 mV. TMS pulses are given at random times with at least 300 ms between two successive TMS pulses.

### 5.2.3 Properties of neurons in primary motor cortex

Cells in motor cortex fire at a relatively low firing rate of about 20 Hz (Baker et al., 2001). This relatively low firing rate is presumably caused by intracortical inhibitory circuits (Ferbert et al., 1992; Kujirai et al., 1993; Werhahn et al., 1999). Since we are interested in cortico-spinal interactions, we did not develop a detailed biologically plausible model for the neurons in motor cortex. For our purpose, it is sufficient to have a model that replicates the firing properties of a cortical neuron, irrespective of the detailed underlying mechanisms. Therefore, the model for the neurons in motor cortex was the same as that for the $\alpha$-motoneuron, where the low firing rate is caused by a long AHP instead of inhibitory mechanisms.

The population of cells in motor cortex was represented by 17 neurons with cell diameters equally distributed from 86 to 92 $\mu$m, resulting in slightly different firing rates (range from 18.3 to 21.5 spikes/s) when current clamped at 10 nA. This is well in agreement with experimental observations (Baker et al., 2001; Davies et al., 2006; Witham and Baker, 2007). Leak conductances for all 17 cells were scaled according to Equation 5.4. Each of the cortical cells was connected to all 17 $\alpha$-motoneurons in the spinal cord by the same coupling strength $\varepsilon = \varepsilon_{SM}/17$, where $\varepsilon_{SM}$ represents the total coupling strength from motor cortex to a motoneuron in the spinal cord. $\varepsilon_{SM}$ was set to 0.4 $\mu$S.

Each neuron in motor cortex receives a common input, which consists of a DC current injection of 10 nA to produce a mean firing rate of the cells in motor cortex, and a signal responsible for the beta rhythm. The level of DC current injection was adjusted such that approximately 35% of the population of $\alpha$-motoneurons was active, corresponding to a mean force output of about 15% maximum voluntary contraction (MVC), similar to the isometric force in the studies by Mitchell et al. (2007) and van Elswijk et al. (2009). In order to simulate beta activity in the motor cortex, the cortical neurons are modulated by an oscillatory current which was obtained by band-pass filtering Gaussian White Noise with a filter with a centre frequency at 20 Hz and a Q-factor of 17.9 (defined as the ratio of the centre frequency, divided by the width of the filter spectrum at 3 dB) (see Figure 5.3A). This band-pass filtered beta-drive had a standard deviation of 0.05 nA. This coloured Gaussian noise has roughly the same spectral properties as the MEG spectrum in the beta range during isometric contractions in man (Conway et al., 2001; Kilner et al., 2000). This current was applied directly to the 17 cortical cells. In this study, we will refer to this band-pass filtered noise as the EEG beta drive. In addition to the common input which consists of the 10 nA DC current and the EEG beta drive, each neuron receives a neuron-specific Gaussian White Noise (GWN) with mean zero and standard deviation of 0.10 nA, which was directly applied (i.e., by current clamp) to the cortical cells. The Gaussian White Noise to different neurons is uncorrelated. With the ratio between common beta-drive (standard deviation 0.05 nA) and the neuron specific noise (standard deviation 0.10 nA) the common beta-drive is 20% of the total variable input power to the cortical cells. The mean firing rate of the cortical cells in response to the constant current, the beta-related input and the neuron specific noise is about 22 spikes/s. A TMS pulse tends to activate neurons in motor cortex directly by excitatory synaptic currents (Kaneko et al., 1996; Lazzaro et al., 1998). Therefore, we simulated the effect of a TMS pulse on the cells in motor cortex by a simultaneous post-synaptic current (see Eq. 5.2) in all cortical cells. The strength of the TMS pulse is represented by the maximum conductivity $\varepsilon$ (see Eqn. 5.23). The reversal potential for this excitatory synaptic current was set to 70 mV and the time constant to 0.2 ms (Table 1). TMS pulses were given randomly, i.e. uncorrelated with the band-pass filtered Gaussian White Noise, representing the common beta-drive to the neurons in motor cortex. The interval between successive TMS pulses was large ($> 300$ ms) to ensure that the pre-TMS epochs did not contain any contributions of responses related to a previous TMS pulse (see Fig. 5.8).

### 5.2.4 Cortico-spinal model

Following a TMS pulse applied over primary motor cortex, an EMG response in hand muscles occurs with an onset latency of about 23 ms (Rothwell et al., 1991). This total delay of 23 ms consists of a delay of 8 ms from primary motor cortex to spinal cord, an additional 14 ms for the conduction delay from spinal cord to the muscle, and a delay of 1 ms due to the synapses and dynamics of the cortical neurons, the $\alpha$-motoneurons, and neuromuscular transmission. Based on these data, we included a conduction delay $\tau_A$ of 8 ms in the projection from motor cortex to spinal cord and a time delay $\tau_B$ of 14 ms in the calculation of EMG from spinal cord activity.

### 5.2.5 Spinal cord and electromyographic activity

The surface EMG signal was constructed by convolution of the spike output of the population of all $\alpha$-motoneurons with the motor-unit action potential (MUAP). The shape of the MUAP was defined by the alpha function:

$$\alpha(t') = \frac{t'}{\tau_\alpha} \exp\left(\frac{-t'}{\tau_\alpha}\right) \tag{5.5}$$

for $t' \geq 0$ with $\tau_\alpha$ = 1.4 ms. The MUAP is given by $MUAP(t) = -\alpha(t)$ for $t \geq 0$ and $MUAP(t) = \alpha(-t)$ for $t < 0$.

The amplitude of the EMG signal is defined as $A(t) = \sqrt{x^2(t) + \tilde{x}^2(t)}$ with $\tilde{x}(t)$ the Hilbert transform of $x(t)$, defined by $\tilde{x}(t) = \int_{-\infty}^{\infty} \frac{x(\tau)}{t-\tau} d\tau$. To avoid confusion, $x(t)$ will be called the raw EMG signal and $A(t)$ the EMG amplitude signal. To prevent the effect of any initial conditions, the first 65 ms in each simulation were excluded from analysis.

### 5.2.6 Neuron model and data analysis

The cortico-spinal model was built using Neuron (version 6.0, www.neuron.yale.edu). All data-analyses were done using Matlab (Release 2008a, The Mathworks, Natick, USA).

In order to calculate the cortico-spinal coherence between the beta drive and EMG, these signals were divided in epochs of 819.1 ms. A multi-taper method was applied to reduce the variance of the spectral estimates in the EEG and EMG amplitude epochs (see Mitra and Pesaran, 1987). This method involves the multiplication of the signals in corresponding time epochs with multiple orthonormal data tapers before Fourier transformation. The windowed Fourier transform $X_k(f)$ of an epoch with the $k$-th taper is given by

$$X_k(f) = \sum_{m=1}^{M} w_{m,k} x_m \exp^{-2\pi i f m \Delta t} \tag{5.6}$$

where $w_{m,k}$ ($k$ = 0, 1, ..., $K$-1) are $K$ orthogonal taper functions. $x_m$ represents the discrete time series in the time epoch with $t = m\Delta t$ $(1 \leq m \leq M\ )$. In this study, a set of orthonormal sine tapers $w_{m,k}$ $(1 \leq m \leq M, 0 \leq k \leq K-1)$ is applied with the $k$-th taper defined by

$$w_{m,k} = \sqrt{\frac{2}{N+1}} \sin\left(\frac{(k+1)\pi m \Delta t}{N+1}\right) \tag{5.7}$$

The number of taper functions is given by $K = 2NW - 1$, where $N$ is the taper length in seconds (0.8191 s in this study) and $W$ the frequency bandwidth parameter in Hz. $W$ was set to 4 Hz to achieve a spectral concentration over about 4 Hz. With the taper length set to 819.1 ms, six taper functions were used.

The direct multitaper estimates for the auto-spectrum $S_{xx}(f)$ and cross-spectrum $S_{xy}(f)$ are given by

$$S_{xx}(f) = \frac{1}{K} \sum_{k=0}^{K-1} |X_k(f)|^2 \tag{5.8}$$

and

$$S_{xy}(f) = \frac{1}{K} \sum_{k=0}^{K-1} X_k(f) Y_k^*(f) \tag{5.9}$$

where $Y_k^*(f)$ represents the complex conjugate of $Y_k(f)$. The coherence $\gamma(f)$ between signals $x(t)$ and $y(t)$ is defined as the absolute value of the normalised cross-spectrum between the demeaned signals $x(t)$ and $y(t)$ in the frequency domain, averaged over trials:

$$\gamma(f) = \frac{|\langle S_{xy}(f)\rangle|}{\sqrt{\langle S_{xx}(f)\rangle\langle S_{yy}(f)\rangle}} \tag{5.10}$$

where $\langle . \rangle$ refers to the ensemble average. The coherence spectrum was computed from 500 paired epochs.

Significance was tested by randomly reshuffling the corresponding EEG and EMG amplitude data epochs and then calculating the average coherence spectrum. This procedure was repeated 100 times, thus providing 100 coherence spectra of uncorrelated data sets, which allowed us to calculate the confidence levels for uncorrelated data. Coherence values that were outside the 95% confidence level of the distribution of uncorrelated data were considered as significant. For a more detailed description of these analyses, see Schoffelen et al. (2005); Womelsdorf et al. (2007); van Elswijk et al. (2009).

### 5.2.7 Spectral analysis of pre-TMS epochs

The phase of oscillations at a particular frequency within motor cortex and spinal cord immediately before applying a TMS pulse (i.e. pre-TMS phase) was determined for all integer frequencies in the range between 10 and 70 Hz. For each frequency, EEG epochs with a length of two cycles prior to the time of a TMS pulse (i.e. pre-TMS epochs) were cut out of the pre-processed data, yielding 1000 epochs for each frequency. Next, a Hann window was applied to each epoch and the Fourier decomposition was computed, resulting in 1000 vectors in the complex plane, each with its own amplitude and phase.

To calculate the motor-evoked potential (MEP) amplitudes as a function of pre-TMS EEG or EMG phase, EMG epochs in the time interval between 0 and 100 ms after the onset of the TMS pulse (i.e. post-TMS EMG epochs which contain the MEP) were clustered as a function of the corresponding pre-TMS EEG or EMG phases for each integer frequency in the range between 10 and 70 Hz (i.e., the phase of a particular frequency in the corresponding EEG or EMG-signal in the time interval of 2 cycles of that frequency before the TMS pulse was applied). Therefore, 20 phase bins on the unit circle with their centres equally spaced between $-\pi$ and $\pi$ were defined for each frequency in the range between 10 and 70 Hz. For each of these 20 phase bins, the fifty pre-TMS EEG or EMG phases (out of the total number of 1000 phases) closest to the bin's centre phase were assigned to that phase bin. Note that this procedure implies that one pre-TMS EEG or EMG phase could be

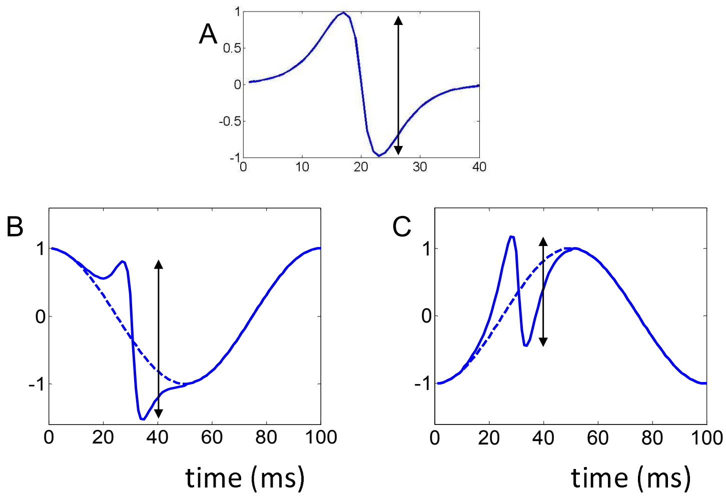

Figure 5.2: The effect of superposition of a MEP-template (upper panel) on a sinusoid at different phases of the sinusoid. (A) shows the MEP-template with a peak-peak amplitude of 2 (arbitrary units). Linear addition of this MEP to a sinusoid gives a larger peak-peak amplitude when added to the decaying slope of the sinusoid (B) and a smaller peak-peak amplitude when the MEP is added to the rising phase of the sinusoid (C).

assigned to more than one phase bin. Next, these 50 pre-TMS EEG or EMG phases and the corresponding post-TMS EMG epochs were averaged for each bin. The MEP amplitude as a function of phase was defined as the peak-to-peak amplitude of the averaged post-TMS EMG epochs in each phase bin.

A proper interpretation of the phase-dependent amplitude modulation of the MEP requires a careful analysis since the peak-peak amplitude of the MEP may be affected by ascending or descending phases of the EMG signal. This is illustrated in Figure 5.2 where we have a typical MEP (panel A), linearly added to a sinusoid (panels B and C). Depending on the phase of the sinusoid, where the MEP is added, the peak-peak amplitude is larger (when the MEP is added on the negative slope, panel B) or smaller (when it is added on the positive slope, panel C) than that of the MEP itself. This can be easily understood from the following. If the signal for the MUAP is given by $f(t) = MUAP(t)$, the peak-peak amplitude can be easily determined by the difference of amplitudes at maximum and minimum of $f(t)$, i.e. at the times when $\frac{df(t)}{dt} = \frac{dMUAP(t)}{dt} = 0$. When the MUAP is superimposed on a sinusoid with amplitude $A$ and frequency $\omega$, the maximum and minimum of the function $f(t) = MUAP(t) + A\sin(\omega t + \varphi)$ are found by solving $\frac{df(t)}{dt} = \frac{dMUAP(t)}{dt} + A\omega\cos(\omega t + \varphi) = 0$. The times, when this derivative is zero, as well as the difference of the values of $f(t)$ at these times, depend on the phase in the sinusoid and on the frequency of the sinusoid. In order to correct the phase-dependent MEP-amplitude for this phase-dependent effect of EMG on the peak-peak amplitude of the MEP, we used the following procedure, which was similar to that used by van Elswijk et al. (2009). First we determined the averaged MEP by averaging all MEP responses, irrespective of the pre-TMS phase in EMG. This average was used as a template. We then determined for each frequency component the amplitude and phase of that frequency component in EMG in the time interval corresponding to two cycles of that frequency. We then added the template MEP to the extrapolated frequency component of that pre-TMS EMG signal and determined the peak-peak amplitude of the resulting MEP. This predicted peak-peak value was subtracted from the measured peak-peak amplitude for that particular frequency and phase in the pre-TMS EMG. If the phase of a frequency in the pre-TMS EMG is not relevant for the MEP amplitude, the difference between measured MEP and predicted MEP should scatter around the value zero for all phases of that frequency component. However, if the MEP amplitude is modulated by the phase of ongoing oscillations, this difference should be periodic. Therefore, the relation between pre-TMS phase of EMG and the difference between measured and predicted post-TMS MEP amplitude was quantified by a least-squares fit of a cosine function with the phase unconstrained. Cosine-fits with unconstrained phases have amplitudes with a positive bias. This bias was estimated by randomly reshuffling pre-TMS phases versus post-TMS MEP amplitudes, followed by the analysis described above (i.e. phase binning and cosine fitting). This randomisation was repeated 100 times for each frequency and for each signal (EEG and EMG amplitude) to provide a criterion for significance.

## 5.3 Results

Figure 5.3 shows the main characteristics of the beta drive and EMG signals without applying TMS. Fig. 5.3A shows the power spectral density of the beta drive, which was constructed by filtering Gaussian White Noise (GWN) with a band-pass filter with a peak frequency at 20 Hz. Figure 5.3B shows the spectral properties of the EMG (i.e., the convolution of the population activity of the cells in the spinal cord with the MUAP). Figure 5.3C shows the coherence between beta drive and EMG. The grey area in Figure 5.3C represents the 95% significance level, which was obtained by calculating the coherence between the beta drive and EMG after

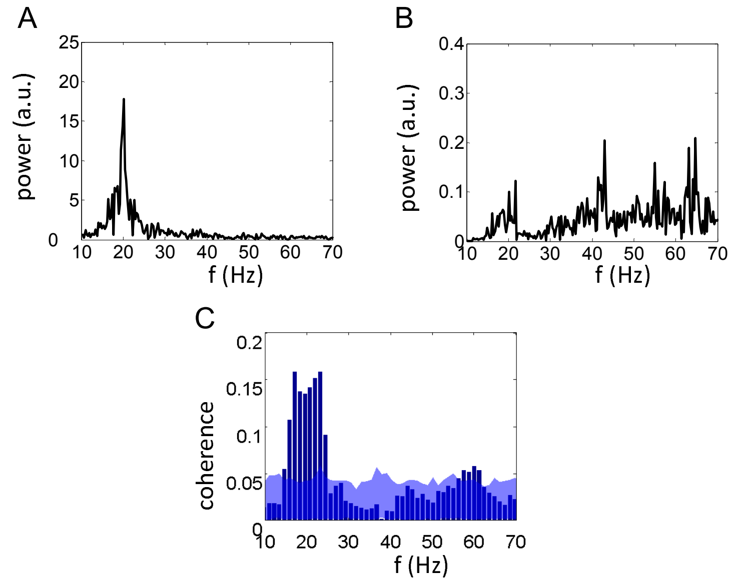

Figure 5.3: Power spectrum of the common beta drive (in arbitrary units; panel A), the power spectrum of the EMG signal (B) and coherence between beta drive and EMG signal as a function of frequency (C) for the model without TMS pulses. The grey area in the bottom panels represents the 95% confidence interval, obtained by calculating the coherence between beta drive and EMG after random permutation of corresponding segments of the beta drive and EMG signals.

random permutation of the corresponding segments of the beta drive and EMG signals. The coherence deviates significantly from chance level in the region between 15 and 25 Hz, in agreement with the experimental results in Kilner et al. (2000) and van Elswijk et al. (2009). The significant coherence in the range between 15 and 25 Hz illustrates that the beta drive, which is small relative to the constant input and the noise input to each cell in motor cortex, has an impact on the activity of the motoneurons in the spinal cord.

Figure 5.3A shows the spectrum of the beta drive. Please note that this beta drive represents only 20% of the total variable input to the cells in motor cortex as the power of the neuron-specific input, which is uncorrelated between neuron, is 4 times larger. Moreover, there is a large constant input to the cells in motor cortex to ensure a constant firing rate near 20 Hz. Fig. 5.3B show the spectrum of the EMG. These spectra show that EMG has a significant power near 20 Hz, which is

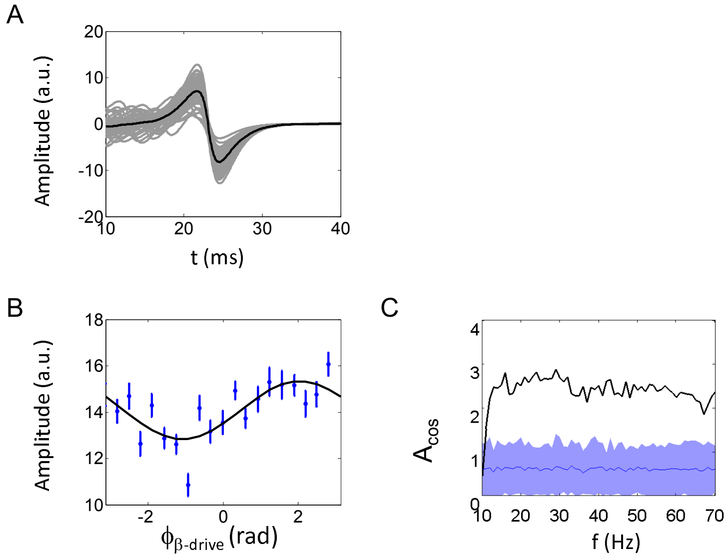

Figure 5.4: The Motor Evoked Potentials (MEPs) induced by simulated TMS pulses to cortex. (A) shows the simulated MEPs for TMS pulses applied at the pre-TMS phase of approximately 2.2 radians of the 20 Hz component in the beta drive. The grey lines represent the separate MEP responses to 50 simulated TMS pulses. The black solid line represents the average of all MEPs. (B) shows the mean peak-peak amplitude of the simulated MEP for each of 20 pre-TMS phases (at 0, $\pi/10$, $2\pi/10$, $3\pi/10$ …, 2 $\pi$) in the 20 Hz component of the beta drive. Bars represent standard deviation in the amplitude values. (C) shows the amplitude of the cosine fit to the data in (B) as a function of frequency. The grey area represents the 95% confidence level obtained by assigning a new randomly chosen pre-TMS phase in the interval $[0, 2\pi]$ to each MEP averaged over the nearest 50 phases.

caused by the beta-modulated drive from motor cortex and these frequencies in the beta drive are coherent with the beta drive in motor cortex (Fig. 5.3C). This will be explained later in more detail.

Figure 5.4 shows the Motor Evoked Potentials (MEPs) induced by simulated TMS pulses in cortex. Figure 5.4A shows a number of 50 simulated MEPs (grey lines) generated when the TMS pulse was given at a phase of approximately 2.2 radians in the 20 Hz cycle of the pre-TMS EEG. In agreement with previous reports

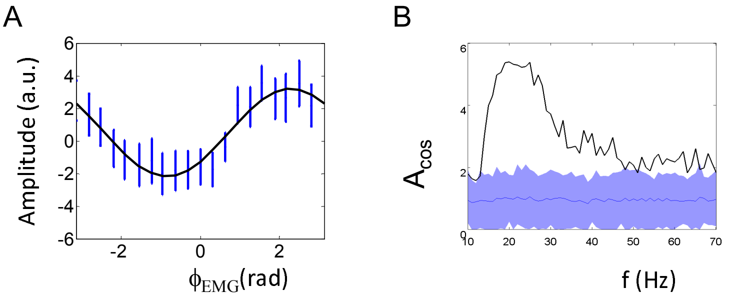

Figure 5.5: (A) shows the mean peak-peak amplitude of the difference of the simulated and predicted MEP for each of 20 pre-TMS phases (at 0, $\pi/10$, 2 $\pi/10$, 3 $\pi/10$, …, $2\pi$ ) in the 20 Hz component of the EMG. Bars represent standard deviation in the amplitude values. The solid line shows the cosine fit to the data. (B) shows the amplitude of the cosine fit to the data in A as a function of frequency. The grey area represents the 95% confidence level obtained by assigning a new randomly chosen pre-TMS phase in the interval $[0, 2\pi]$ to each MEP averaged over the nearest 50 phases.

(Amassian et al., 1989; Kiers et al., 1993; van der Kamp et al., 1996; Ellaway et al., 1998) there is a large variability in MEP amplitudes. The black solid line represents the average of all MEPs. Figure 5.4B shows the mean MEP amplitudes elicited by TMS pulses as a function of the phase in the 20 Hz component of the EEG, when the TMS was applied. The solid line is a cosine fit to the data. Similar analyses were done for all frequencies. The amplitude of the cosine fit for each frequency is shown in Figure 5.4C. The phase-dependent modulation was small but appeared to be significantly different from chance level (grey area, indicating the 95% confidence range) for most frequencies.

Figure 5.5A shows the peak-peak amplitude of the difference between the simulated and predicted MEP amplitude for various phases of the pre-TMS 20 Hz component in EMG. A cosine fit to the data revealed a significant cosine modulation with the phase of the 20 Hz component in the pre-TMS EMG. Figure 5.5B shows the phase-dependent modulation of the MEP-amplitude for all frequencies. The MEP amplitude was significantly dependent on phase in the frequency range between 15 and 40 Hz, in agreement with experimental data (van Elswijk et al., 2009).

In order to obtain a better understanding of the dependency of the MEP amplitude on the phase in pre-TMS EEG and EMG, we have analysed the firing charac-

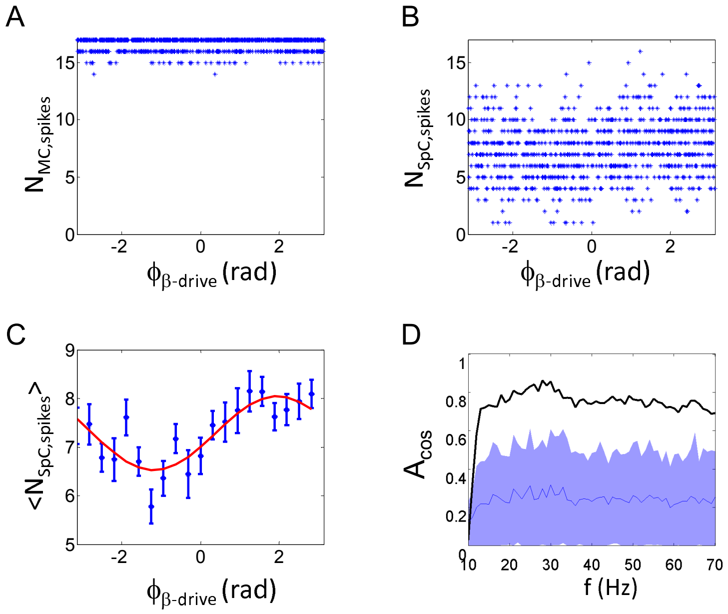

Figure 5.6: (A) shows the number of action potentials in the population neurons in motor cortex in response to a TMS pulse in various phases of the pre-TMS 20 Hz cycle in the beta drive. Each dot represents the response to a single TMS pulse. (B) shows the number of action potentials in the population of $\alpha$-motoneurons in the spinal cord in response to a TMS pulse in various phases of the pre-TMS 20 Hz cycle in the beta drive. (C) shows the mean number of spikes (dots) and standard deviation (bars) as a function of phase of the pre-TMS 20 Hz cycle in the beta drive. The solid line shows the result of a cosine fit to the data. (D) shows the amplitude of the cosine fit (as in C) as a function of frequency in pre-TMS beta drive.

teristics of the neurons in motor cortex and spinal cord after a TMS pulse, implemented by a synaptic current with maximum conductance 5 mS to the neurons in motor cortex. The TMS pulses elicited action potentials in almost all (range 15-17) cortical cells, irrespective of the phase of the pre-TMS beta drive. This is illustrated in Figure 5.6A, which shows the number of action potentials in the population of 17 neurons of motor cortex in the interval of 1 *ms* after a TMS pulse as a function of the phase in the 20 Hz component of the pre-TMS beta drive. Figure 5.6A shows the responses to 976 TMS pulses. Most TMS pulses activate all 17 neurons in motor cortex. In about 15% of the responses, only 16 or 15 spikes were generated by the TMS pulse. There was no significant correlation between the number of action potentials after the TMS pulse and the phase of the pre-TMS beta drive. In order to investigate whether these results might have been due to the strength of the TMS pulse we have repeated the simulations for a smaller current pulse (2 mS instead of 5 mS). For this current pulse the average number of spikes in response to this TMS pulse was 13 spikes, with a small but significant phase-dependent modulation of (on average) 0.5 spikes. These simulations show that the number of spikes in motor cortex in response to a TMS pulse was only slightly modulated by the phase of the beta drive (results not shown).

Figure 5.6B shows the number of action potentials in the population of motoneurons in the spinal cord in the interval between 8.5 and 9.5 ms after a TMS pulse (5 mS current pulse) as a function of the pre-TMS phase of the 20 Hz component of the beta drive. Whereas almost all cells in motor cortex do respond to the TMS pulse (Fig. 5.6A), only half of the $\alpha$-motoneurons in the spinal cord respond to a TMS pulse (Fig. 5.6B). On average each TMS pulse elicits about 8 spikes in the 17 $\alpha$-motoneurons. There is a small modulation in the number of action potentials as a function of phase, which becomes more evident if we plot the average number of action potentials in the pool of $\alpha$-motoneurons as a function of pre-TMS phase of the 20 Hz component in the beta drive (Figure 5.6C). A cosine fit gave a significant modulation of the number of action potentials in the pool of $\alpha$-motoneurons as a function of pre-TMS beta drive. This result illustrates that the phase of the TMS pulse in the beta drive does have a significant effect on the spike output of the pool of $\alpha$-motoneurons. Figure 5.6D shows the amplitude of the cosine fit as a function of frequency in the pre-TMS beta drive. A statistical analysis of the cosine fit revealed a small but significant ($p < 0.05$) modulation for all frequencies.

Figure 5.7 shows the same results for the responses of motoneurons in the spinal cord to TMS pulses, but now as a function of phase and frequency in the pre-TMS EMG, instead of pre-TMS beta drive. Figure 5.7A shows the distribution of the number of action potentials in the population of $\alpha$-motoneurons in response to 976 TMS pulses in various phases of the 20 Hz cycle in EMG preceding the TMS pulse. These results show a clear modulation in the number of action potentials in the pool of $\alpha$-motoneurons. This becomes more evident when we plot the average number of action potentials as a function of phase in the 20 Hz component of pre-TMS EMG (Figure 5.7B). The amplitude of a cosine fit to the average number of spikes as a function of phase (Figure 5.7B) is 1.34 spikes, which appeared to be significantly different from zero. Similar results were obtained for all frequencies in the range between 15 and 40 Hz (see Figure 5.7C). The main result from Figures 5.6 and 5.7 is that a TMS pulse elicits hardly any changes in the number of action potentials in the cells in motor cortex as a function of phase of the pre-TMS beta drive. However, the same TMS pulse induces a significant modulation of the number of action potentials in the pool of $\alpha$-motoneurons as a function of phase of pre-TMS-beta

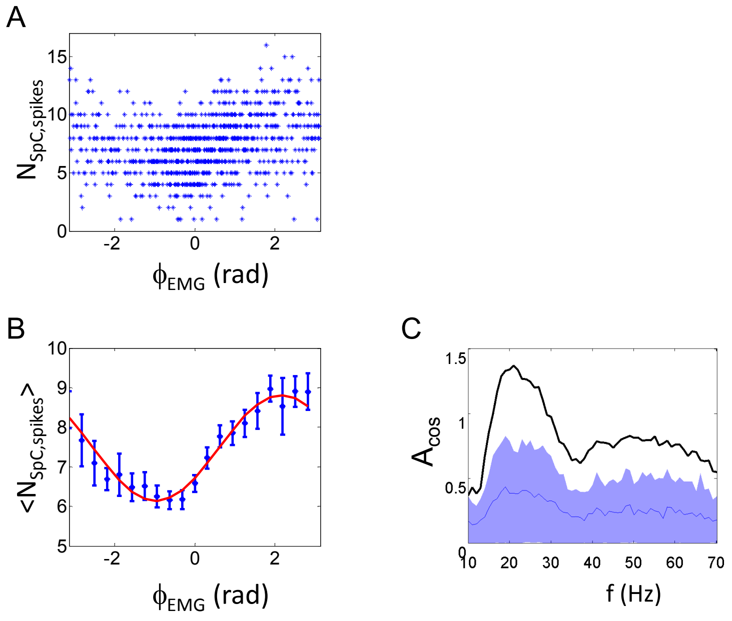

Figure 5.7: The number of action potentials in the population of $\alpha$-motoneurons in response to a TMS pulse for various phases of the pre-TMS 20 Hz cycle in EMG. Each dot in (A) represents the number of spikes in the pool of 17 $\alpha$-motoneurons for a TMS pulse applied at that particular phase of pre-TMS EMG. (B) shows the average number of spikes in the population of $\alpha$-motoneurons as a function of pre-TMS phase of the 20 $Hz$ component in EMG in 20 equally large phase bins. Bars represent the standard deviation. The solid line shows the result of a cosine fit to the data. (C) shows the amplitude of the cosine fit (shown in B) as a function of frequency in pre-TMS EMG.

drive. This modulation is even larger, if we plot the number of spikes elicited by a TMS pulse as a function of phase of pre-TMS EMG.

The results in Figures 5.6 and 5.7 and the results of Figures 5.4 and 5.5, which show that the phase-dependency of the MEP-amplitude is different for EEG and EMG, could be attributed to various components of the cortico-spinal model. The result that the MEP amplitude hardly depends on the phase of the beta drive, but does depend on EMG phase, might be explained by the fact that a TMS pulse to the cells in motor cortex activates almost all neurons in motor cortex. The coupling from motor cortex to spinal cord is much weaker, resulting in much less spikes in-

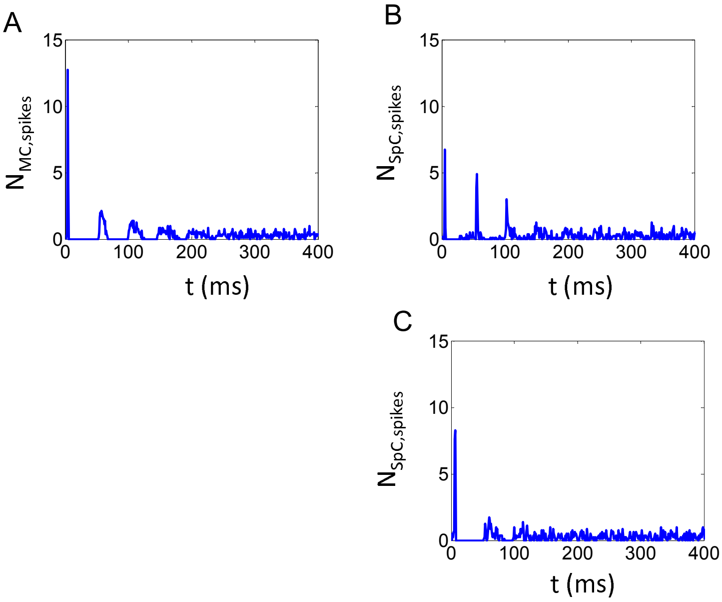

Figure 5.8: (A) and (B) show averaged responses of the population of cells in motor cortex (A) and spinal cord (B) to TMS pulses. Each TMS pulse triggers a sequence of volleys in the population of cells in motor cortex, which is reflected in a series of bursts in the pool of $\alpha$-motoneurons. (C) shows the average activity in the $\alpha$-motoneurons after a single volley of 15 spikes to each cell. All data show averages of 8 responses.

duced in the pool of $\alpha$-motoneurons. Another explanation might be that the TMS pulse to the cells in motor cortex was given before the effect of the previous TMS pulse had vanished. As mentioned before a TMS pulse activates almost all neurons in motor cortex and thereby synchronises the motor neurons in motor cortex. Since all cortical cells have similar firing rates, synchronisation of neuronal firing in motor cortex by a TMS pulse could elicit a series of synchronised volleys of spikes in motor cortex. This is shown in Fig. 5.8A, which shows the average response (i.e. averaged response to 8 TMS pulses) of the population of motocortical cells. These synchronised volleys in motor cortex drive the $\alpha$-motoneurons, leading to a decaying series of volleys in $\alpha$-motoneurons. This is illustrated in Figure 5.8B, which shows the average response of the population of $\alpha$-motoneurons to TMS pulses. In order to distinguish between the direct effect of the TMS pulse on the

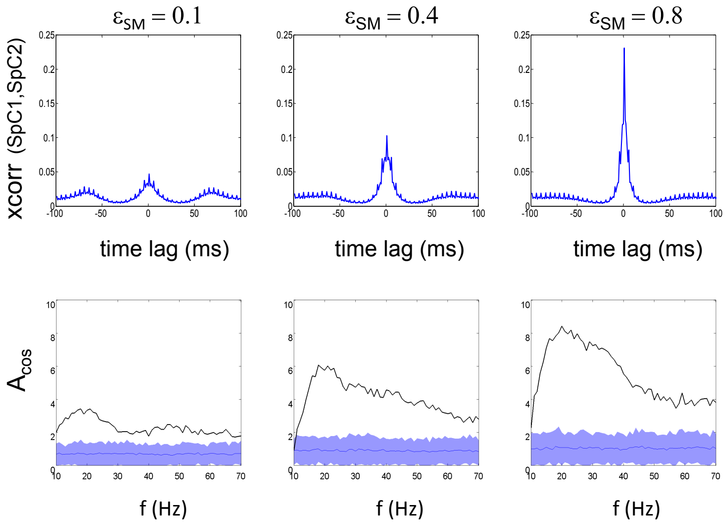

Figure 5.9: Upper row shows the cross correlation between the ongoing spike activity (without the TMS effect) of two spinal cord subpopulations (even and odd numbered subpopulations) for different coupling strengths $\varepsilon_{SM}$. The bottom row shows the corresponding corrected amplitude of the cosine fit as a function of frequency in pre-TMS EMG for different coupling strengths $\varepsilon_{SM}$ .

activity of $\alpha$-motoneurons and the indirect effect of synchronisation of MC cells on $\alpha$-motoneurons, we have simulated a single volley of 15 spikes from MC to all $\alpha$-motoneurons at random phases of the EMG beta-cycle. The average response to such a single volley is illustrated in Figure 5.8C. This single input volley of 15 spikes generates one volley of activity in spinal cord, which desynchronises rapidly due to the different firing rates of the $\alpha$-motoneurons (8-21 spikes per second) in agreement with previous experimental studies (Mills and Schubert, 1995; Kleine et al., 2000). Notice that the synchronised volleys in the population of cells in motor cortex decay gradually until they have disappeared after about 250 ms. This implies that the interval between the TMS pulses in the study by Mitchell et al. (2007) (>5 s), in the study by van Elswijk et al. (2009) (>3.5 s) and in our simulations (>300 ms) should be longer than this interval of 250 ms. Therefore, the modulation of the MEP as a function of phase of pre-TMS EMG cannot be explained by long lasting synchronisation of EMG by TMS-induced volleys in motor cortex.

Increasing the coupling strength between motor cortex and spinal cord not only increases the synchronisation of activity within the spinal cord, but also increases the strength of the ’TMS’-induced spike-volley input to the $\alpha$-motoneurons in spinal cord. In order to separate these effects, we changed the model slightly. In stead of applying a TMS pulse to the motor cortex and inducing synchronised volleys for a short period, we simulated the effect of a TMS pulse on the $\alpha$-motoneurons in the spinal cord by a spike to all $\alpha$-motoneurons on a synapse with a constant maximum conductance strength ($\varepsilon_{TMS} = 0.4\ \mu$S). Before simulating the effect of a TMS pulse on the $\alpha$-motoneurons in the spinal cord, we determined the synchronisation of the ongoing activity within the spinal cord. In order to quantify this synchronisation, we divided the activity in the population of $\alpha$-motoneurons in two subpopulations (a subpopulation of the odd numbered $\alpha$-motoneurons (SpC1) and a subpopulation of the even numbered $\alpha$-motoneurons (SpC2)) and determined the normalised cross correlation between the activity of the two subpopulation activities (without TMS effects) for three different coupling strengths between motor cortex and spinal cord ($\varepsilon_{SM}$) (upper row of Fig. 5.9). A stronger coupling between motor cortex and spinal cord caused a higher cross correlation between the two subpopulations in spinal cord. Knowing this, we investigated the effect of a TMS pulse (implemented by a spike to all $\alpha$-motoneurons, see above) as a function of this increased synchronisation and observed that the modulation depth of the phase-dependent TMS response in the EMG (MEP-amplitude) increased for increasing coupling strengths as is shown in the bottom row of Fig. 5.9 as a function of the frequency in pre-TMS EMG. From these results we conclude that an increase in periodic synchronised firing of the $\alpha$-motoneurons activity causes a possibly larger possible flexibility ($A_{cos}$) in neuronal communication.

## 5.4 Discussion

The main result of this study is that the amplitude of the MEP depends on the phase of the pre-TMS EMG in the frequency range between 15 and 35 Hz with a peak around 20 Hz (Figure 5.5), in agreement with previous experimental observations (Mitchell et al., 2007; van Elswijk et al., 2009). The amplitude of the MEP in our simulations is also modulated by the phase of the pre-TMS beta-rhythm (Figure 5.4B), but much less than by the pre-TMS EMG. Presumably, the modulation of MEP-amplitude as a function of pre-TMS phase EEG is too small to become significant in the experimental studies (Mitchell et al., 2007; van Elswijk et al., 2009). The present study shows that the phase of rhythmic activity in the receiving population determines the effectiveness of information transfer.

The ’CTC’-hypothesis postulates that the effectiveness of information transfer between two neuronal populations is determined by the phase difference between the peaks in excitability of those populations. The idea is that the sending population generates a spike volley at the time when its excitability is maximal and that this 'information package' arrives after some time $\tau$ at the receiving population. If the excitability of the receiving population is high at the arrival time of the 'information package', then the receiving population is supposed to respond with a high population activity, whereas the response to the 'information package' is small when it arrives at the trough of the excitability of the receiving population. The effect of neuronal volleys with a constant amplitude (i.e. a constant number of spikes) to spinal motoneurons, was shown in the bottom row of Fig. 5.9: the MEP amplitude (induced by TMS) depends on the phase of the pre-TMS EMG. Applying a TMS pulse to the neurons in motor cortex in our model showed that almost all neurons in motor cortex respond with a spike to the TMS-pulse (Fig. 5.6A). The number of spikes in the responses of the $\alpha$-motoneurons in the spinal cord to these 'information packages' and the MEP amplitudes depend on the phase of the pre-TMS EMG (Fig. 5.7B and Fig.5.5B). The latter result is in agreement with the experimental findings of van Elswijk et al. (2009), who showed that the difference in simulated and predicted MEP amplitudes depends on the pre-TMS EMG phase for the 15 - 35 Hz oscillations.

The number of action potentials in the pool of motocortical cells in response to a TMS pulse is hardly modulated as a function of phase of the beta rhythm (Fig. 5.6A). However, the number of action potentials in the population of $\alpha$-motoneurons is significantly modulated as a function of pre-TMS beta rhythm (Fig. 5.6B, C). The modulation of the number of action potentials in the population of $\alpha$-motoneurons as a function of phase of the pre-TMS EMG is significant in the frequency range between 15 and 35 Hz and is much larger than that relative to phase of the pre-TMS beta rhythm (Figs. 5.6 and 5.7). The experimental result obtained in the study by van Elswijk et al. (2009) did not show a significant modulation as a function of the phase of pre-TMS EEG. This discrepancy might be explained by the fact that the dependency of phase of pre-TMS beta rhythm is rather small and by the fact that for strong TMS pulses it is also possible to produce direct activation of cortico-spinal axons (Lazzaro et al., 1998). Mitchell et al. (2007) proposed another two possible explanations for the fact that the amplitude of MEP responses is related to the pre-TMS phase of EMG oscillations but not to pre-TMS EEG. Firstly, they postulate that only oscillations within the $\alpha$-motoneuron pool are relevant for the prediction of the MEP amplitude. In that case, EMG oscillations corresponding to modulations of $\alpha$-motoneuron excitability predict the phase dependent response of $\alpha$-motoneurons to the descending corticospinal volleys. Additionally, Mitchell et al. (2007) postulated a second mechanism related to the coherence between EMG and EEG rhythms. In their view, EMG oscillations might act as a surrogate measure of the oscillatory network state in motor cortex. Since EMG oscillations would relate only to that part of the motor cortex network that projects to the target muscle, and since EEG reflects the average activation over a wide and (possibly) functionally heterogeneous area of motor cortex, EMG could be more effective in predicting the MEP amplitude than EEG. Our results provide support to the first explanation proposed by Mitchell et al. (2007). In our simulations the TMS pulse elicits a constant number of spikes in motor cortex, i.e. the output of the motor cortex does not depend on the pre-TMS phase of the beta drive. Our results reveal a clear dependence of MEP amplitude with the phase of pre-TMS EMG. Since beta drive and EMG are weakly correlated (see Fig. 5.3C), the MEP amplitude and pre-TMS beta drive may be indirectly correlated by the coherence between beta drive and EMG. Since the coherence between beta drive and EMG is weak (about 0.1), the correlation between MEP amplitude and phase of pre-TMS beta drive is much smaller than that with phase of pre-TMS EMG. Presumably the correlation between MEP-amplitude and phase of pre-TMS EEG is too small to be significant in experimental studies.

The phase-dependent modulation of the output of the cells in motor cortex in response to a TMS pulse, is rather small or absent (Fig. 5.6A). All results shown are simulation results for a TMS pulse whose strength was given by the maximum value of the synaptic conductance of $\varepsilon$ of 5 $\mu$S. In that condition the TMS pulses saturate the neurons in the motor cortex: for most simulated TMS pulses, all neurons in motor cortex become active. Simulations with a weaker TMS pulse ($\varepsilon = 2$ $\mu$S and also $\varepsilon = 0.4$ $\mu$S , results not shown) revealed a weak modulation as a function of the phase of the beta drive, suggesting that the motoneurons in the motor cortex are also sensitive to the timing of (synchronised) input in the beta rhythm. This dependence is most likely only weak since the common beta-drive makes only 20% of the total variable input.

One of the complications in understanding cortico-spinal coherence is the close overlap of the frequencies of the beta-rhythm (from about 15 to 25 Hz) and the firing rates of neurons in motor cortex and spinal cord. The coherence between firing rate and local field potential in motor cortex is weak (Baker et al., 2003). In our model, the common beta-drive to the cells in motor cortex is only 20% of the variable input, which explains why cells in motor cortex reveal a weak coupling to the beta drive. Since the coherence between firing rate in motor cortex and local field potential is weak, the majority of neurons in motor cortex is not firing in synchrony. However, a TMS pulse synchronises the firing of neurons in motor cortex and thereby induces a 20 Hz series of spike volleys to the spinal cord, not because of the beta rhythm, but because of the mean firing rate of 20 Hz of cells in motor cortex. This 20 Hz rhythm induces 20 Hz oscillations in EMG.

Simulations with different peak frequencies (15 and 25 Hz) of the beta drive showed similar results with only a slightly decreased maximum value for the amplitude of the cosine fit ($A_{cos}$) of the MEP amplitude as a function of the pre-TMS EMG phase (results not shown). Simulations with a different average firing rate for the neurons in motor cortex (30 spikes/s) showed a decrease in peak value of $A_{cos}$ at 20 Hz (results not shown). This shows that in our corticospinal model the firing rate of the motor cortex plays an important role in the flexibility of information transfer between motor cortex and spinal cord.

The CTC-hypothesis postulates that the sending population, i.e., the motor cortex in our corticospinal model, generates a spike volley at the time that its excitability is maximal. In our model and in the experiments described by van Elswijk et al. (2009), the TMS pulses are presented at random times within the excitability cycle. At any phase almost all neurons in motor cortex respond. This allowed us to investigate the effect of the phase of the ongoing EMG on the MEP amplitude. However, this did not allow to test to what extent the coherence between the sending and the receiving populations determines the communication efficiency. Figure 5.8A shows that a TMS pulse synchronises the neurons in motor cortex. This synchronisation then leads to series of gradually decaying volleys with intervals of about 50 ms, related to the 20 Hz firing of neurons in motor cortex. These volleys then activate the $\alpha$-motoneurons in spinal cord causing coherent activity in spinal cord and motor cortex for a short period ($<$ 250 ms). Figure 5.8B shows that a considerable number of $\alpha$-motoneurons respond to the second and even third volley from the motor cortex. This result suggests that if the excitability of the sending and receiving population is coherent and optimal adjusted to each other, like in our computer simulations after a TMS-pulse to motor cortex, the two populations can communicate efficiently during this period of coherent activity.

The main conclusions from this study can be summarised as follows. The phase of the ongoing rhythmic activity in spinal cord modulates the efficiency of the transfer of information to the spinal cord. The modulation depth of the information transfer depends on the amount of correlated activity within the pool of $\alpha$-motoneurons.

### 5.4.1 Properties of the corticospinal model

One could argue that the results of this study may critically depend on the assumptions and on the choice of some parameter values in the model.

Our model had feedforward projections from cortex to spinal cord and did not have feedback connections. In order to incorporate possible feedback projections from spinal cord to motor cortex, we had extended the model with feedback connections from all motoneurons in the spinal cord to all neurons in the motor cortex. Since the motor cortex is driving the spinal cord and not the other way around, the synaptic coupling from motor cortex to spinal cord is most likely significantly stronger than the feedback projections. We set the strength of the feedback connection to 0.25 $\varepsilon_{SM}$. The coherence between the beta drive and the EMG signal for the model with feedback connections (result not shown) was similar to the coherence of the forward model. This is in agreement with predictions by several theoretical studies on pulse-coupled oscillators with time delay in the coupling (Ernst et al., 1995, 1998; Zeitler et al., 2009). In particular, the study by Zeitler et al. (2009) on synchronisation between pulse-coupled oscillators with *asymmetric* coupling and time delays, shows that the two stable states for symmetric coupling merge to a single stable state when the strength of coupling from population $A$ to $B$ is significantly stronger than the coupling strength from $B$ to $A$. This implies that if one coupling strength is sufficiently larger than the other, the population of neurons with the stronger synaptic connections drives the other population. Moreover, the time delay of the synchronised activity between two coupled oscillators converges to a single stable state, where the precise value of the phase delay does no longer depend on the precise value of the two coupling strengths.

An important aspect of the model concerns the common beta-drive to the neurons in motor cortex. This common input in the beta range to the neurons in motor cortex was relatively small in this study. The precise strength was chosen based on the finding that the common input to cells in motor cortex is approximately 20% of the total input to each cell. In monkey, neurons in motor cortex synchronise to local oscillations in the beta band around 20 Hz Baker et al. (2003), which is close to the mean firing rate of pyramidal tract cells (Baker et al., 2001; Davies et al., 2006; Witham and Baker, 2007). This synchronisation is weak (typical coherence values between spike firing and LFP less than 0.05, Baker et al. (2003)). Since the coherence between the beta drive and EMG in this study agrees quite well with the coherence obtained in previous experimental studies (van Elswijk et al., 2009), we feel confident that both the amplitude of the common beta drive as well as the frequency band of the beta drive are well chosen.

Another important aspect of the model concerns the implementation of the TMS pulse. It is well known that TMS affects the responses of neurons in motor cortex by direct and indirect activation (Day et al., 1987; Edgley et al., 1990). In Mitchell et al. (2007) who used both electrical stimulation (TES) and magnetic stimulation (TMS), muscle responses elicited by TES have slightly shorter latencies than TMS, suggesting that TMS is mediated more by indirect stimulation of motor cortex neurons.

The other aspect of the TMS pulse concerns the strength of this pulse, which was implemented by a synaptic current, modelled by a alpha-function with a maximum conductance of 5 $\mu$S. For this strength of TMS pulse, analysis revealed that the MEP amplitude was modulated by the pre-TMS beta rhythm. Simulations with a smaller pulse of 2 $\mu$S gave very similar results as for 5 $\mu$S. Therefore, the results of this study do not critically depend on the strength of the TMS pulse.

The strength of the projections from motor cortex to spinal cord was chosen to meet some physiological criteria. First of all, the projections should produce a coherence of about 0.1 between beta drive and EMG in the 15-30 Hz frequency band for isometric contractions, in agreement with previous observations (Kilner et al., 2000; Schoffelen et al., 2005). Second, the strength of the projections should be such that a TMS pulse may activate a large fraction of the neurons in the motor cortex, but should not activate all $\alpha$-motoneurons. A third requirement was that the firing of motor-units during an isometric contraction is weakly correlated (Datta et al., 1991; Bremner et al., 1991). In our simulations, the correlation between neurons in the spinal cord was typically 0.1, which is in good agreement with experimental data by Datta et al. (1991) and Bremner et al. (1991).

### 5.4.2 Implications for neuronal communication

One of the major problems in understanding neuronal information processing is related to the question how groups of neurons interact with each other and how neurons participate in a flexible way in various ensembles depending on the stimulus or intention of the subject. This problem was revived by experiments on selective attention. In this paradigm, neurons can respond very differently to the same physical stimulus (Reynolds et al., 1999). Therefore, it was speculated that the different neuronal responses reflect a cognitive control over the routing of information from sensory to motor areas. Conceptually, the effect of cognitive top-down control implies a modification in the communication structure between brain areas. Fries (2005) speculated that this top-down control is mechanistically implemented by a pattern of coherent firing among neuronal groups by phase-locking among oscillations in the communicating neuronal groups, called the communication-through-coherence (CTC) hypothesis. Specifically, he hypothesised that neuronal communication between two neuronal groups mechanistically depends on coherence between them and the absence of neuronal coherence prevents communication. This requires that activated neuronal groups have the intrinsic property to oscillate and that those oscillations constitute rhythmic modulations in neuronal excitability that affect both the likelihood of spike output and the sensitivity to synaptic input. Thereby, rhythmic excitability peaks constitute rhythmically reoccurring temporal windows for communication.

One of the aims of this study was to test the CTC-hypothesis by modelling the coherent oscillations in EEG and EMG in the beta band. The results of this study are the first simulation results that replicate the main predictions of the CTC-hypothesis. However, they also point to some caveats in interpreting experimental data in the context of the CTC-hypothesis. First of all, we show that simply adding neuronal activity (in our case the MUAP) on top of sinusoidally modulated neuronal activity gives rise to modulations of the size of this neuronal activity (MUAP). However, this reflects just linear addition and does not imply a(non-linear) modulation of information flow. Secondly, our results show that it is truly the interaction between the rhythmic activity of two neuronal populations that is responsible for a selective modulation of transfer of neuronal information.

The results of this in silico study provide strong support to the CTC-hypothesis proposed by Fries (2005). This hypothesis assumes that modulations in excitability in a population of neurons provide gating windows for input to that population and thereby provide a modulation of effective transmission of neuronal activity from one population to the other. Therefore, the CTC-hypothesis predicts a phase-dependent modulation of the MEP. This is indeed what our simulations have shown. The result of our simulations is the first computational result which supports the CTC-hypothesis and which shows how the CTC-hypothesis is implemented in neuronal interactions.

The basic principles, that underlie the results of this study, are equally well applicable to other frequencies of rhythmic neuronal oscillations, such as in the gamma rhythms in the visual cortex as reported by Womelsdorf et al. (2007), in the alpha rhythms in visual and auditory cortex (for an overvieuw see the introduction of Kruglikov and Schiff, 2003), and in the alpha and mu rhythm as reported recently by Mazaheri et al. (2009). Therefore, we believe that the phenomenon explained in this paper has a general applicability to many neuronal systems that interact by synchronisation (see also Womelsdorf and Fries, 2007).

## Acknowledgement

This project was funded by the Netherlands Organisation for Scientific Research (NWO 051.02.050)

## Appendix

The motoneuron is modelled as the equivalent of an electric circuit, in which the cell's membrane (i.e. the lipid bilayer) is represented as a capacitance $C_m$. The voltage-gated ion channels are represented by nonlinear electrical conductances $G$, which are time and voltage-dependent. Leak channels are represented by linear leak conductances $G_L$. The time derivative of the potential across the membrane $V_m$ is proportional to the sum of the membrane currents and is given by

$$C_m \frac{dV_m}{dt} = -G_{Na}(V_m - E_{Na}) - (G_{K,fast} - G_{K,slow})(V_m - E_K) - G_L((V_m - E_L) + I_{ext}(t) \tag{5.11}$$

with $G_{Na}$ , $G_{K,fast}$ and $G_{K,slow}$ the electrical conductances for sodium, fast potassium and slow potassium currents, respectively. $E_{Na}$ and $E_K$ are the reversal potentials for sodium and potassium, respectively. $G_L$ is the leak conductance and is the leak-current reversal potential. $I_{ext}$ is an externally applied current, which in our case can be a synaptic input or input elicited by a TMS pulse.

The conductance of the ion channels is given by $G_{Na} = g_{Na}^{max} m^3 h$, $G_{K,fast} = g_{K,fast}^{max} n^4$, $G_{K,slow} = g_{K,slow}^{max} q^2$. The values for the leak conductance, maximum conductances and reversal potentials are given in Table 1. The dynamics of the activation and in-activation parameters $m$, $h$, $n$, and $q$ are given by first-order differential equations of the time and voltage-dependent gate variables for activation and inactivation, and are expressed as

$$\frac{dx}{dt} = \frac{x_\infty - x}{\tau_x} \tag{5.12}$$

where $x$ represents the activation or inactivation parameter. The time constant $\tau_x$ and the steady-state value $x_\infty$ are given by

$$\tau_x = \frac{1}{\alpha_x + \beta_x} \tag{5.13}$$

and

$$x_\infty = \frac{\alpha_x}{\alpha_x + \beta_x} \tag{5.14}$$

respectively.

The transition rates $\alpha_x$ and $\beta_x$ are voltage dependent and are given by

$$\alpha_m = \frac{-0.4V_m + 7}{\exp\left(-\frac{V_m - 17.5}{5}\right) - 1} \tag{5.15}$$

$$\beta_m = \frac{0.4V_m - 18}{\exp\left(\frac{V_m - 45}{5}\right) - 1} \tag{5.16}$$

$$\alpha_h = \frac{0.15}{\exp\left(\frac{V_m - 34.26}{18.19}\right)} \tag{5.17}$$

$$\beta_h = \frac{4}{\exp\left(-\frac{V_m - 40}{10}\right) + 1} \tag{5.18}$$

$$\alpha_n = \frac{-0.02V_m + 0.4}{\exp\left(-\frac{V_m - 20}{10}\right) - 1} \tag{5.19}$$

$$\beta_n = \frac{0.16}{\exp\left(\frac{V_m - 33.79}{66.56}\right) - 0.032} \tag{5.20}$$

$$\alpha_q = \frac{3.5}{\exp\left(-\frac{V_m - 55}{4}\right) - 1} \tag{5.21}$$

$$\beta_q = \frac{0.035}{\exp\left(-\frac{V_m + 50}{0.001}\right) + 1} \tag{5.22}$$

Equations 5.15- 5.20 were taken from Vieira and Kohn (2007). Equations 5.21-5.22 were adapted from Jones and Bawa (1997). All values for the membrane potential $V_m$ are in mV.

The synaptic conductance $g_{syn}$ is defined by the alpha-function

$$g_{syn} = \frac{\varepsilon}{\tau_s^2} t \exp\left(\frac{-t}{\tau_s}\right) \tag{5.23}$$

for $t \geq 0$. In our simulations we used the value $\tau_s$ = 0.2 ms, (in agreement with Finkel and Redman (1983) and Vieira and Kohn (2007)) and $\varepsilon$ = 0.4 $\mu$S.

# Bibliography

**Abbott LF**. Lapique's introduction of the integrate-and-fire model neuron (1907). *Brain Research Bulletin* 50(5/6): 303–304, 1999.

**Adrian ED**. The impulses produced by sensory nerve endings. Part I. *Journal of Physiology* 61(1): 49–72, 1926.

**Amassian VE, Cracco RQ, and Maccabee PJ**. Focal stimulation of human cerebral cortex with the magnetic coil: a comparison with electrical stimulation. *Electroencephalography and Clinical Neurophysiology* 74: 401–416, 1989.

**Aradi I and Holmes WR**. Role of multiple calcium and calcium-dependent conductances in regulation of hippocampal dentate granule cell excitability. *Journal of computational Neuroscience* 6: 215–235, 1999.

**Azouz R and Gray CM**. Dynamic spike threshold reveals a mechanism for synaptic coincidence detection in cortical neurons in vivo. *Proceedings of the National Academy of Sciences USA* 97: 8110–8115, 2000.

**Baker SN**. Oscillatory interactions between sensorimotor cortex and the periphery. *Current Opinion in Neurobiology* 17: 649–655, 2007.

**Baker SN, Olivier E, and Lemon R**. Coherent oscillations in monkey motor cortex and hand muscle EMG show task-dependent modulation. *The Journal of Physiology* 501: 225–241, 1997.

**Baker SN, Pinches EM, and Lemon RN**. Synchronization in monkey cortex during a precision grip task. II. Effect of oscillatory activity on corticospinal output. *Journal of Neurophysiology* 89: 1941–1953, 2003.

**Baker SN, Sprinks R, Jackson A, and Lemon RN**. Synchronization in Monkey Motor Cortex During a Precision Grip Task. I. Task-dependent modulation in single-unit synchrony. *Journal of Neurophysiology* 85: 869–885, 2001.

**Bal R, Green G, Rees A, and Sanders D**. Firing patterns of inferior colliculus neurons-histology and mechanism to change firing patterns in rat brain slices. *Neuroscience Letters* 317: 42–46, 2002.

**Battaglia D, Brunel N, and Hansel D**. Temporal decorrelation of collective oscillations in neural networks with local inhibition and long-range excitation. *Physical Review Letters* 99(23): 238106, 2007.

**Beaulieu C, Kisvarday Z, Somogyi P, Cynader M, and Cowey A**. Quantitative distribution of GABA-immunopositive and -immunonegative neurons and synapses in the monkey striate cortex (area 17). *Cerebral Cortex* 2(4): 295–309, 1992.

**Berne RM and Levy MN**. *Physiology*. the C.V. Mosby Company, 1988.

**Binder MD, Heckman CJ, and Powers RK**. How different afferent inputs control motoneuron discharge and the output of the motoneuron pool. *Current opinion in Neurobiology* 3: 1028–1034, 1993.

**Bremner FD, Baker JR, and Stephens JA**. Correlation between the discharges of motor units recorded from the same muscle and from different finger muscles in man. *The Journal of Physiology* 432: 355–380, 1991.

**Brown EN, Kass RE, and Mitra PP**. Multiple neural spike train data analysis: state-of-the-art and future challenges. *Nature Neuroscience* 7: 456–461, 2004.

**Buia C and Tiesinga P**. Attentional modulation of firing rate and synchrony in a model cortical network. *Journal of Computational Neuroscience* 20(3): 247–264, 2006.

**Burke RE**. *Handbook of Physiology. The Nervous System. Motor Control.* Bethesda, MD, 1981.

**Bushnell M, Goldberg ME, and Robinson DC**. Behavioral enhancement of visual responses in monkey cerebral cortex. I modulation in posterior parietal cortex related to selective visual attention. *Journal of Neurophysiology* 46(4): 755–772, 1981.

**Buzsáki G**. Large-scale recording of neuronal ensembles. *Nature Neuroscience* 7: 446–451, 2004.

**Buzsáki G and Draguhn A**. Neuronal oscillations in cortical networks. *Science* 304: 1926–1929, 2004.

**Canolty RT, Edwards E, Dalal S, Soltani M, Nagaranja SS, Kirsch HE, Berger MS, Barbaro NM, and Knight RT**. High gamma power is phase-locked to theta oscillations in human neocortex. *Science* 313: 1626–1628, 2006.

**Câteau H, Kitano K, and Fukai T**. Interplay between phase response curve and spike-timing dependent plasticity leading to wireless clustering. *Phys Rev E* 77: 051909, 2008.

**Chelazzi L, Duncan J, Miller EK, and Desimone R**. Responses of neurons in inferior temporal cortex during memory-guided visual search. *Journal of Neurophysiology* 80: 2918–2940, 1998.

**Chelazzi L, Miller EK, Duncan J, and Desimone R**. Responses of neurons in macaque area V4 during memory-guide visual search. *Cerebral Cortex* 11: 761–772, 2001.

**Conway BA, Halliday DM, Farmer SF, Shahani U, Maas. P, Weir AI, and Rosenberg JR**. Synchronization between motor cortex and spinal motoneuronal pool during the performance of a maintained motor task in man. *The Journal of Physiology* 489: 917–924, 2001.

**Corbetta M and Shulman GL**. Control of goal-directed and stimulus-driven attention in the brain. *Nature Reviews Neuroscience* 3: 201–215, 2002.

**Datta AK, Farmer SF, and Stephens JA**. Central nervous pathways underlying synchronization of human motor unit firing studied during voluntary contractions. *The Journal of Physiology* 432: 401–425, 1991.

**Davies RM, Gerstein GL, and Baker SN**. Measurement of time-dependent changes in the irregularity of neural spiking. *Journal of Neurophysiology* 96: 906–918, 2006.

**Day BL, Rothwell JC, Thompson PD, Dick JPR, Cowan A, Berardelli A, and Marsden CD**. Motor cortex stimulation in intact man. II. Multiple descending volleys. *Brain* 110: 1191–1209, 1987.

**Dayan P and Abbott LF**. *Theoretical Neuroscience*. MIT Press, 2001.

**deCharms RC and M. M. Merzenich M**. Primary cortical representation of sounds by the coordination of action-potential timing. *Nature* 381(6583): 610–613, 1996.

**Deco G and Rolls E**. Neurodynamics of biased competition and cooperation for attention: A model With spiking neurons. *Journal of Neurophysiology* 94: 295–313, 2005.

**Denker M, Timme M, Diesmann M, Wolf F, and Geisel T**. Breaking synchrony by heterogeneity in complex networks. *Physical Review Letters* 92(7): 074103, 2004.

**Desimone R and Duncan J**. Neural mechanisms of selective visual attention. *Annual Review of Neuroscience* 18: 193–222, 1995.

**Destexhe A, Rudolph M, Fellous JM, and Sejnowski TJ**. Fluctuating synaptic conductances recreated in vivo-like activity in neocortical neurons. *Neuroscience* 107(1): 13–24, 2001.

**Eckhorn R, Frien A, Bauer R, Woelbern T, and Kehr H**. High frequency (60-90 Hz) oscillations in primary visual cortex of awake monkey. *NeuroReport* 4: 243–246, 1993.

**Edgley SA, Eyre JA, Lemon RN, and Miller S**. Excitation of the corticospinal tract by electromagnetic and electrical stimulation of the scalp in the macaque monkey. *The Journal of Physiology* 425: 301–320, 1990.

**Edwards E, Soltani M, Deouell LY, Berger M, and Knight RT**. High gamma activity in response to deviant auditory stimuli recorded directly from human cortex. *Journal of Neurophysiology* 94(6): 4269–4280, 2005.

**Ellaway PH, Davey NJ, Maskill DW, Rawlinson SR, Lewis HS, and Anissimova NP**. Variability in the amplitude of skeletal muscle responses to magnetic stimulation of the motor cortex in man. *Electroencephalography and Clinical Neurophysiology* 109: 104–113, 1998.

**Engel AK, Fries P, and Singer W**. Dynamic predictions: Oscillations and synchrony in top-down processing. *Nature Reviews Neuroscience* 2(10): 704–716, 2001.

**Ernst U, Pawelzik K, and Geisel T**. Synchronization induced by temporal delays in pulse-coupled oscillators. *Physical Review Letters* 74(9): 1570–1573, 1995.

**Ernst U, Pawelzik K, and Geisel T**. Delay-induced multistable synchronization of biological oscillators. *Physical Review E* 57: 2150–2162, 1998.

**Feng J and Brown D**. Impact of correlated inputs on the output of the Integrate-and-Fire model. *Neural Computation* 12: 671–692, 2000.

**Ferbert A, Priori A, Rothwell JC, Day BL, Colebatch JG, and Marsden CD**. Interhemispheric inhibition of the human motor cortex. *The Journal of Physiology* 453: 525–546, 1992.

**Finkel AS and Redman SJ**. The synaptic current evoked in cat spinal motoneurons by impulses in single group Ia axons. *The Journal of Physiology* 342: 615–632, 1983.

**Fleshman JW, Segev I, and Burke RB**. Electrotonic architecture of type-identified alpha-motoneurons in the cat spinal cord. *Journal of Neurophysiology* 60: 60–85, 1988.

**Frien A, Eckhorn R, Bauer R, Woelbern T, and Kehr H**. Stimulus specific fast oscillations at zero phase between areas V1 and V2 of awake monkey. *NeuroReport* 5: 2273–2277, 1994.

**Fries P**. A mechanism for cognitive dynamics: neuronal communication through neuronal coherence. *Trends in Cognitive Sciences* 9(10): 474–480, 2005.

**Fries P**. Finding gamma. *Neuron* 58: 303–306, 2008.

**Fries P, Neuenschwander S, k. Engel A, Goebel R, and Singer W**. Rapid feature selective neuronal synchronization through correlated latency shifting. *Nature Neuroscience* 4: 194–200, 2001a.

**Fries P, Reynold JH, Rorie AE, and Desimone R**. Modulation of oscillatory neuronal synchronization by selective attention. *Science* 291: 1560–1563, 2001b.

**Fries P, Schröder JH, Roelfsema PR, Singer W, and Engel AK**. Oscillatory neuronal synchronization in primary visual cortex as a correlate of stimulus selection. *The Journal of Neuroscience* 22: 3739–3754, 2005.

**Gawne TJ and Martin JM**. Responses of primate visual cortical V4 Neurons to simultaneously presented stimuli. *Journal of Neurophysiology* 88: 1128–1135, 2002.

**Gerstner W and Kistler WM**. *Spiking Neuron Models. Single Neurons, Populations, Plasticity*. Cambridge University Press, 2002.

**Gray CM, König P, Engel AK, and Singer W**. Oscillatory responses in cat visual cortex exhibit intercolumnar synchronization which reflects global stimulus properties. *Nature* 338: 334–337, 1989.

**Haken H**. *Brain Dynamics*. Springer, 2008.

**Hari R and Salenius S**. Rhythmical corticomuscular communication. *NeuroReport* 10: 1–10, 1999.

**Henneman E, Somjen G, and Carpenter DO**. Functional significance of cell size in spinal motoneurons. *Journal of Neurophysiology* 28: 560–580, 1965.

**Higley MJ and Contreras D**. Balanced excitation and inhibition determine spike timing during frequency adaptation. *Journal of Neuroscience* 26(2): 448–457, 2005.

**Hines ML and Carnevale NT**. The NEURON simulation environment. *Neural Computation* 9: 1179–1209, 1997.

**Hodgkin AL and Huxley AF**. A quantitative description of membrane current and its application to conduction and excitation in a nerve. *Journal of Physiology* 117: 500–544, 1952.

**Horikawa K, Ishimatu K, Yoshimoto E, Kondo S, and Takeda H**. Noise-resistant and synchronized oscillation of the segmentation clock. *Nature* 441: 719–723, 2006.

**Izhikevich EM**. *Dynamical systems in neuroscience*. MIT Press, 2007.

**Jarvis MR and Mitra PP**. Sampling properties of the spectrum and coherence of sequences of action potentials. *Neural Computation* 13: 717–749, 2001.

**Jones KE and Bawa P**. Computer simulation of the responses of human motoneurons to composite Ia EPSPs: effects of backgroundfiring rate. *Journal of Neurophysiology* 77: 405–420, 1997.

**Kandel RE and Schwartz J**. *Principles of Neural Science*. Edward Arnold, Ltd., 1982.

**Kaneko K, Kawai Y, Fuchigami S, Morita H, and Ofuji. A**. The effect of current direction induced by transcranial magnetic stimulation on the corticospinal excitability in human brain. *Electroencephalography and Clinical NeurophysiologyElectromyography and Motor Control* 101(6): 478–482, 1996.

**Kernell D and Zwaagstra B**. Size and remoteness: two relatively independent parameters of dendrites, as studied for spinal motoneurons of the cat. *The Journal of Physiology* 413: 233–254, 1989.

**Kiehn O and Eken T**. Functional role of plateau potentials in vertebrate motor neurons. *Current Opinion of Neurobiology* 8: 746–752, 1998.

**Kiers L, Cros D, Chiappa KH, and Fang J**. Variability of motor potentials evoked by transcranial magnetic stimulation. *Electroencephalography and Clinical Neurophysiology* 89: 415–423, 1993.

**Kilner JM, Baker SN, Salenius S, Hari R, and Lemon RN**. Human cortical muscle coherence is directly related to specific motor parameters. *The Journal of Neuroscience* 20: 8838–8845, 2000.

**Kilner JM, Baker SN, Salenius S, Jousmaki V, Hari R, and Lemon RN**. Task-dependent modulation of 15-30 Hz coherence between rectified EMGs from human hand and forearm muscles. *The Journal of Physiology* 516: 559–570, 1999.

**Kleine BU, Blok JH, Oostenveld R, Praamstra P, and Stegeman DF**. Magnetic stimulation-induced modulations of motor unit firings extracted from multi-channel surface EMG. *Muscle and Nerve* 23: 1005–1015, 2000.

**Kreiter AK and Singer W**. Stimulus-dependent synchronization of neural responses in the visual cortex of awake macaque monkey. *The Journal of Neuroscience* 16(7): 2381–2396, 1996.

**Kruglikov SY and Schiff SJ**. Interplay of electroencephalogram phase and auditory-evoked neural activity. *The Journal of Neuroscience* 23(31): 10122–10127, 2003.

**Kuhn A, Aertsen A, and Rotter S**. Neuronal integration of synaptic input in the fluctuation-driven regime. *The Journal of Neuroscience* 24: 2345–2356, 2004.

**Kujirai T, Caramia MD, Rothwell JC, Day BL, Thompson PD, Ferbert A, Wroe S, Asselman P, and Marsden CD**. Corticocortical inhibition in human motor cortex. *The Journal of Physiology* 471: 501–519, 1993.

**Kuramoto Y**. *Chemical Oscillations, Waves and Turbulence*. Springer, 1984.

**Lachaux JP, Rodriguez E, Martinerie J, and Varela F**. Measuring phase synchrony in brain signals. *Human Brain Mapping* 8: 194–208, 1999.

**Lazzaro VD, Restuccia D, Oliviero A, Profice P, Ferrara L, Insola A, Mazzone P, Tonali P, and Rothwell JC**. Effects of voluntary contraction on descending volleys evoked by transcranial stimulation in conscious humans. *Journal of Physiology London* 508(2): 625–633, 1998.

**Luck SJ, Chelazzi L, Hillyard SA, and Desimone R**. Neural mechanisms of spatial selective attention in areas V1, V2, and V4 of macaque visual cortex. *Journal of Neurophysiology* 77(1): 24–42, 1997.

**Luck SJ, Chelazzi L, Hillyard SA, and Desimone R**. Neural mechanisms of spatial selective attention in areas V1, V2, and V4 of macaque visual cortex. *Journal of Neurophysiology* 77: 24–42, 1999.

**Macefield VG, Gandevia SC, B. Bigland-Ritchie RBG, and Burke D**. The firing rates of human motoneurones voluntarily activated in the absence of muscle afferent feedback. *The Journal of Physiology* 471: 429–443, 1993.

**Maldonado PE, Friedman-Hill S, and Gray C**. Dynamics of striate cortical activity in the alert macaque: II. fast time scale synchronization. *Cerebral Cortex* 10(11): 1117–1131, 2000.

**Marmarelis PZ and Marmarelis VZ**. *Analysis of Physiological Systems: The White-Noise Approach.* New York: Plenum Press, 1978.

**Martinez D**. Oscillatory synchronization requires precise and balanced feedback inhibition in a model of the insect antennal lobe. *Neural Computation* 17: 2548–2570, 2006.

**Mazaheri A, Nieuwenhuis ILC, van Dijk H, and Jensen O**. Prestimulus alpha and mu activity predicts failure to inhibit motor responses. *Human brain mapping* 30(6): 1791–1800, 2009.

**Mazzitello KI, Arizmendi CM, and Hentschel HGE**. Converting genetic network oscillations into somite spatial pattern. *Physical Review E* 78: 021906, 2008.

**McAdam CJ and Maunsell JHR**. Effects of attention on orientation-tuning functions of single neurons in macaque cortical area V4. *The Journal of Neuroscience* 19(1): 431–441, 1999.

**McCoy EJ, Walden AT, and Percival DB**. Multitaper Spectral Estimation of Power Law Processes. *IEEE Transacions on Signal Processing* 46(3): 655–668, 1997.

**Miller EK, Gochin PM, and Gross CG**. Suppression of visual responses of neurons in inferior temporal cortex of a awake macaque by addition of a second stimulus. *Brain Research* 616: 25–29, 1993.

**Mills KR and Schubert M**. Short term synchronization of human motor units and their responses to transcranial magnetic stimulation. *The Journal of Physiology* 483: 511–523, 1995.

**Mirollo RE and Strogatz SH**. Synchronization of pulse-coupled biological oscillators. *SIAM Journal on Applied Mathematics* 50(6): 1645–1662, 1990.

**Mishra J, Fellous JM, and Sejnowski TJ**. Selective attention through phase relationship of excitatory and inhibitory input synchrony in a model cortical neuron. *Neural Networks* 19: 1329–1346, 2006.

**Mitchell WK, Baker MR, and Baker SN**. Muscle responses to transcranial stimulation in man depend on background oscillatory activity. *The Journal of Physiology* 583: 567–579, 2007.

**Mitra PP and Pesaran B**. Analysis of dynamic brain imaging data. *Biophysical Journal* 76(2): 691–708, 1987.

**Moore T and Amstrong KM**. Selective gating of visual signals by microstimulation of frontal cortex. *Nature* 421: 370–373, 2003.

**Moran J and Desimone R**. Visual attention gates visual processing in the extrastriate cortex. *Science* 229: 782–784, 1985.

**Motter BC**. Focal attention produces spatially selective processing in visual cortical areas V1, V2 and V4 in the presence of competing stimuli. *Journal of Neurophysiology* 70(3): 909–919, 1993.

**Nicolaev AR, Ivanitsky GA, Ivanitsky AM, Posner MI, and Abdullaev YG**. Correlation of brain rhythms between frontal and left temporal (Wernickes) cortical areas during verbal thinking. *Neuroscience Letters* 298: 107–110, 2001.

**Percival DB and Walden AT**. *Spectral analysis for physical applications: Multitaper and Conventional Univariate techniques*. Cambridge Univ. Press, Cambridge, UK, 2002.

**Pesaran B, Pezaris JS, Sahani M, Mitra PP, and Andersen RA**. Temporal structure in neuronal activity during working memory in macaque parietal cortex. *Nature Neuroscience* 5: 805–811, 2002.

**Reynolds JH, Chelazzi L, and Desimone R**. Competitive mechanisms subserve attention in macaque areas V2 and V4. *The Journal of Neuroscience* 19(5): 1736–1753, 1999.

**Reynolds JH and Desimone R**. Interacting roles of attention and visual salience in V4. *Neuron* 37: 853–863, 2003.

**Rieke F, Warland D, de Ruyter van Stevenick R, and Bialek W**. *Spikes - exploring the neuronal code*. the MIT Press, 1997.

**Roelfsema PR, Lamme VAF, and Spekreijse H**. Synchrony and covariation of firing rates in the primary visual cortex during contour grouping. *Nature Neuroscience* 7(9): 982–991, 2004.

**Rolls ET, Franco L, Aggelopous NC, and Reece S**. An information theoretic approach to the contributions between the firing rates and the correlations between the firing neurons. *Journal of Neurophysiology* 89: 2810–2822, 2003.

**Rolls ET and Tovee MJ**. The responses of single neurons in the temporal visual cortical areas of the macaque when more than one stimulus is present in the receptive field. *Experimental Brain Research* 103: 409–420, 1995.

**Rols G, Girard CBP, Bertrand O, and Bullier J**. Cortical mapping of gamma oscillations in areas V1 and V4 of the macaque monkey. *Visual Neuroscience* 18(4): 527–540, 2001.

**Rothwell JC, Thompson PD, Day BL, Boyd S, and Marsden CD**. Stimulation of the human motor cortex through the scalp. *Experimental Physiology* 76: 159–200, 1991.

**Salenius S, Portin K, Kajola M, Salmelin R, and Hari R**. Cortical control of human motoneuron firing during isometric contraction. *Journal of Neurophysiology* 77: 3401–3405, 2000.

**Salinas E and Sejnowski T**. Impact of correlated synaptic input on output firing rate and variability in simple neuronal models. *The Journal of Neuroscience* 20: 6193–6209, 2000.

**Salinas E and Sejnowski T**. Correlated neuronal activity and the flow of neural information. *Nature Reviews Neuroscience* 2: 539–550, 2001.

**Salinas E and Sejnowski T**. Integrate-and-Fire neurons driven by correlated stochastic input. *Neural Computation* 14: 2111–2155, 2002.

**Schoffelen JM, Oostenveld R, and Fries P**. Neuronal coherence as a mechanism of effective corticospinal interaction. *Science* 308(5718): 111–113, 2005.

**Senn W and Urbancik R**. Similar non-leaky integrate-and-fire neurons with instantaneous coupling always synchronize. *SIAM Journal on Applied Mathematics* 61(4): 1143–1155, 2000.

**Shim S, Imboden M, and Mohanty P**. Synchronized oscillation in coupled nanomechanical oscillators. *Science* 316: 95–99, 2007.

**Shusterman V and Troy WC**. From base-line to epileptiform acivity: a path to synchronized rhythmicity in large-scale neural networks. *Physical Review E* 77: 061911, 2008.

**Singer W and Gray CM**. Visual feature integration and the temporal correlation hypothesis. *Annual Review Neuroscience* 18: 555–586, 1995.

**Smith AT, Singh KD, Williams AL, and Greenlee MW**. Estimating receptive field size from fMRI data in human striate and extrastriate visual cortex. *Cerebral Cortex* 11: 1182–1190, 2002.

**Smiyukha Y, Mandon F, Galashan FO, Neitzel SD, and Kreiter A**. Attention-dependent switching of interareal synchronization between V4 neurons and different subpopulations of their V1 afferents. *Society for Neuroscience Abstract* 32: 11.2, 2006.

**Spitzer H, Desimone R, and Moran J**. Increased attention enhances both behavioural and neuronal performance. *Science* 240(4850): 338–340, 1988.

**Stroeve T and Gielen C**. Correlation between uncoupled conductance-based integrate-and-fire neurons due to common and synchronous presynaptic firing. *Neural Computation* 13: 2005–2030, 2001.

**Tass P, Rosenblum MG, Weule J, Kurths J, Pikovsky A, Volkmann J, Schnitzler A, and Freund HJ**. Detection of *n:m* phase locking from noisy data: Application to magnetoencephalography. *Physical Reviews Letter* 81(15): 3291–3294, 1998.

**Tass PA**. *Phase Resetting in Medicine and Biology*. Springer, 1999.

**Taylor K, Mandon S, Freiwald WA, and Kreiter AK**. Coherent oscillatory activity in monkey area V4 predicts successfull allocation of attention. *Cerebral Cortex* 15(9): 1424–1437, 2005.

**Thomson DJ**. Spectrum estimation and harmonic analysis. *Proceedings of the IEEE* 70: 1055–1096, 1982.

**Tiesinga PHE**. Stimulus competition by inhibitory interference. *Neural Computation* 17: 2421–2453, 2005.

**Timme M, Wolf F, and Geisel T**. Unstable attractors induce perpetual synchronization and desynchronization. *Chaos* 13: 377–387, 2003.

**Tovee MJ and Rolls ET**. Oscillatory activity is not evident in the primate temporal visual-cortex with static stimuli. *NeuroReport* 3(4): 369–372, 1992.

**Traub RD and Miles R**. *Neuronal networks of the hippocampus*. Cambridge, UK: Cambridge Univ. Press., 1991.

**Treue S and Maunsell JHR**. Attentional modulation of visual motion processing in cortical areas MT and MST. *Nature* 382: 539–541, 1996.

**Treue S and Maunsell JHR**. Effects of attention on the processing of motion in macaque visual cortical areas MT and MST. *The Journal of Neuroscience* 19(17): 7603–7616, 1999.

**Treue S and Trujillo JCM**. Feature-based attention influences motion processing gain in macaque visual cortex. *Nature* 399: 575–579, 1999.

**Tsodyks M, Pawelzik K, and Makram H**. Neural networks with dynamic synapses. *Neural Computation* 10: 821–835, 1998.

**Tsodyks M, Uziel A, and Makram H**. Synchrony generation in recurrent networks with frequency-dependent synapses. *The Journal of Neuroscience* 20(RC50): 1–5, 2000.

**Tsubo Y, Takada M, Reyes A, and Fukai T**. Layer and frequency dependencies of phase response properties of pyramidal neurons in rat motor cortex. *European Journal of Neuroscience* 25(11): 3429–3441, 2007.

**van der Heyden MJ, Hilgevoord AAJ, Bour LJ, and de Visser BWO**. Modeling motoneuron firing properties: dependency on size and calcium dynamics. *Biological Cybernetics* 72: 133–139, 1994.

**van der Kamp W, Zwinderman AH, Ferrari MD, and van Dijk JG**. Cortical excitability and response variability of transcranial magnetic stimulation. *Journal of Clinical Neurophysiology* 13: 164–171, 1996.

**van der Togt C, Kalitzin S, Spekreijse H, Lamme VAF, and Super H**. Synchrony dynamics in monkey V1 predicts success in visual detection. *Cerebral Cortex* 16(1): 136–148, 2006.

**van Elswijk G, Maij F, Schoffelen JM, Overeem S, Stegeman DF, and Fries P**. Rhythmic neuronal synchronization entails rhythmic gain modulation. *Submitted* 2009.

**Vieira MF and Kohn AF**. Compartmental models of mammalian motoneurons of types S, FR and FF and their computer simulation. *Computers in Biology and Medicine* 37: 842–860, 2007.

**Vreeswijk C, Abbott LF, and Ermentrout GB**. When inhibition not excitation synchronizes neural firing. *Journal of Computational Neuroscience* 1: 313–321, 1994.

**Waldert S, Preissl H, Demandt E, Braun C, Birbaumer N, Aertsen A, and Mehring C**. Hand Movement Direction Decoded from MEG and EEG. *The Journal of Neuroscience* 28: 1000–1008, 2008.

**Webb CG and Cope TC**. Influence of synaptic identity on single-Ia-afferent connectivity and EPSP amplitude in the adult cat: homonymous versus heteronymous connections. *Journal of Neurophysiology* 68: 1046–1052, 1992.

**Werhahn KJ, Kunesch E, Noachtar S, Benecke. R, and Classen J**. Differential effects on motorcortical inhibition induced by blockade of GABA uptake in humans. *The Journal of Physiology* 517: 591–597, 1999.

**Whittington MA, Traub RD, Kopell N, Ermentrout B, and Buhl EH**. Inhibition-based rhythms: experimental and mathematical observations on network dynamics. *International Journal of Psychophysiology* 38: 315–336, 2000.

**Winfree A**. *The Geometry of Biological Time*. Springer, 1980.

**Witham CL and Baker SN**. Network oscillations and intrinsic spiking rhythmicity do not covary in monkey sensorimotor areas. *The Journal of Physiology* 580: 801–814, 2007.

**Womelsdorf T and Fries P**. The role of neuronal synchronization in selective attention. *Current Opinion in Neurobiology* 17: 154–160, 2007.

**Womelsdorf T, Fries P, Mitra PP, and Desimone R**. Gamma-band synchronization in visual cortex predicts speed of change detection. *Nature* 439: 733–736, 2006.

**Womelsdorf T, Schoffelen JM, Oostenveld R, Singer W, Desimone R, Engel AK, and Fries. P**. Modulation of neuronal interactions through neuronal synchronization. *Science* 316: 1609–1612, 2007.

**Zeitler M, Daffertshofer A, and Gielen CCAM**. Asymmetry in pulse-coupled oscillators with delay. *Physical Review E* 79: 065203(R), 2009.

**Zeitler M, Fries P, and Gielen S**. Assessing neuronal coherence with single-unit, multi-unit and local field potentials. *Neural Computation* 18(9): 2256–2281, 2006.

# Publications

## Articles

**M. Zeitler, P. Fries and S. Gielen**, Assessing neuronal coherence with single-unit, multi-unit and local field potentials *Neural Computation* 18(9):2256-2281, 2006

**M. Zeitler, P. Fries and S. Gielen**, Biased competition through variation in amplitude of $\gamma$-oscillations. *Journal of Computational Neuroscience* 25:89-107, 2008

**M. Zeitler, A. Daffertshofer and C. C. A. M. Gielen**,Asymmetry in pulse-coupled oscillators with delay. *Physical Review E* 79:065203(R), 2009

**M. Zeitler, J. Tramper, D.F. Stegeman and C. C. A. M. Gielen**,Effective communication by neuronal coherence: a model study. *in preparation*

# Summary

In this thesis, we studied various aspects of neuronal synchronisation, like detection of synchronised activity and a possible functional role for stimulus selection and for effective neuronal communication.

Oscillations have been observed in many brain areas (Gray et al., 1989; Edwards et al., 2005; Schoffelen et al., 2005). Different frequency bands are thought to be related to different functional properties of the brain (Buzsáki and Draguhn, 2004). Gamma oscillations (30-80 Hz) are thought to be related to cognitive task like memory (Pesaran et al., 2002) and attention (Fries, 2008) and possibly also involved in the transfer of information (Fries, 2005). An increase in power in the gamma band can be related to an increase in working memory load (Pesaran et al., 2002) or an increase in attention (Fries, 2008). This thesis presents a theoretical framework to understand the experimental findings reported above.

In the first part of this thesis (**Chapter 2**) we investigated why experimentally derived coherence estimates between multi unit (6-10 neurons) recordings are significantly higher than that between single unit recordings. Starting with a qualitative understanding of the interpretation of correlated output spike trains in terms of correlated input to the neurons, we continued by comparing the coherence results obtained for single-unit recording with those obtained for multi-unit activities for several neuron models and additionally also for experimentally obtained recordings. All results showed significantly higher coherence estimates for multi-unit than for single unit activities. One of the differences between the coherence estimates of single and multi-unit recordings was the total number of spikes used in the calculations. In order to investigate the difference in the coherence value between multi-unit and single-unit signals we repeated the data-analysis for a reduced number of multi-unit recordings, in such a way that the total number of spikes, used for the coherence estimates, was similar to the number of spikes used for the coherence estimates for the single-unit recordings. Although the 95% significance band broadened, the coherence estimates of these reduced number of multi-unit recordings was still significantly higher than for the single unit recordings. The reason for this is that the signal-to-noise (SNR) ratio in the multi-unit recording is much better compared to the SNR of the single unit recordings. This implies that the coherence estimates for multi-unit recordings are in general higher than for single unit recordings because the correlations between the individual single unit activities that are contained within the multi unit recording contribute to a larger signal-to-noise ratio.

In **Chapter 3** we investigated whether synchronised activity can be an effective mechanism to modulate synaptic efficacy. Experiments in visual cortex have shown that the firing rate of a neuron is related to the visual stimulus within the receptive field of the recorded neuron: a preferred stimulus causes a high firing rate, a non-preferred a lower firing rate. Since the size of the receptive field increases for neurons in higher visual areas, two stimuli can be presented simultaneously within the receptive field of the recorded neuron. Experiments in visual cortex have shown that the firing rate of a neuron in response to the simultaneous presentation of a preferred and non-preferred visual stimulus within the receptive field is intermediate between that for the two stimuli alone. Experiments have also shown that if one of the two visual stimuli within the receptive field of the recorded neuron is attended, the firing rate is driven towards the firing rate of that stimulus alone. A rate model (Reynolds et al., 1999) can reproduce these firing rate findings only if the strength of the synapses of the neurons that represent the attended stimulus are increased by a factor of 5. Fries et al. (2001b) showed that due to attention an increase in coherence occurs, even before the firing rate increased. Our results have shown that an increased coherence between input and output signals can be caused by an increase in synchrony of the input activity. Can an increase in synchrony between the input activities, representing the attended visual stimulus, also explain the firing rates for the different conditions as described above? In **Chapter 3** we showed that a simple feedforward model with fixed synaptic conductance values can indeed reproduce attention and selective attention effects using synchronisation in the gamma-frequency range to increase the effective synaptic gain for the responses to the attended stimulus. The performance of the model is robust to changes in the parameter values. In this chapter we also determined the phase locking value to obtain a measure to compare the phase locking between the receiving output neuron and each of the two input populations of neurons. The communication through coherence hypothesis states that the phase locking between the sending and receiving population can change over time in order to enable/disable the temporal (effective) communication window. The model described in **Chapter 3** predicts that the phase locking between presynaptic input and output spikes increases with more synchronised input activity. This implies that synchronisation of neuronal activity is a good candidate to modulate the synaptic efficacy and to enable/disable the effectiveness of the communication window.

If the activity of a neuronal population is highly synchronised it can be approximated by a neuronal oscillator, e.g. a Mirollo-Strogatz (MS) oscillator. By coupling two Mirollo-Strogatz oscillators, one can investigate the phase relation between two such neuronal populations as a function of excitatoty or inhibitory coupling strength and as a function of the time delay between generation of a spike and its arrival at the other oscillator. In **Chapter 4** we studied analytically the stable states of two pulse-coupled MS oscillators with and without a time delay. Without time delay and with equal coupling strengths, two excitatory pulse-coupled oscillators will fire in-phase (Mirollo and Strogatz, 1990). With a time delay two stable states exist in which they fire out-of-phase (Ernst et al., 1995, 1998). In the brain symmetric coupling is an exception rather than the rule. Due to learning and plasticity the coupling strengths can change continuously. In **Chapter 4** we investigated the effect of asymmetric coupling strengths between two MS-oscillators with time-delay. For large time delays only one stable state exists in which the oscillators are exactly in anti-phase. For large differences in excitatory coupling strengths and with small time delays only one stable state exists in which the oscillator ($A$) that receives the strongest input is driven by the other ($B$). This implies that information is transmitted reliably in one direction (from $B$ to $A$), and less reliably in the other direction. For small differences in coupling strengths two stable states exist, like for symmetric couplings ($A$ drives $B$ and vice versa). A change in coupling strength (e.g. due to learning) does not change the phase of the stable state unless it merges with an unstable state (saddle-node bifurcation) and disappears.

Symmetric inhibitory coupling of two MS-oscillators shows a stable in-phase state (Ernst et al., 1995, 1998), independent of time delays. Under certain conditions a second stable state exists in which the two oscillators fire exactly in anti-phase. The more realistic asymmetric couplings destroy the exact in-phase and anti-phase relationships and also reduce the region for which two stable states exists. So, asymmetric coupling reduces the region of bistability and a pronounced asymmetric coupling supports the reliable information transfer between neurons in one direction only.

In **Chapter 5** we explored the role of the phase of the population activity in the communication between two neuronal populations. For this study we modelled the corticospinal system as a feed forward network in which the neurons in the motor cortex project to the $\alpha$-motoneurons in spinal cord. Simulations showed that the (much weaker) projections from spinal cord to motor cortex could be neglected as predicted by our results described in **Chapter 4**. First we reproduced the experimental findings of van Elswijk et al. (2009), who showed that the effectiveness of the neuronal communication between motor cortex and spinal cord is modulated by the phase of the receiving population, as predicted by the Communication-Through-Coherence hypothesis. Although much less pronounced, the MEP amplitude also depends on the phase of the beta drive of the neurons in motor cortex in our study. This result differs from that obtained in experimental studies (van Elswijk et al., 2009), presumably because the phase-dependence is too small to become significant in experimental studies. Our results suggest that the MEP amplitude and pre-TMS beta drive are correlated indirectly by the coherence between beta drive and EMG. The basic principles, that underlie the results of this study, do apply equally well to other frequencies of rhythmic neuronal oscillations like alpha, mu, and gamma rhythms.

# Samenvatting

In de loop der jaren heb ik al vaak de vraag gehoord: ”Mama, weet jij waar mijn fietssleutel ligt?”Als ik dan antwoordde: ”Die ligt op de eettafel bij jouw spullen, die je nog moet opruimen.”, kreeg ik vaak een ontkennende reactie. Maar als ik dan vervolgens zei: ”Helemaal rechts van de stapel, naast je broodtrommel.”, dan kwam er meestal een teken van herkenning. Het beeld dat op het netvlies viel, veranderde niet, maar wel de toestand van het brein, doordat de beschrijving cq. opdracht, nauwkeuriger gegeven werd. Dit voorbeeld toont aan dat niet alle informatie die op ons netvlies valt, geheel verwerkt wordt door onze hersenen. De hersenen selecteren de voor ons relevante informatie om die verder te verwerken en de niet-relevante informatie wordt genegeerd. Een voorbeeld hiervan dat zeer veel indruk op mij gemaakt heeft, vindt u op http://viscog.beckman.illinois.edu/falshmovie/15.php (een soortgelijke film vindt u op www.dothetest.co.uk). In het basketball filmpje ziet u twee teams. Elk team heeft een bal, die door de teamleden naar elkaar doorgespeeld wordt. Hoe vaak wordt de bal door de spelers met de witte t-shirts aan, naar elkaar doorgespeeld? Veel succes met tellen! Als u het filmpje nog niet bekeken heeft, lees dan niet de volgende regels, maar gaat u verder bij de volgende alinea. Indien u geteld heeft en het antwoord weet, kijkt u dan nog eens naar het filmpje, ziet u nu ook een gorilla die zwaait en een dansje maakt? Welke mechanismen ten grondslag liggen aan het selectief doorgeven van informatie zullen in dit proefschrift verder onderzocht worden.

Dit proefschrift beschrijft diverse aspecten van neuronale ritmische (oscillatoire) synchronisatie, zoals het detecteren van synchrone neuronale activiteit en een mogelijke functionele rol in het negeren en selecteren van stimuli en in de effectiviteit van neuronale communicatie. Voor dit onderzoek, dat theoretisch van aard was, zijn diverse modellen gebruikt, die een beschrijving van de activiteit van een neuron geven (**Hoofdstuk 1**). De modellen zijn gebruikt voor de uitgevoerde computer-simulaties en indien mogelijk ook in wiskundige analyses.

In het brein zijn op vele plaatsen oscillaties waar genomen (Gray et al., 1989;

Edwards et al., 2005; Schoffelen et al., 2005). De verschillende frequenties behorende bij deze oscillaties, zijn opgedeeld in frequentiebanden. Naburige frequentiebanden in een neuronaal netwerk worden geassocieerd met verschillende functionele toestanden van het brein (Buzsáki and Draguhn, 2004). Men veronderstelt dat gamma oscillaties (30 - 80 Hz) gerelateerd zijn aan cognitieve taken zoals geheugen (Pesaran et al., 2002) en aandacht (Fries, 2008) en mogelijk ook een rol spelen bij de informatieoverdracht (Fries, 2005) tussen neuronen.

In het eerste gedeelte van dit proefschrift (**Hoofdstuk 2**) wordt onderzocht waarom de experimenteel gevonden waardes voor de coherentie tussen multi-unit (6-10 neuronen) metingen significant hoger zijn dan tussen twee single-unit (1 neuron) metingen. De coherentie maat geeft aan hoe constant het faseverschil tussen twee oscillaties (van een bepaalde frequentie) is gedurende diverse herhalingen van het experiment. Een coherentie waarde van nul, betekent dat het faseverschil geheel willekeurig is, m.a.w. de signalen zijn niet gecorreleerd. Een coherentie waarde van precies één geeft aan dat het faseverschil altijd hetzelfde is. De coherentie wordt verlaagd door ruis in het (neuronale) systeem. In **Hoofdstuk 2** worden eerst enkele wiskundige afleidingen voor de coherentie beschreven als functie van het aantal neuronen $m$ en als functie van de mate waarin het inputsignaal van verschillende neuronen overeenkomt. De verkregen uitdrukkingen laten zien dat de coherentie tussen de activiteit van één neuron en zijn inputsignaal $\sqrt{m}$ keer lager is dan de coherentie tussen de gezamenlijke activiteit van $m$ neuronen en hun gezamenlijk inputsignaal. Verder volgt dat de coherentie tussen de activiteiten van twee individuele neuronen $m$ keer lager is dan de coherentie tussen de activiteiten van twee neuronale populaties, elk bestaande uit $m$ neuronen. Computer simulaties voor verschillende neuron modellen en experimentele resultaten bevestigen kwalitatief de wiskundige analyses. Eén van de verschillen bij de bepaling van de coherentie waardes voor single- en multi-unit recordings is het totaal aantal actie potentialen dat gebruikt wordt voor de berekening. Om het verschil in de coherentie waardes nader te onderzoeken, wordt de data analyse herhaald voor de multi-unit recordings waarbij in totaal (ongeveer) evenveel actie potentialen meegenomen worden voor de multi-unit recordings als voor de single-unit recordings. Door het verminderen van het aantal spikes in de bepaling van de coherentie wordt de 95% significantie band breder, maar blijven de waardes nog altijd significant hoger dan voor single-unit recordings. Dit komt omdat de signaal-ruis verhouding voor de multi-unit recordings veel beter is vergeleken met de signaal-ruis verhouding voor de single-unit recordings. Dit impliceert dat de coherentie voor multi-unit recording in het algemeen hoger is dan voor single-unit recordings omdat de correlaties tussen de individuele single-unit activiteiten van de multi-unit activiteit een grotere signaal-ruis verhouding geven.

In **Hoofdstuk 3** wordt onderzocht of synchrone neuronale activiteit een mechanisme kan zijn om de effectieve synaptische koppelingssterkte te varieëren. Experimenten in de visuele cortex (zie bijvoorbeeld Reynolds et al. (1999)) tonen aan, dat de vuurfrequentie van een neuron gerelateerd is aan de visuele stimulus in het receptieve veld van het gemeten neuron: een voorkeursstimulus veroorzaakt een hoge vuurfrequentie als responsie, andere stimuli een lagere vuurfrequentie. Aangezien de grootte van het receptieve veld toeneemt voor neuronen, die zich in hogere visuele gebieden bevinden (Desimone and Duncan, 1995), is het mogelijk dat twee visuele stimuli zich tegelijkertijd in het visuele veld van het gemeten neuron bevinden. Experimenten in de visuele cortex laten zien dat de vuurfrequentie van een neuron ten gevolge van het gelijktijdig aanbieden van een voorkeur en een niet-voorkeur stimulus in zijn receptieve veld, een vuurfrequentie is die tussen de door de individuele stimuli veroorzaakte vuurfrequenties in ligt. Indien de aandacht door de aap gericht wordt op één van deze twee in het receptieve veld aanwezige stimuli, dan benadert de gemeten vuurfrequentie de vuurfrequentie, die gemeten zou worden, indien enkel en alleen deze stimulus aangeboden zou worden. Een vuurfrequentie model (Reynolds et al., 1999) kan deze vuurfrequentie resultaten alleen reproduceren indien de synaptische koppelingssterktes van de neuronen die de sti-mulus waarop de aandacht gericht is representeren naar het ontvangende neuron, vijf keer zo sterk worden. Dit is fysiologisch zeer onrealistisch. Fries et al. (2001b) hebben getoond dat ten gevolge van aandacht de coherentie toeneemt en wel voordat de vuurfrequentie toeneemt. De in **Hoofdstuk 3** beschreven resultaten laten zien dat de coherentie tussen input- en output-signaal kan toenemen indien de mate van synchroon vuren van de inputsignalen in het gamma-gebied (30-80 Hz) toeneemt. Kan een toename in synchroniteit tussen input activiteiten, die de stimulus met aandacht representeren, ook de vuurfrequenties, zoals hierboven beschreven, verklaren?

In **Hoofdstuk 3** wordt getoond dat een eenvoudig feed-forward model met constante synaptische conductantie waardes inderdaad de effecten t.g.v. aandacht en stimulusselectie kan reproduceren. Dit geschiedt door synchronisatie van activiteit in de gamma-frequentie band, waardoor de synchrone input effectiever tot actiepotentialen leidt in het neuron waarop de synchrone input binnenkomt. Daardoor neemt de effectieve synaptische koppelingssterkte toe voor de stimulus, waarop de aandacht gericht is. Het model is robuust voor veranderingen in parameter waardes.

In dit hoofdstuk wordt verder gekeken naar de mate, waarin de actiepotentialen van het ontvangende neuron een fase voorkeur hebben t.o.v. de gamma-modulatie in de activiteit van de twee populaties, die de input leveren. De communicatie-door middel van - coherentie (CTC) hypothese zegt dat de voorkeur voor het faseverschil tussen de ontvangende en zendende populatie in de loop der tijd kan veranderen, waardoor de effectiviteit van de communicatie kan veranderen voor een bepaald tijdsinterval. De presynaptische input spikes zijn afkomstig van verschillende neuronen. Naarmate deze presynaptische neuronen meer gelijktijdig vuren, verschij-nen de input spikes meer synchroon in de tijd. Het model dat in **Hoofdstuk 3** beschreven is, voorspelt dat als de input spikes meer synchroon aankomen, de fase-locking tussen de presynaptische input en de response spikes toeneemt. Dit impliceert dat er een bepaalde fase is van het input signaal waarbij dezelfde input tot een grotere output leidt dan voor de overige fases. Dit betekent dat synchronisatie van neuronale activiteit een goede candidaat is om de effectieve synaptisch sterkte te veranderen en daarmee de effectiviteit van de communicatie te veranderen .

Indien de activiteit van een populatie neuronen zeer sterk gesynchroniseerd is, kan deze populatie benaderd worden door een fase oscillator zoals bijvoorbeeld een Mirollo-Strogatz (MS) oscillator. De fase relatie tussen twee gekoppelde MS-oscillators kan onderzocht worden als functie van de exciterende of inhiberende koppelingssterkte en ook als functie van de tijdsvertraging van een puls (actiepotentiaal), die optreedt tussen het zenden en de ontvangst door de andere oscillator. In **Hoofdstuk 4** worden analytisch de stabiele toestanden van twee puls-gekoppelde MS-oscillators, met en zonder de hierboven beschreven tijdsvertraging, bestudeerd. In het geval dat er geen tijdsvertraging optreedt en de twee exciterende oscillators even sterk aan elkaar gekoppeld zijn (symmetrische koppelingssterktes), vuren de twee oscillatoren gelijktijdig (Mirollo and Strogatz, 1990). Realistischer is om aan te nemen dat er een tijdsvertraging optreedt en in dat geval vuren de oscillatoren uitfase (Ernst et al., 1995, 1998). Symmetrische koppelingssterktes zijn echter eerder een uitzondering dan de regel in het brein.Ten gevolge van leren en plasticiteit ver-anderen de koppelingssterktes voortdurend. In **Hoofdstuk 4** wordt het effect van asymmetrische koppelingssterktes tussen twee MS-oscillators onderzocht, waarbij ook een tijdsvertraging tussen het versturen en het ontvangen van een puls aangenomen wordt. Voor grote tijdsvertragingen treedt slechts één stabiele toestand op, namelijk dat de twee fase oscillatoren precies in anti-fase (d.w.z. precies halverwege de periode van de ander) vuren. Voor de situatie, waarin de twee exciterende koppelingssterktes zich sterk onderscheiden en er sprake is van slechts een kleine tijdsvertraging, treedt slecht één stabiele toestand op: de oscillator (A), die de sterkste input (puls) ontvangt, vuurt direct na ontvangst van de puls afkomstig van de andere oscillator (B). Dit heeft tot gevolg dat de informatie (puls) betrouwbaar doorgegeven wordt in één richting (van B naar A), maar minder betrouwbaar in de andere richting, omdat er in de tijd tussen ontvangst van de puls en het uiteindelijk vuren, in principe nog van alles kan gebeuren. Indien het verschil in koppelingssterkte gering is, bestaan er twee stabiele toestanden, net als voor de situatie waarin de koppelingssterktes gelijk zijn (A drijft B, en vice versa).

Een verandering van synaptisch koppelingssterkte (bijv. t.g.v. het leren) verandert niets aan de relatieve fase tussen de twee oscillatoren in de stabiele toestand, tenzij de stabiele toestand samensmelt met de instabiele toestand (er treedt een zadelknoop bifurcatie op) en verdwijnt. Twee inhibitoir gekoppelde MS-oscillators vertonen stabiel infase vuurgedrag (Ernst et al., 1995, 1998), onafhankelijk van de tijdsvertraging tussen het zenden en ontvangen van dezelfde puls. Voor bepaalde situaties zijn twee stabiele toestanden mogelijk, waarbij de oscillators precies in fase of anti-fase vuren. Deze stabiele in fase en anti-fase toestanden veranderen in twee stabiele toestanden waarbij de neuronen uit-fase vuren, indien de twee koppelingssterktes niet meer precies gelijk (d.w.z. asymmetrisch) zijn. Verder reduceren de asymmetrische koppelingssterktes ook het domein, waarvoor twee stabiele toestanden bestaan. Kortom, asymmetrische koppelingssterktes reduceren het gebied van bistabiliteit. Een duidelijke asymmetrie in koppelingssterkte bevordert het betrouwbaar versturen en ontvangen van informatie in één bepaalde richting.

Welke rol de fase van de populatie activiteit speelt in de communicatie tussen twee neuronale populaties wordt in **Hoofdstuk 5** onderzocht. In deze studie wordt het corticospinale systeem beschouwd als een feedforward netwerk waarin de neuronen in de motor cortex projecteren naar de $\alpha$-motoneuronen in het ruggenmerg. Simulaties toonden dat de (veel zwakkere) projecties van het ruggenmerg naar de motor cortex verwaarloosd konden worden zoals verwacht op basis van de resultaten uit **Hoofdstuk 4**. Allereerst worden de resultaten van van Elswijk et al. (2009) gereproduceerd. Zij toonden aan, dat de effectiviteit van de communicatie tussen de neuronen in de motor cortex en in het ruggenmerg, gemoduleerd wordt door de fase van de ontvangende populatie, zoals voorspeld door de CTC-hypothese. In deze modelstudie hangt de MEP amplitude nauwelijks af van de fase van de beta drive van de neuronen in de motor cortex. In de studie van van Elswijk et al. (2009) wordt gerapporteerd dat de MEP-amplitude onafhankelijk is van de fase van het EEG signaal. Deze discrepantie kan verklaard worden door het feit dat de fase-afhankelijkheid te klein is om significant gemeten te kunnen worden in deze experimentele studie. De resultaten zoals beschreven in **Hoofdstuk 5** suggereren dat de MEP amplitude en de pre-TMS beta drive indirect gecorreleerd zijn door de coherentie tussen beta drive en EMG. De basis principes voor de resultaten van deze studie kunnen ook van toepassing zijn voor andere frequenties van ritmische neuronale oscillaties zoals alpha, mu en gamma ritmes.

# Dankwoord

Dit proefschrift sluit een interessante en leerzame periode af. Tijdens deze periode heb ik niet alleen de mogelijkheid gekregen om wetenschappelijk onderzoek te verrichten op een zeer boeiend terrein, maar ook om mezelf verder te ontwikkelen. Het onderzoek dat in dit proefschrift beschreven staat, zou niet tot stand gekomen zijn zonder de steun van diverse mensen. Door middel van dit dankwoord wil ik graag de gelegenheid gebruiken om een aantal mensen te bedanken.

Alleerst wil ik mijn promotor Stan Gielen bedanken. Dank je wel voor al je goede zorgen, je motiverende en optimistische houding, het delen van je grote parate kennis, je vertrouwen in mij, je enthousiasme en geduld en alle mogelijkheden die je me in de loop der jaren geboden hebt.

Pascal, dank je voor al je geduldige antwoorden op mijn vragen over jouw experimenten, data en data analyse technieken en je tips over welke recente artikels relevant waren voor ons onderzoek. Andreas, jij was altijd geïnteresseerd in mijn onderzoek vanaf het begin, dat deed mij erg goed. Dank je wel voor de interessante discussies, de prettige samenwerking en de gezelligheid. Sonja, danke für deine Ehrlichkeit und deinen guten Rat, wenn's mal nicht so gut lief. Ich bewundere Deine Leidenschaft. Dick, jou wil ik bedanken voor de kans die je me samen met Stan bood om aan dit promotie onderzoek te beginnen, voor je interesse en de prettige samenwerking. Julian, Eelke en Louis, dank jullie wel voor de goede samenwerking en de discussies tijdens onze ontdekkingsreizen gedurende jullie afstudeerstages.

Dankzij Helma kon ik direct op volle toeren beginnen met mijn promotie onderzoek. Met een gerust hart kon ik mijn kinderen aan haar toevertrouwen, vanaf de eerste dag. Als ik ze ophaalden, gingen ze niet direct mee naar huis, ze waren graag bij haar. Kinderen waren haar lust en leven. Helaas is ze veel te vroeg heengegaan.

Meow, meow, special thanks to Michelle, Zuzanna, Chloe, Birgit, Anna, Margarita and the other members of the Arcachon clan, for the science and for having a great time in Arcachon and every time we meet.

In de afgelopen jaren bestond er meer dan alleen maar wetenschap. Ik had

het geluk op een sociaal actieve en gezellige afdeling terecht te komen en wil dan ook alle voormalige en huidige collega's bedanken voor de fijne tijd op de afdeling. Enkele namen wil ik daarbij toch wel graag noemen. Martijn, als trouwe kamergenoot op alle vier de kamers die we in de loop van die vier jaar deelden, wil ik jou bedanken voor je humor, je luisterend oor, je hulp, de vele mokken thee en je gezelligheid. Willem, mijn tweede kamergenoot en de rust zelve, jou wil ik bedanken voor je positiviteit, steun en gezelligheid. Atthaphon, Martin, Moniek en Peter, mijn huidige kamergenoten, dank jullie wel voor de prettige en goede sfeer op onze kamer.

Naast een drukke baan heb ik ook een grote hobbie: sax spelen. Muziek maken zorgt voor de balans tussen het rationele en emotionele, tussen koppie en handen gebruiken. Speciale dank dan ook aan José, Lydia, Trix, Lex, Gnther, Josien, Gleb, Saxophonia, Theo en Luctor et Emergo, Vlijt en Volharding voor de vele uren ontspanning.

Verder wil ik mijn familie en vrienden bedanken voor de steun en interesse die zij getoond hebben in mijn onderzoek, mijn ouders voor hun vertrouwen in mij, voor de geweldige stimulans en praktische steun die zij mij in de loop der jaren gegeven hebben. Ich möchte meine Schwiegereltern herzlich bedanken für ihr Interesse und ihre Unterstützung.

Jacqueline, Geneviève en Géraud bedankt voor jullie interesse en steun tijdens de afgelopen jaren. Uli, mijn grote inspirator, steun en toeverlaat, dank je wel voor alle steun en liefde.

**Dank jullie wel!!!**

# Curriculum Vitae

Magteld Zeitler is geboren op 22 december 1970 te Nijmegen en groeide op op Alverna. Na het afronden van haar atheneum opleiding aan het Dukenburg College te Nijme-gen, begon ze in 1989 de studie Natuurkunde aan de Katholieke Universiteit Nijme-gen. In 1994 sloot ze haar studie af met het afstudeerwerk, dat ze verrichtte onder begeleiding van Prof. dr. ing. J.C. Maan op de afdeling Experimentele Vaste Stof Fysica I. Gedurende dit afstudeerwerk groeide haar wens om in de wetenschap verder te gaan. Alvorens die wens te vervullen, maakte ze een ’baby-pauze’ in het buitenland (Engeland en Duitsland) en besteedde haar spaarzaam overgebleven vrije uren vanaf oktober 1995 aan een (deeltijd-)studie wiskunde met bijvak informatica aan de FernUniversität Hagen, Duitsland. Inmiddels drie kinderen rijker, behaalde ze in 1999 het Vordiplom. In augustus 2002 kwam ze met haar gezin weer in Nederland wonen.

In september 2003 begon ze haar promotieonderzoek op de afdeling Medische Fysica en Biofysica aan de Katholieke Universiteit Nijmegen (huidige Radboud Universiteit Nijmegen) onder begeleiding van Prof. dr. C.C.A.M. Gielen. De wetenschappelijke resultaten van dit onderzoek staan in dit proefschrift beschreven. Een ander belangrijk resultaat is dat ze graag verder wil in het onderzoek. Als stimulans om in het onderzoek verder te gaan, heeft Magteld Zeitler in 2007 een Frye Stipendium gekregen, om naar het buitenland te gaan voor onderzoek en om haar werk daar meer bekendheid te geven. Dit heeft ze gedaan in Göttingen (D), Snowbird (USA) en Nottingham (GB). Momenteel werkt ze als post-doc op de afdeling Medische Fysica en Biofysica.


Was ..t ..s?
. ist das?
..s ist da.?

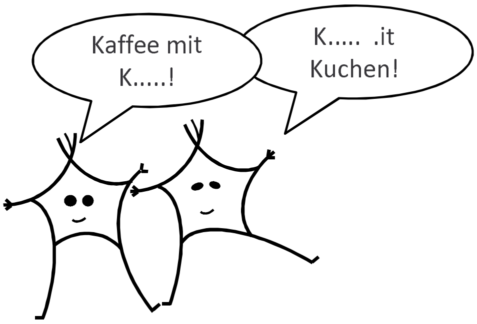
Kaffee mit K.....!
K..... .it Kuchen!